The Preserve: Lehigh Library Digital Collections

Thermal Characterization And Modeling Of Heterojunction Bipolar Transistors.

Citation

Whitefield, David Scott. *Thermal Characterization And Modeling Of Heterojunction Bipolar Transistors*. 1993, https://preserve.lehigh.edu/lehigh-scholarship/graduate-publications-theses-dissertations/theses-dissertations/thermal-10.

Find more at https://preserve.lehigh.edu/

This document is brought to you for free and open access by Lehigh Preserve. It has been accepted for inclusion by an authorized administrator of Lehigh Preserve. For more information, please contact preserve@lehigh.edu.

INFORMATION TO USERS

This manuscript has been reproduced from the microfilm master. UMI films the text directly from the original or copy submitted. Thus, some thesis and dissertation copies are in typewriter face, while others may be from any type of computer printer.

The quality of this reproduction is dependent upon the quality of the copy submitted. Broken or indistinct print, colored or poor quality illustrations and photographs, print bleedthrough, substandard margins, and improper alignment can adversely affect reproduction.

In the unlikely event that the author did not send UMI a complete manuscript and there are missing pages, these will be noted. Also, if unauthorized copyright material had to be removed, a note will indicate the deletion.

Oversize materials (e.g., maps, drawings, charts) are reproduced by sectioning the original, beginning at the upper left-hand corner and continuing from left to right in equal sections with small overlaps. Each original is also photographed in one exposure and is included in reduced form at the back of the book.

Photographs included in the original manuscript have been reproduced xerographically in this copy. Higher quality 6" x 9" black and white photographic prints are available for any photographs or illustrations appearing in this copy for an additional charge. Contact UMI directly to order.

U·M·I

University Microfilms International
A Bell & Howell Information Company
300 North Zeeb Road. Ann Arbor. MI 48106-1346 USA
313/761-4700 800/521-0600

Order Number 9325970

Thermal characterization and modeling of heterojunction bipolar transistors

Whitefield, David Scott, Ph.D.

Lehigh University, 1993

U·M·I
300 N. Zeeb Rd.
Ann Arbor, MI 48106

Thermal Characterization and Modeling of Heterojunction Bipolar Transistors

by

David S. Whitefield

A Dissertation

Presented to the Graduate Committee

of Lehigh University

in Candidacy for the Degree of

Doctor of Philosophy

in

Electrical Engineering

Lehigh University

May 1993

Approved and recommended for acceptance as a dissertation in partial fulfillment of the requirements for the degree of Doctor of Philosophy.

5/13/93
(date)

J C M Hwang
Professor in charge

Accepted 5/13/93
(date)

Special committee directing

The doctoral work of

David S. Whitefield

Dr. James C.M. Hwang
Chairman

Dr. D. Richard Decker

Dr. Frank H. Hielscher

Dr. Alastar K. Macpherson

Acknowledgements

I would like to thank Dr. James C.M. Hwang for his expert guidance and support over the course of this work, and for his clear explanations through which I have learned a great deal. I would also like to thank Dr. C.J. Wei for his assistance within the laboratory, particularly with microwave modeling.

I wish to thank the members of my committee, Professors James C.M. Hwang, D. Richard Decker, Frank H. Hielscher, and Alastar K. Macpherson for their timely advice and guidance.

I would like to thank the Air Force Office of Scientific research for providing the funding for this project under grant number 90-0302, and the Air Force Wright Laboratory for providing the transistors.

Also, I would like to thank my family for their understanding and support.

Table of Contents

Acknowledgements iii

Table of Contents iv

List of Tables vi

List of Figures vii

ABSTRACT 1

INTRODUCTION 3
- 1.1 HBT AND BJT TEMPERATURE EFFECTS 6
- 1.2 FOCUS OF THIS RESEARCH 7

BIPOLAR TRANSISTOR THERMAL EFFECTS 9
- 2.1 NOMENCLATURE AND VARIABLES 10
- 2.2 BASIS FOR BIPOLAR THERMAL EFFECTS 11
  - 2.2.1 Semiconductor Material Parameters 12
  - 2.2.2 Currents 17
  - 2.2.3 Gain 22
  - 2.2.4 Small Signal Elements 24
  - 2.2.5 Parasitic Resistances 26
- 2.3 SPECIFIC BJT AND HBT ANALYSIS 27
  - 2.3.1 BJT 27
  - 2.3.2 HBT 34
- 2.4 DISCUSSION 40

HBT THERMAL EFFECTS ON LOW FREQUENCY CHARACTERISTICS 41
- 3.1 EXPERIMENTAL 41
  - 3.1.1 dc Characterization 42
  - 3.1.2 Pulsed Characterization 44
  - 3.1.3 Junction Temperature Analysis 50
- 3.2 MODELING 56
  - 3.2.1 Large Signal Model 57
  - 3.2.2 Incorporation of Thermal Effects 59
  - 3.2.3 Model Implementation 60
- 3.3 RESULTS AND DISCUSSION 62

HBT THERMAL EFFECTS ON MICROWAVE PERFORMANCE 67
- 4.1 EXPERIMENTAL 68

4.2 THEORY AND ANALYSIS 72
4.2.1 Bias- and Temperature-Dependent Equivalent Circuit 73
4.2.2 One-Dimensional Physical Model 74
4.3 RESULTS AND DISCUSSION 77
4.3.1 I-V Characteristics 77
4.3.2 Small Signal Analysis 82
4.3.2.1 Microwave Circuit Elements 83
4.3.2.2 Error Analysis 87
4.3.2.3 Transit Times and Cutoff Frequencies 91

CONCLUSION 96
5.1 OVERVIEW 96
5.2 APPLICATIONS 100
5.3 FUTURE RESEARCH 100

REFERENCES 102

TEMPERATURE DEPENDENT HBT MODEL 112
A.1 User Defined Element Program Listing 112
A.2 Example Circuit file for HBT dc Simulation 119
A.3 Example Circuit file for HBT Pulsed Simulation 120
A.4 Example Circuit file for HBT Microwave Simulation 121

Vita 123

List of Tables

Table 2-1. Constants for bandgap expression of (2-1). 12
Table 2-2. Constants for the mobility expressions above. 15
Table 2-3. Relative importance of various currents for the HBT and BJT. 27

Table 3-1. Formulas used in large signal temperature-dependent modeling. 61

Table 4-1. Material thickness and doping structure. 68

List of Figures

Figure 2-1. Temperature dependence of bandgap energy for Si, GaAs, and AlGaAs. 13
Figure 2-2. Temperature dependence of intrinsic carrier concentration for Si, GaAs, and AlGaAs. 14
Figure 2-3. Temperature dependence of electron and hole mobilities for Si, GaAs, and AlGaAs. 16
Figure 2-4. Temperature dependence of saturation velocity for Si and GaAs. 18
Figure 2-5. Current flow diagram for a bipolar transistor. 19
Figure 2-6. Gummel plot for an HBT showing the base and collector ideality factors. 28
Figure 2-7. Energy band diagram of homojunction bipolar junction transistor. 28
Figure 2-8. Cross section of a typical double-diffused BJT. 29
Figure 2-9. Temperature dependence of current gain for a BJT where high emitter doping has caused a base-emitter change in bandgap. 30
Figure 2-10. Calculations of the temperature dependence of the BJT current components assuming a 0.02 eV change in base-emitter bandgap. 31
Figure 2-11. SPICE simulation of I_b for a BJT at different ambient temperatures. 32
Figure 2-12. Measurements of the temperature dependence of V_{be} for a BJT. 32
Figure 2-13. Calculations of the temperature dependence of V_{be} for the BJT currents. 33
Figure 2-14. Energy band diagram for an HBT. 35
Figure 2-15. Cross section of an AlGaAs/GaAs HBT. 35
Figure 2-16. Temperature dependence of the components of current gain for the HBT. 37
Figure 2-17. Collector characteristics for an HBT in the common emitter configuration. 37
Figure 2-18. Temperature dependence of the current components in an HBT. 38
Figure 2-19. Temperature dependence of V_{be} for the current components in an HBT. 39
Figure 3-1. Measurements of the base-emitter characteristics for the HBT at several ambient temperatures. 43
Figure 3-2. Temperature dependence of V_{be} for the HBT at constant base currents. 44
Figure 3-3. 110 ns pulsed measurement system used to measure the HBT collector characteristics. 45
Figure 3-4. Pulsed-source load line superimposed on the HBT base-emitter characteristics at several junction temperatures. 46
Figure 3-5. Oscilloscope traces of the pulse-generator voltage and the actual V_{be} of the HBT. The V_{be} decrease is caused by the influence of

the source load-line during heating. 47
Figure 3-6. Collector current response to a base voltage pulse. The decrease in I_c is caused by self-heating. 47
Figure 3-7. Pulsed and dc characteristics of an HBT. The reduction of self-heating causes the pulsed characteristics to show much less negative differential resistance. 48
Figure 3-8. HBT pulsed response at low dissipated power (minimal self-heating). 49
Figure 3-9. HBT pulsed characteristics at high dissipated power (large self-heating). 50
Figure 3-10. Sequential measurements showing a permanent decrease in device gain. 51
Figure 3-11. V_{be} characteristics of an HBT at constant I_b. V_{be} decreases due to self-heating at high power levels. 52
Figure 3-12. Collector current corresponding to the V_{be} measurements of Figure 3-11. 53
Figure 3-13. Determination of thermal resistance by using calibrated V_{be} characteristics 54
Figure 3-14. Junction temperature contours superimposed on collector characteristics. 54
Figure 3-15. Current gain degradation with temperature for the HBT. 55
Figure 3-16. Comparison of pulsed measurements and those predicted from dc thermal calculations. 56
Figure 3-17. Large signal model used for modeling HBT transport and thermal effects. 57
Figure 3-18. Large signal current gain element fit to data extracted from bias-dependent S-parameter measurements. 58
Figure 3-19. Thermal circuit used within the large signal model to emulate the transient change in junction temperature. 59
Figure 3-20. Sequence of operations performed during large signal simulations. 62
Figure 3-21. Modeled HBT pulsed characteristics. 63
Figure 3-22. Measured HBT pulsed characteristics. 64
Figure 3-23. Junction temperature waveform during the pulsed simulation. 64
Figure 3-24. Comparison of large signal model simulation with dc characteristics. 65
Figure 3-25. Comparison of large signal model simulation with pulsed characteristics. 66
Figure 4-1. Variable temperature S-parameter measurement system. 69
Figure 4-2. Heat shields installed to protect probe-body overheating. 70
Figure 4-3. Linear V_{be} characteristics used for calibration of wafer ambient temperature. 71
Figure 4-4. Bias points used for elevated temperature S-parameter measurements. 72

Figure 4-5. Microwave equivalent circuit used for bias- and temperature-dependent parameter extraction. 73
Figure 4-6. Measured and modeled Base and Collector currents for the HBT at two temperatures. 78
Figure 4-7. Physical Modeling of room temperature collector characteristics. 79
Figure 4-8. Physical modeling of V_{be} associated with characteristics of Figure 4-7. 79
Figure 4-9. Physical modeling of collector characteristics at 226°C. 80
Figure 4-10. Physical modeling of V_{be} associated with characteristics of Figure 4-9. 80
Figure 4-11. Junction temperatures calculated by the physical model for the previous room temperature and 226°C simulations. 82
Figure 4-12. Gummel plot including physical model calculations and measurements at all evaluated temperatures. 83
Figure 4-13. Model calculations and measurements of the base-emitter resistance, R_{eb}. 84
Figure 4-14. Model calculations and measurements of transconductance, g_m. 85
Figure 4-15. Model calculation of base-emitter capacitance showing depletion and diffusion components. 86
Figure 4-16. Model calculations and measurements of the base-emitter capacitance, C_{eb}. 86
Figure 4-17. Measured parasitic base and emitter resistances versus base-emitter voltage. For the physics-based model calculations these resistances are assumed to be constant. 88
Figure 4-18. Error analysis for R_{eb}, accounting for a ±20% error in material parameters and a ±70% change in parasitic resistances. 89
Figure 4-19. Error analysis for g_m under the same conditions as for Figure 4-18. 90
Figure 4-20. Error analysis for C_{eb} under the same conditions as for Figure 4-18. 90
Figure 4-21. Measurements of |H21| and maximum available gain/maximum stable gain, showing the f_{MAX} and f_T figures of merit. 92
Figure 4-22. Model calculations and measurements of unity gain cutoff frequency, f_T. 93
Figure 4-23. Model calculations and measurements of maximum frequency of oscillation, f_{MAX}. 93
Figure 4-24. Measured and modeled f_T as a function of temperature. 94
Figure 4-25. Measured and modeled f_{MAX} as a function of temperature.. 94

ABSTRACT

The heterojunction bipolar transistor (HBT) is a very promising device for high power microwave applications. Recently, HBTs have demonstrated impressive characteristics, with typical values for maximum frequency of oscillation, f_{MAX}, of over 100 GHz and power densities of 5 W/mm of emitter length. At such high power densities internal junction temperatures can rise to over 200°C causing its I-V characteristics to change significantly. These temperature-dependencies are in some ways similar to those of the well known homojunction bipolar transistors, but in other ways are completely opposite.

In this work a theoretical investigation of the thermal effects for the general class of bipolar transistors is performed. This analysis, based on the temperature dependencies of the major semiconductor properties, applies to homojunction transistors as well as the HBT. From this analysis, and from dc characterization of actual HBTs, the main thermal effects were found to be a linear decrease in gain with increasing temperature and a linear decrease in base-emitter voltage at constant base current. Both of these effects were included into a large signal model based on pulsed and dc characterization. This model was implemented in a commercial microwave circuit simulator and can be used for dc, pulsed and microwave simulations.

Microwave measurements were also performed at elevated ambient temperatures to characterize the change in small signal parameters with temperature. The base-emitter resistance and capacitance, and the transconductance were found to be the most

temperature-sensitive. Theoretical calculations were performed from material properties and geometry and gave an accurate indication of the relative changes in the small-signal elements with temperature and bias. Over this 200°C temperature range the maximum frequency of oscillation was found to monotonically decrease by a total of 60%.

The characterization results and models developed for this work are valuable tools for improving HBT device and circuit design specifically for high power applications. Using these tools, final packaged device performance can be determined using only on-wafer measurements. The effect of different heat sink thermal resistances on device performance can be evaluated and power-dissipation limits can be determined in all modes of operation including dc, pulsed, and continuous wave.

Chapter 1
INTRODUCTION

The concept of the heterojunction bipolar transistor (HBT) is as old as the transistor itself. Designing a circuit element (transistor) with two adjoining semiconductor layers of different bandgaps was one of the claims in William Shockley's original patent on the transistor in 1948 [1]. Since the inception of the transistor, the *homojunction* bipolar transistor, or bipolar junction transistor (BJT), has matured quickly into a mainstream technology particularly for analog applications.

The HBT did not undergo this same rapid development because of the physical impossibility at the time, of achieving an abrupt low-defect junction between two different semiconductors. The idea of an HBT lay dormant for twenty years until semiconductor growth technology advanced to the point to allow its implementation. In the mid-1970's molecular beam epitaxy (MBE) and metal-organic chemical vapor deposition (MOCVD) were developed which allowed precise control of semiconductor composition and doping during the growth of thin films. Today, single atomic layer accuracy can be achieved at a growth rate of approximately one mono-layer per second.

Ever since the implementation of the HBT, it has developed relatively slowly because of the earlier development and steady improvement of the competing single semiconductor type devices. These devices include the Si based BJT and, for microwave applications, the GaAs metal semiconductor field effect transistor (MESFET). The HBT does, however, have performance advantages over these other devices specifically for

microwave and millimeter wave high power applications.

The basic structure of the HBT is similar to that of the BJT with three regions of semiconductors, n-p-n or p-n-p corresponding to the emitter-base-collector regions. The HBT differs from the BJT in that the emitter is made from a semiconductor with a wider bandgap than that of the base and collector. The gain of a bipolar transistor is fundamentally dependent on the base-emitter junction composition and doping, and as a result, this change in bandgap for the HBT increases its maximum attainable gain by approximately five orders of magnitude. Since a current gain of 1×10^7 is not necessary, or even desirable, in most applications, other aspects of the device design can be optimized at the expense of gain. The real advantage of the HBT is this flexibility the bandgap engineering allows now that designing for adequate gain is not a primary concern. This flexibility is generally used in the HBT to design for high frequency operation.

One typical technique to increase frequency response is to dope the base region much greater than that of the emitter. This allows the base region to be designed very thin without sacrificing base sheet resistance. This in turn reduces the base transit time, and increases the frequency response. In addition, the base-collector depletion capacitance can be quite low because of the low doping in the collector, also enhancing the frequency response. With the use of the precise epitaxial technologies, which are also used for other types of devices, the collector region can be designed for low collector-base capacitance and a desired breakdown voltage at the expense of collector transit time and current carrying capacity.

Recently, HBTs have demonstrated impressive characteristics, with typical values for maximum frequency of oscillation, f_{MAX}, of over 100 GHz, power densities of 5 W/mm of emitter length, and power added efficiencies of 50% [2-6]. HBTs are also living up to their potential in high frequency, high power circuits with power amplifiers operating typically in the range 6-12 GHz with gains of 10 dB and output powers of 1-4 W [7-13].

The application of HBTs in the future looks bright, as the operating frequencies and power densities for ICs continue to increase. In order to achieve high frequency operation, dimensions for transistors must be reduced, particularly in the direction of current flow. FETs are horizontal devices where this critical length is defined by lithography which is becoming increasingly more challenging as dimensions push 0.1 μm. The HBT, however, is a vertical device with critical dimensions defined by the epitaxial growth which has atomic layer accuracy. For good device performance, the lithographic constraints on HBTs are quite relaxed at greater than 1 μm.

The future trends for HBT applications also point to high power applications. The HBT has already exhibited the ability to handle extremely high current and power densities of 1×10^5 A/cm^2, and 1×10^5 W/cm^2. Today, HBT circuit performance is restrained by thermal limitations rather than electrical, and in the pulsed condition, HBTs have exhibited power densities of 6×10^5 W/cm^2 [14]. Due to the thermal limitations, there is a great need for thermal characterization and modeling in order to develop circuit topologies which minimize self-heating, and effectively treat the unique thermal characteristics of the device in both continuous wave (CW) and pulsed operation.

1.1 HBT AND BJT TEMPERATURE EFFECTS

Because bipolar devices can handle large current and power densities, high junction temperatures are inevitable in many applications. Therefore, there has been considerable interest in characterizing the effect of temperature on both BJTs and HBTs. In some ways the thermal effects between these two types of transistors is similar, but in other ways the resulting effects are quite different, and in fact are the opposite. The reason the effects are different is due to the differing physical structure as well as the differing characteristics of the materials most commonly used for each type of device.

Even though the materials and structure of the HBT and BJT are different, they are both based on p-n junction diodes which have similar temperature dependencies. Their characteristics differ only in the degree of dependence. As a consequence, their base-emitter temperature characteristics are similar, and show an exponentially increasing current with temperature.

The differing base-emitter structures do, however, cause an intrinsic difference in the behavior of current gain with temperature. Due to the change in bandgap for the HBT, the ratio of various current components turns out to be quite different than in the BJT. As a result, the two devices have opposite current gain dependencies on temperature. For the BJT, gain increases with temperature, and for the HBT it decreases. A detailed analysis in Chapter 1 reveals the basis of such differences.

Due to this basic difference in behavior, traditional temperature-dependent BJT models have failed to predict the HBT thermal performance. Therefore characterization and modeling of thermal effects is required which is specific to the HBT.

1.2 FOCUS OF THIS RESEARCH

Due to its delayed development, currently the state of HBT characterization and modeling lags that of other devices, but is beginning to quickly become mature. Accurate modeling and knowledge of the HBT is still needed especially regarding the high power, and therefore high temperature, operating conditions. This work investigates the effect of increasing junction temperature on the electrical characteristics of the HBT. Characterization techniques are developed and used to analyze the HBT under elevated ambient temperatures and self-heating conditions. Physical modeling is performed from first principles to correlate measured effects with semiconductor physics. In addition, large signal and small signal temperature-dependent equivalent circuit modeling is performed to provide a tool for use in high power circuit design.

In this work, Chapter 2 is an investigation of the thermal effects for the general class of bipolar transistors. It is based on standard semiconductor physics, and includes the effects of a base-emitter change in bandgap. Expressions for the various currents and gain components are presented as well as for the small signal equivalent circuit element values and parasitic resistances. The temperature dependencies are evaluated for all expressions based on the measured and theoretical behavior of fundamental semiconductor properties. Specific analyses are presented for the Si based BJT and the GaAs/AlGaAs HBT.

Chapter 3 contains a discussion of the low frequency thermal effects for the HBT. Characterization techniques an measurement results are presented for dc and pulsed

analysis of thermal effects. A large signal temperature-dependent model topology and implementation is presented for the HBT and shown to be valuable for simulating the high-power characteristics and pulsed responses. Chapter 4 is a presentation of elevated temperature measurement and modeling results at microwave frequencies. An equivalent circuit is used to extract small signal elements from bias- and temperature-dependent S-parameter measurements taken up to 226°C. A comparison is performed of these elements against theoretical calculations based on the theoretical development in Chapter 2. In addition, an error analysis of these calculations is performed. Finally an analysis of the overall device figures of merit are analyzed versus temperature.

Chapter 5 is a conclusion including applications of this work for circuit design and device optimization. Areas for future research are discussed which also use tools and techniques developed in this work.

Chapter 2
BIPOLAR TRANSISTOR THERMAL EFFECTS

Temperature is a very important variable for the analysis of transistors. It can change device characteristics dramatically, and can even cause positive feedback situations which burn out the transistor. In a discussion of the temperature effects on a device it is important to bear in mind that the temperature of the device is only partially determined by the ambient temperature. Equally as important is the self-heating effects which can raise the actual device temperature up to several hundred degrees. Self-heating is basically proportional to the dissipated power. Also, in general, the temperature is not constant throughout the entire device, and local "hot spots" can become important.

This analysis of the bipolar transistor thermal effects will concentrate on the temperature range from room temperature up to approximately 200°C. Since the goal of this work is to model the self-heating effects of the HBT, this is the most important temperature range. Some of the analysis, however is also valid for temperatures significantly less than room temperature. In addition, the effects considered are analyzed for forward active region of operation, but can be extended to other regions as well.

This analysis concentrates on the intrinsic device region consisting of the entire base width and the immediate adjoining emitter and collector regions. This intrinsic device is assumed to be entirely at the same temperature which is a reasonable assumption for normal operation. Some effects where this does not hold are noted.

2.1 NOMENCLATURE AND VARIABLES

The variables, subscripts and constants which are used throughout this analysis are listed below along with their interpretation.

Variable:	Interpretation:
A_e	emitter area
A_s	emitter-base exposed surface area
C_{eb}	small-signal base to emitter capacitance
C_j	depletion region capacitance
C_{je}	base-emitter depletion region capacitance
E_g	bandgap energy
f_T	unity current gain cutoff frequency
f_{MAX}	maximum frequency of oscillation
gm	transconductance
H21	H-parameter transmission component (I_2/I_1)
I	current
J	current density
L	electron or hole diffusion length
n	electron concentration
N	doping concentration
N_c	conduction band density of states
n_i	intrinsic carrier concentration
n_{i0}	temperature independent constant in n_i
N_v	valence band density of states
p	hole concentration
P_{dc}	dc power dissipation
R	resistance
R_{th}	thermal resistance
R_{eb}	small-signal base to emitter resistance
S	surface recombination velocity
T	temperature in Kelvin
t	time
V_{bc}	base-collector applied voltage
V_{be}	base-emitter applied voltage
V_{bi}	junction built in voltage
V_T	thermal voltage = kT/q
v_{sat}	saturation velocity
W	quasi-neutral width of semiconductor
X_d	depletion-region width
α	base transport factor
β_f	forward current gain

βr	reverse current gain
β_{sr}	current gain limit due to surface and depletion region recombination
β_{α}	current gain limit due to the base transport factor
β_{γ}	current gain limit due to the emitter efficiency
γ	emitter efficiency
Δ	change in ...
ϵ	material dielectric constant
ρ	resistivity
σ	conductivity
τ	electron or hole lifetime
τ_{ec}	emitter to collector transit time
τ_b	base transit time
τ_d	depletion recombination lifetime
τ_s	surface recombination lifetime
μ	mobility

Subscripts:	Referring to a property of:
b	the base
c	the collector
e	the emitter
n	an electron
p	a hole
0	a constant

Physical Constants:		Value:
k	Boltzmann constant	$= 1.38\text{x}10^{-23}$ J/K
q	electron charge	$= 1.6\text{x}10^{-19}$ C

2.2 BASIS FOR BIPOLAR THERMAL EFFECTS

Just about every property of semiconductors is dependent on temperature which can make analysis of temperature effects very complicated. The following concentrates on the properties with the most severe temperature dependence or the properties which have significant impact on the bipolar transistor characteristics. These properties include the bandgap, E_g, the intrinsic carrier concentration, n_i, the electron and hole mobility, μ_n and μ_p, and the electron saturation velocity, v_{sat}.

The materials which are analyzed include Si, which is currently the exclusive material used for homojunction bipolar transistors (BJTs). Also, GaAs and AlGaAs are analyzed which are the most common materials used for heterojunction bipolar transistors (HBTs). For AlGaAs, the common Al mole fraction of 25% is assumed, therefore the compound is written $Al_{0.25}Ga_{0.75}As$.

2.2.1 Semiconductor Material Parameters

One of the most basic material properties of a semiconductor is its bandgap, E_g, which has an effect on a large number of other properties of the material. E_g tends to decrease with increasing temperature [15] following the empirical equation

$$E_g = E_{g0} - \frac{K_1 T^2}{(T + K_2)} \tag{2-1}$$

where E_{g0}, K_1, and K_2 are constants given in Table 2-1 for Si, GaAs and AlGaAs [16]. For AlGaAs, the temperature dependence is assumed to be the same as for GaAs because of the similarities between AlAs and GaAs, and because of the low mole-fraction of Al considered. Figure 2-1 shows the three bandgap energies.

Material	Constants		
	E_{g0}	K_1	K_2
Si	1.170	4.73×10^{-4}	636
GaAs	1.519	5.41×10^{-4}	204
$Al_{0.25}Ga_{0.75}As$	1.829	5.41×10^{-4}	204

Table 2-1. Constants for bandgap expression of (2-1).

Another material property, the intrinsic carrier concentration n_i, is a very strong function of temperature. In addition, the *square* of n_i is found in many of the transport and recombination currents

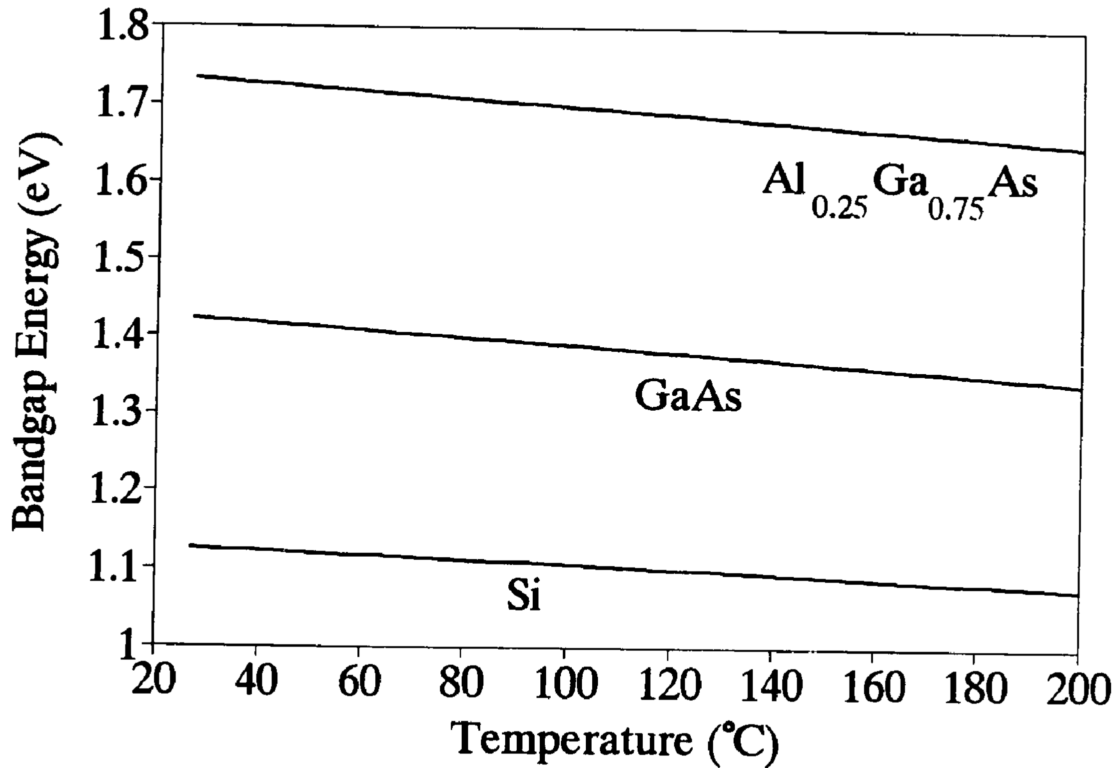

Figure 2-1. Temperature dependence of bandgap energy for Si, GaAs, and AlGaAs.

for the bipolar transistor making it an even more important factor in evaluating transistor thermal effects. n_i can be derived from Fermi-Dirac statistics [15] as

$$n_i = \sqrt{N_c N_v}\; e^{\left(-\frac{E_g}{2V_T}\right)} \tag{2-2}$$

where the density of states N_c and N_v have a T^3 dependence. Therefore,

$$n_i = n_{i0}\, T^{\left(\frac{3}{2}\right)}\, e^{\left(-\frac{E_g}{2V_T}\right)} \qquad (2\text{-}3)$$

where n_{i0} is a temperature independent constant. Experimentally n_i has been found to agree very well to these theoretical temperature dependencies [17]. In the overall temperature dependence, the effect of the exponential term dominates over the $T^{3/2}$ term. Figure 2-2 shows the temperature dependence of n_i which includes the change in E_g with temperature.

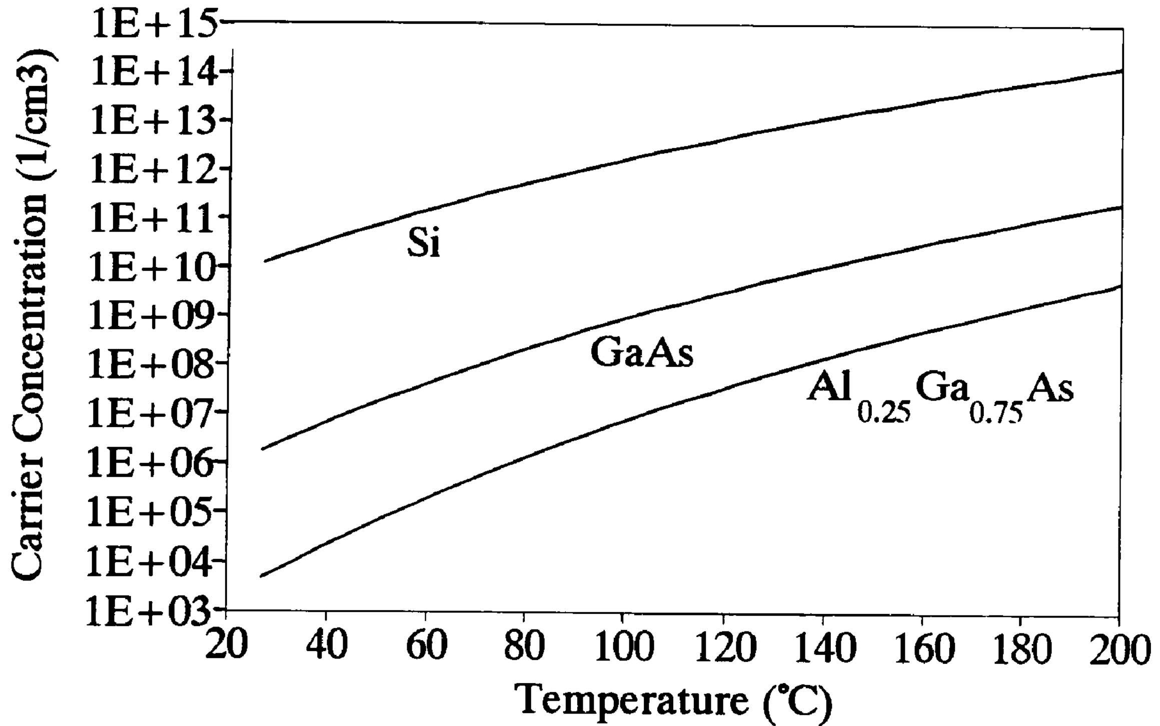

Figure 2-2. Temperature dependence of intrinsic carrier concentration for Si, GaAs, and AlGaAs.

The constants n_{i0} for the different materials are indicated below where again, for lack of

measured data, the $Al_{0.25}Ga_{0.75}As$ behavior [16] is assumed to be similar to that of GaAs.

$$n_{i0\text{-}Si} = 6.70\times10^{15}\ cm^{-3}$$

$$n_{i0\text{-}GaAs} = 2.92\times10^{14}\ cm^{-3}$$

$$n_{i0\text{-}AlGaAs} = 2.92\times10^{14}\ cm^{-3}$$

Mobility is also a function of temperature. Its empirically determined behavior versus temperature and total doping concentration N (donors and acceptors) takes on the following form for Si, valid from room temperature to greater than 250°C [15,18,19].

$$\mu_{Si} = \left[\frac{K_1}{1+(K_2N)^{K_3}}\right]\left[\frac{300}{T}\right]^{K_4} + K_5 \qquad \left(\frac{cm^2}{Vs}\right) \tag{2-4}$$

For GaAs, mobility has been fit to a slightly different equation [16,20,21]:

$$\mu_{GaAs} = \left[\frac{K_1}{(1+K_2N)^{K_3}}\right]\left[\frac{300}{T}\right]^{K_4} \qquad \left(\frac{cm^2}{Vs}\right) \tag{2-5}$$

where K_1 - K_5 are the constants given in Table 2-2 for electron and hole mobility of the

Material	Mobility type	Constants				
		K1	K2	K3	K4	K5
Si	μ_n	1265	1.18×10^{-17}	0.72	1.5	65
	μ_p	447	5.26×10^{-18}	0.76	1.5	48
GaAs	μ_n	8000	5.51×10^{-17}	0.23	2.3	
	μ_p	380	3.17×10^{-17}	0.26	2.7	
$Al_{0.25}Ga_{0.75}As$	μ_n	6046	5.51×10^{-17}	0.23	2.3	
	μ_p	303	3.17×10^{-17}	0.26	2.7	

Table 2-2. Constants for the mobility expressions above.

particular materials. Figure 2-3 shows the temperature dependence of electron and hole mobilities for the various materials. The room temperature mobilities of AlGaAs are well known [16,22], but there is a lack of experimental fitting results for the temperature

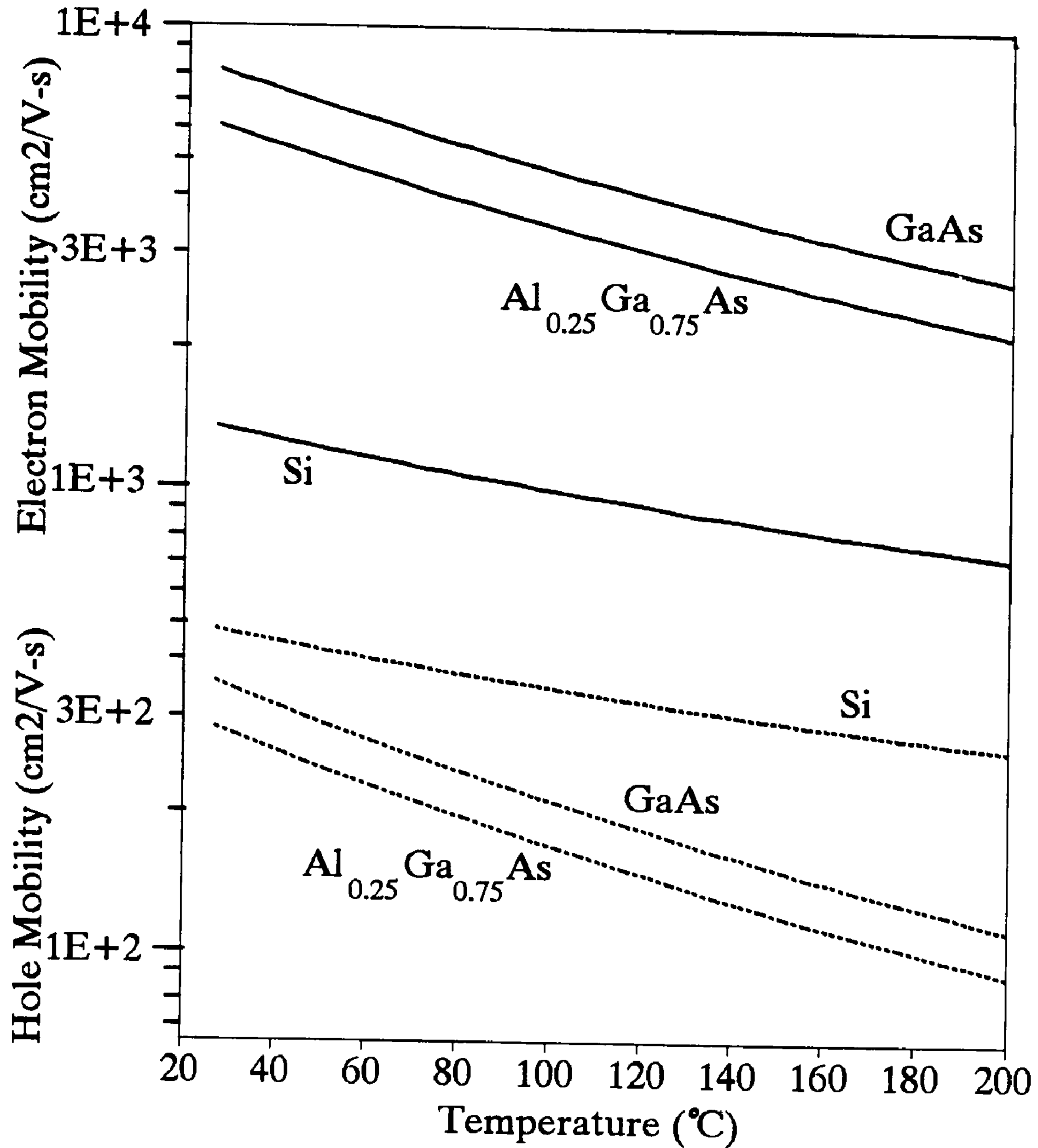

Figure 2-3. Temperature dependence of electron and hole mobilities for Si, GaAs, and AlGaAs.

dependence these mobilities. Therefore, the temperature dependence of the AlGaAs mobilities has been assumed to be the same as for GaAs.

At high electric fields, the velocity of electrons tends to saturate in semiconductors and only small changes in velocity are noticed for a given change in field. This saturation is equivalent to a terminal velocity, and is caused by lattice scattering. Lattice scattering increases with temperature and will cause v_{sat} to decrease. For GaAs the saturation velocity has been empirically determined [20,21] to be

$$v_{sat-GaAs} = (1.28 - 0.0015\ T)x10^{7} \quad \left(\frac{cm}{\sec}\right) \tag{2-6}$$

at 50 KV/cm. Likewise for Si, the saturation velocity is [15]

$$v_{sat-Si} = \frac{2.4x10^{7}}{1 + 0.8e^{\left(\frac{T}{600}\right)}} \quad \left(\frac{cm}{\sec}\right) \tag{2-7}$$

Figure 2-4 illustrates these dependencies.

2.2.2 Currents

The analysis of the transport equations for the bipolar transistor has been evaluated in the following sections to include detailed terms accounting for the unique features of both BJTs and HBTs. The expressions have been developed based on Maxwell-Boltzmann statistics and have been formulated to agree with both specific BJT [23-27] and HBT [28-39] analyses.

In order to analyze the terminal currents of the bipolar transistor, it is useful to separate them into distinct components which then add together to produce the actual

characteristics. These components include several injection and recombination currents which are shown in the simplified current flow diagram of Figure 2-5.

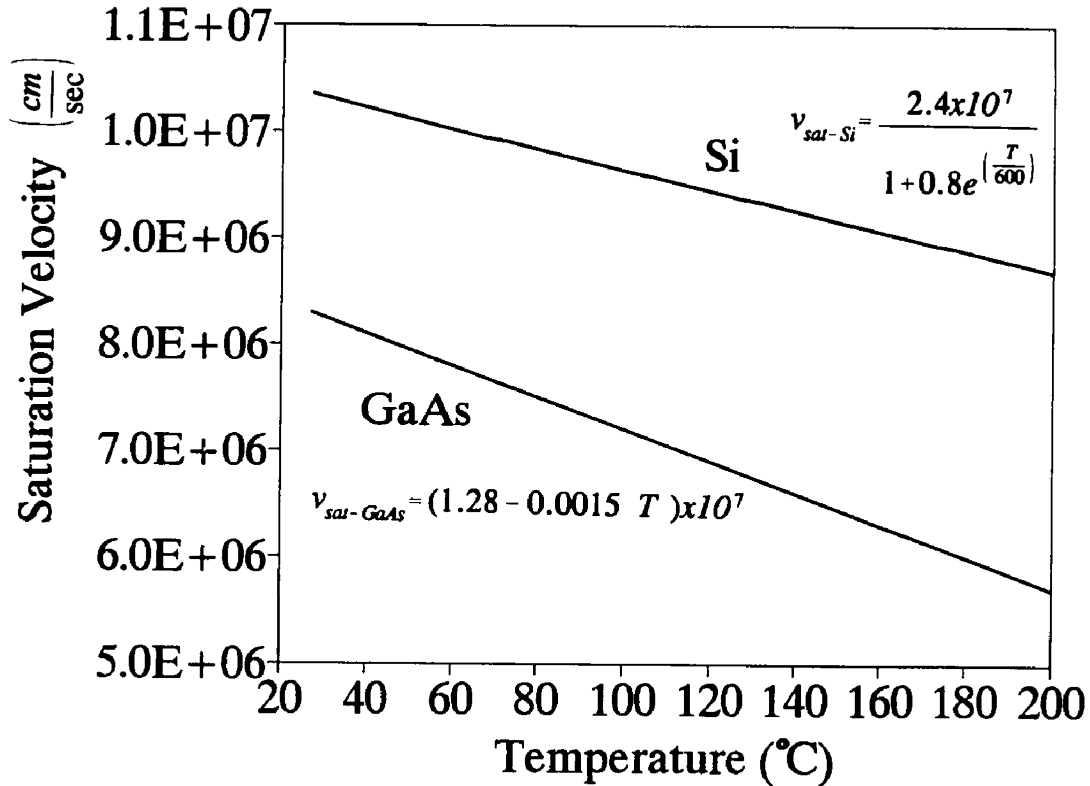

Figure 2-4. Temperature dependence of saturation velocity for Si and GaAs.

In formulating the current equations for the bipolar transistor it is useful to make several assumptions which can greatly simplify the analysis. First, for the forward active region of operation the base-collector junction is assumed to be reverse biased therefore $e^{(Vbc/VT)} \approx 0$ and the parasitic base-collector currents (which are not figured) can be neglected. With the additional standard assumptions that $e^{(Vbe/VT)} \gg 1$, $W_e \ll L_{pe}$, and $W_b \ll L_{nb}$, the equations for the currents shown in Figure 2-5 are listed in the following,

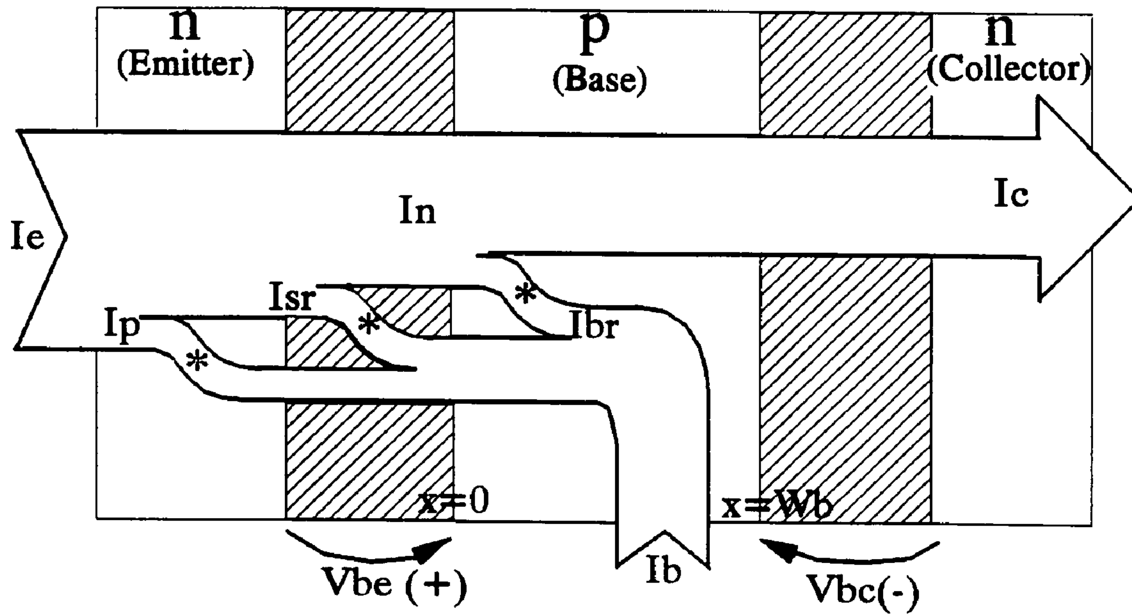

Figure 2-5. Current flow diagram for a bipolar transistor.

for an n-p-n transistor.

The main current of the device is the electron current injected from the emitter into the base,

$$I_n = A_e \left[\frac{qV_T\ \mu_{nb}\ n_{ib}^2}{N_b W_b} \right] e^{\left(\frac{V_{be}}{V_T}\right)} \tag{2-8}$$

and the hole current which is injected from the base to the emitter is

$$I_p = A_e \left[\frac{qV_T\ \mu_{pe}\ n_{ie}^2}{N_e W_e} \right] e^{\left(\frac{V_{be}}{V_T}\right)} \tag{2-9}$$

The quasi-neutral base recombination current is

$$I_{br} = A_e \left[\frac{qW_b\ n_{ib}^2}{2N_b \tau_{nb}} \right] e^{\left(\frac{V_{be}}{V_T}\right)} \tag{2-10}$$

and the surface and depletion recombination current is

$$I_{sr}=\left[\frac{q\ n_{ie}}{2}\right]\left[\frac{A_e X_d}{\tau_d}+A_s S\right]e^{\left(\frac{V_{be}}{2V_T}\right)} \tag{2-11}$$

The depletion region and surface recombination have been combined together into (2-11) because they both have the same $e^{(V_{be}/2V_T)}$ term. This results because they are both Shockley-Read-Hall recombination processes [20,40,41]. In I_{sr}, the $(A_e X_d/\tau_d)$ term is for depletion region recombination while $(A_s S)$ is for surface recombination. The depletion region recombination for both the BJT and HBT is insignificant in the normal forward active region, only becoming important for the BJT at low values of V_{be}. Surface recombination is also insignificant for the BJT, but is very important for the HBT where it dominates over the depletion region recombination. For these reasons I_{sr} for future calculations will only include the surface effect as in

$$I_{sr}=\left[\frac{qn_{ie}\ A_s S}{2}\right]e^{\left(\frac{V_{be}}{2V_T}\right)} \tag{2-12}$$

Using these current equations, the terminal currents of the device can be formulated referring again to Figure 2-5:

$$I_e=I_n+I_p+I_{sr} \tag{2-13}$$

$$I_b=I_p+I_{sr}+I_{br} \tag{2-14}$$

$$I_c=I_n-I_{br} \tag{2-15}$$

By analyzing the dependence of each term in the current equations the overall temperature behavior can be obtained. In the following, equations are presented showing the temperature proportionality for each current using the combined temperature dependence of V_T, mobility, n_i^2, and $e^{(Vbe/VT)}$.

$$I_n \propto T^{(4-K_4)}\, e^{\left(\frac{V_{be}-E_{gb}}{V_T}\right)} \tag{2-16}$$

$$I_p \propto T^{(4-K_4)}\, e^{\left(\frac{V_{be}-E_{ge}}{V_T}\right)} \tag{2-17}$$

$$I_{br} \propto T^{3}\, e^{\left(\frac{V_{be}-E_{gb}}{V_T}\right)} \tag{2-18}$$

$$I_{sr} \propto T^{1.5}\, e^{\left(\frac{V_{be}-E_{ge}}{2V_T}\right)} \tag{2-19}$$

K_4 is the exponent for the mobility as a function of T found in (2-4) and (2-5) and in Table 2-1. Each current can be seen to depend on a particular power of T as well as an exponential of V_{be}-E_g. When gain equations are derived, which are simply ratios of different currents, their temperature variation can be easily evaluated by noting the ratios of the respective equations (2-16) - (2-19).

When evaluating these proportionalities using actual values for the particular

semiconductors, it is found that the exponential term dominates over the power of T term. Therefore with constant V_{be}, each current increases exponentially with T.

These equations can be inverted to show V_{be} in terms of current:

$$V_{be}(I_n) \propto E_{gb} + V_T\left[\ln(I_n) - \ln(T^{(4-K_4)})\right] \tag{2-20}$$

$$V_{be}(I_p) \propto E_{ge} + V_T\left[\ln(I_p) - \ln(T^{(4-K_4)})\right] \tag{2-21}$$

$$V_{be}(I_{br}) \propto E_{gb} + V_T\left[\ln(I_{br}) - \ln(T^{3})\right] \tag{2-22}$$

$$V_{be}(I_{sr}) \propto E_{ge} + 2V_T\left[\ln(I_{sr}) - \ln(T^{1.5})\right] \tag{2-23}$$

In this case the V_T term dominates over $\ln(T^x)$ and V_{be} decreases *linearly* with T. This effect has been used to create very accurate temperature sensors based on the forward diode voltage at constant current.

2.2.3 Gain

To obtain the total gain for the bipolar transistor it is instructive to evaluate it in parts, and then combine the parts [23-25,40]. The various gain portions help intuitively understand the role and relative importance of each current. One parameter to help evaluate the parts of current gain is the emitter efficiency, γ, describing the efficiency by which electrons are injected into the base compared to the undesirable injection of

holes into the emitter. Emitter efficiency is defined as

$$\gamma = \frac{I_n}{I_n + I_p} \tag{2-24}$$

A current gain equation reflecting only this emitter efficiency can be formulated, and by using the general form of n_i in (2-3), (2-3) this current gain is

$$\beta_\gamma = \frac{I_n}{I_p} = \left[\frac{\mu_{nb}\ W_e\ N_e\ n_{ib0}^2}{\mu_{pe}\ W_b\ N_b\ n_{ie0}^2} \right] e^{\left(\frac{E_{ge} - E_{gb}}{V_T} \right)} \tag{2-25}$$

Another parameter, the base transport factor, α,describes the amount of emitter injected electrons which successfully diffuse through the quasi-neutral base and are collected at the collector. The electrons which do not diffuse to the collector recombine in the base and form I_{br}. The base transport factor is

$$\alpha = \frac{I_n - I_{br}}{I_n} \tag{2-26}$$

The gain which describes this mechanism is

$$\beta_\alpha = \frac{I_n - I_{br}}{I_{br}} = \frac{I_n}{I_{br}} - 1 = 2\left[\frac{L_{nb}}{W_b} \right]^2 - 1 \tag{2-27}$$

where

$$L_{nb} = \sqrt{V_T\ \mu_{nb}\ \tau_{nb}} \tag{2-28}$$

is the electron diffusion length in the base. A third gain which describes the surface and

depletion region recombination current is

$$\beta_{sr} = \frac{I_n}{I_{sr}} = \left[\frac{2\ V_T\ A_e\ \mu_{nb}\ n_{ib0}^{\ 2}}{N_b W_b A_s\ S\ n_{ie0}^{\ 1}} \right] T^{\left(\frac{3}{2}\right)} e^{\left(\frac{(E_{ge}/2)-E_{gb}}{V_T}\right)} e^{\left(\frac{V_{be}}{2V_T}\right)} \quad (2\text{-}29)$$

These three gains combine together in a parallel fashion were the total forward current gain is limited by the smallest of the three gains:

$$\beta_f = \frac{I_c}{I_b} = \frac{1}{\frac{1}{\beta_\gamma} + \frac{1}{\beta_\alpha} + \frac{1}{\beta_{sr}}} \quad (2\text{-}30)$$

The change in these current gains with T will be examined in detail during the BJT and HBT specific analyses.

2.2.4 Small Signal Elements

The small signal equivalent circuit elements [24,42,43] will also change with temperature, affecting its high frequency performance for the bipolar transistor. The three most important intrinsic elements are the base-emitter small signal resistance, R_{eb}, the transconductance, gm, and the base-emitter capacitance, C_{eb}.

The small signal base-emitter resistance is given by

$$R_{eb} = \frac{\Delta V_{be}}{\Delta I_b} \quad (2\text{-}31)$$

As determined earlier, for a constant V_{be}, I_b will increase exponentially with T. Therefore for a given change in V_{be}, the change in I_{be} will increase causing R_{eb} to decrease exponentially with T.

The transconductance is

$$gm = \frac{\Delta I_c}{\Delta V_{be}} \qquad (2\text{-}32)$$

and for similar reasons will increase exponentially with T.

C_{eb} is given by the slightly more involved expression:

$$C_{eb} = C_{je} + gm\ \tau_b \qquad (2\text{-}33)$$

The components of C_{eb} are given by

$$C_{je} = \frac{A_e \epsilon_0 \epsilon_r}{X_d} \qquad (2\text{-}34)$$

$$X_d = \sqrt{\frac{2\epsilon_0 \epsilon_r (N_e + N_b)(V_{bi} - V_{be})}{q N_e N_b}} \qquad (2\text{-}35)$$

$$V_{bi} = V_T\ \ln\left[\frac{N_b N_e}{n_i^2}\right] \qquad (2\text{-}36)$$

$$\tau_b = \frac{W_b^2}{2 V_T\ \mu_{nb}} + \frac{W_b}{v_{sat}} \qquad (2\text{-}37)$$

where C_{je} is the base-emitter depletion region capacitance, X_d is the depletion region width, V_{bi} is the junction built in voltage, and τ_b is the base transit time. Both terms in τ_b will increase with temperature causing the $gm\tau_b$ term in C_{eb} to increase. V_{bi} will increase with T because of the n_i^2 term, therefore X_d will decrease, and C_{je} will increase.

C_{cb} will then increase with T. A specific evaluation of these terms for the AlGaAs/GaAs HBT is presented in Section 4.3.2.

2.2.5 Parasitic Resistances

Parasitic resistances [15,43,44] can have a significant effect on the performance of a transistor, in fact the parasitic base resistance strongly affects the maximum frequency of oscillation. The majority of parasitic resistance is proportional to the bulk resistivity, ρ, of the particular region, which is given by

$$\rho=\frac{1}{\sigma}=\frac{1}{q\ (\mu_n n+\mu_p p)} \tag{2-38}$$

If n-type doping is assumed at a concentration N_D, resistivity can be expressed as

$$\rho=\frac{1}{q\left(\mu_n N_D+\mu_p \frac{n_i^2}{N_D}\right)} \tag{2-39}$$

Only for very high temperatures, and very low doping is the n_i^2 term important, and for the temperatures considered here, ρ is proportional to μ_n^{-1}, and therefore increases with T. Actual calculations indicate that for Si, resistivity increases by approximately 10 to 45% every 100°C, while for GaAs it increases by 50 to 150% every 100°C.

2.3 SPECIFIC BJT AND HBT ANALYSIS

Table 2-3 shows the relative importance [23,24,43,45] of each current considered earlier for the BJT and for the HBT. Arrows are added to stress the most important differences between the two types. For the BJT, the base current is composed mainly of I_p which has been found to have an $e^{(Vbe/VT)}$ dependence which is the same as the collector current dependence. For the HBT, however, I_{sr} often dominates in the base current, causing it to have nearly an $e^{(Vbe/2VT)}$ dependence. Actual measured characteristics fit an $e^{(Vbe/nVT)}$ where the ideality factor, n, describes the log-linear slope of the current versus V_{be}. Figure 2-6 is a Gummel plot for an HBT, which shows the ideality factors for the collector and base current are approximately 1 and 2 respectively.

Current:	Transistor Type		Affected Gain
	HBT	BJT	
I_n	****	****	All
I_p -->	*	***	β_γ
I_{br}	**	**	β_α
I_{dr}	**	*	β_{sr}
I_{sr} -->	***	*	

Table 2-3. Relative importance of various currents for the HBT and BJT.

2.3.1 BJT

As can be seen in the energy-band diagram for the BJT in Figure 2-7, the barrier for electrons from emitter to base is roughly the same magnitude as the barrier for holes from base to emitter. Since this barrier to holes is quite small, the hole current I_p

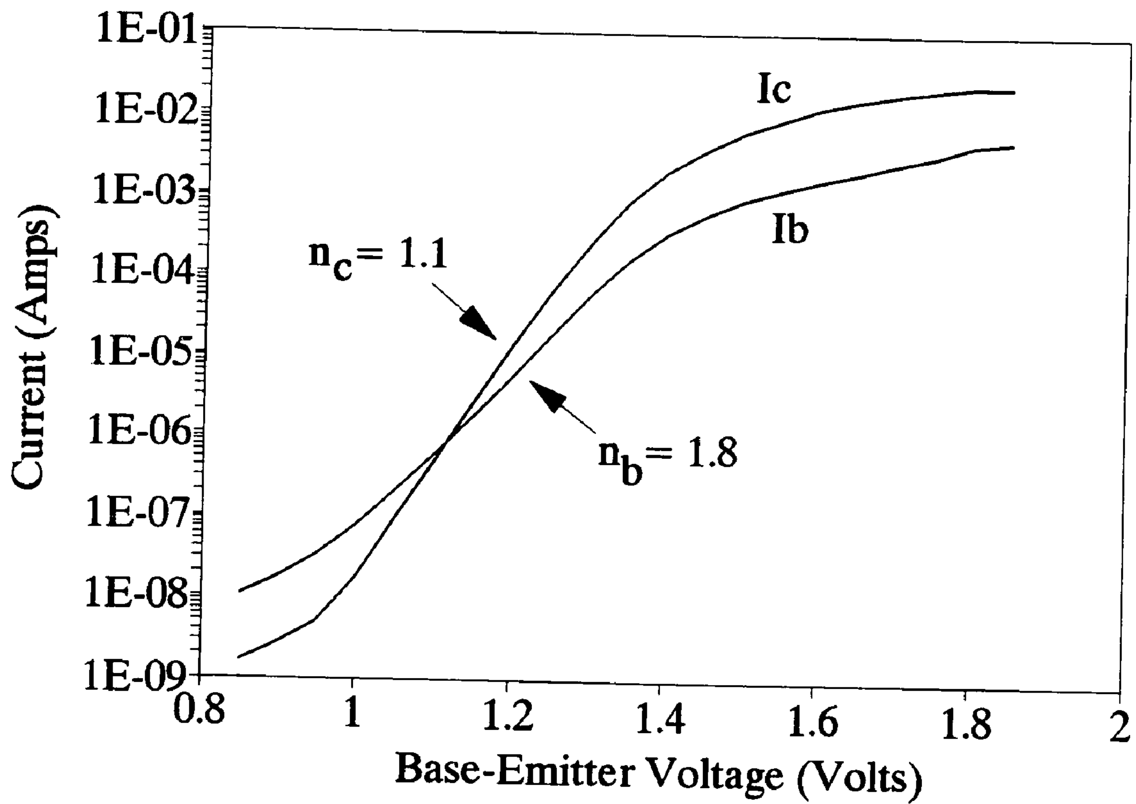

Figure 2-6. Gummel plot for an HBT showing the base and collector ideality factors.

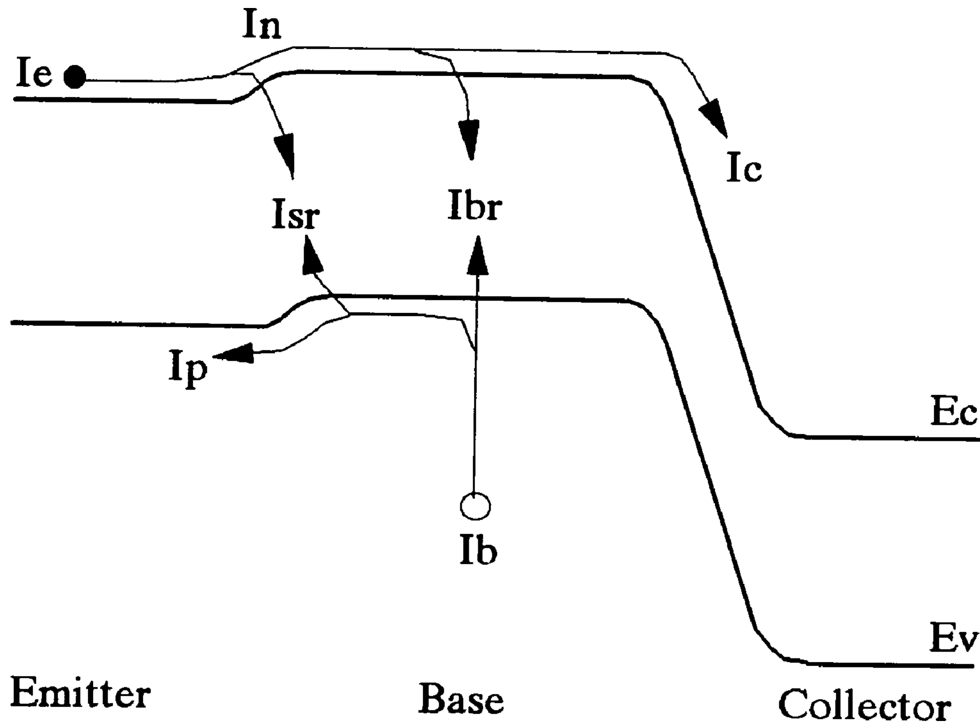

Figure 2-7. Energy band diagram of homojunction bipolar junction transistor.

dominates over the neutral base and depletion region recombination currents. This in turn indicates that the emitter efficiency gain, β_γ, is the limiting gain term. Therefore, to achieve high current gains, the emitter to base doping ratio should be large, as seen in the equation for β_γ repeated below. This implies a very high emitter doping.

$$\beta_\gamma = \frac{I_n}{I_p} = \left[\frac{\mu_{nb}\, W_e\, N_e\, n_{ib0}^2}{\mu_{pe}\, W_b\, N_b\, n_{ie0}^2} \right] e^{\left(\frac{E_{ge} - E_{gb}}{V_T} \right)} \tag{2-40}$$

Figure 2-8 shows a typical planar double-diffused BJT structure were the emitter, base, and collector doping are n++,p+,and n respectively. Unfortunately, the high doping required in the emitter enhances coulomb interaction between the abundant excess electrons and causes the emitter bandgap to decrease [26,46-49]. In this condition, the emitter has a smaller bandgap than the base, increasing the barrier for electrons and decreasing the barrier for holes. This reduces gain exponentially as seen in (2-40). Therefore, for increasing emitter doping there is a point of diminishing return in terms of current gain. Finally, due to this change in bandgap an exponential temperature dependence is present in the gain.

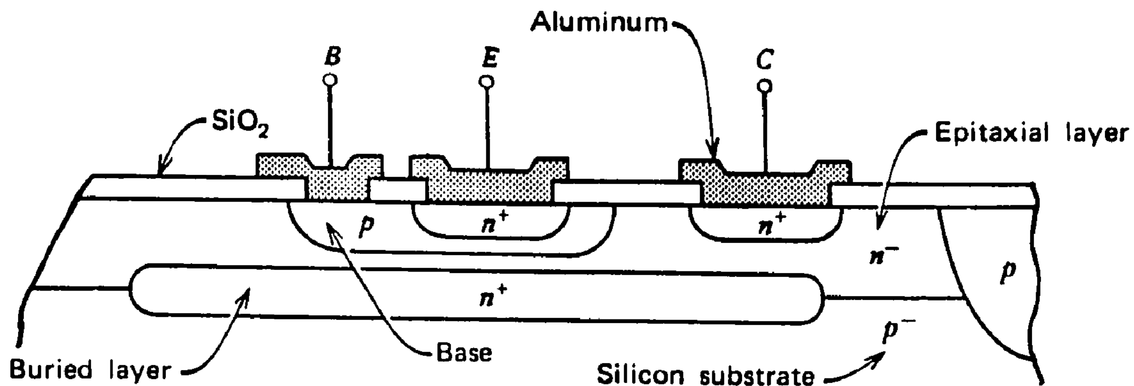

Figure 2-8. Cross section of a typical double-diffused BJT.

For a typical emitter doping of $5x10^{20}$ cm^{-3} the change in bandgap has been measured to be 0.02 eV [50]. When this small change in bandgap is used in β_γ it causes this gain to be reduced by 55% as compared to the ideal case of no change in bandgap. Figure 2-9 illustrates this gain reduction as well as the associated positive temperature dependence for a device with an otherwise ideal gain of 500. This temperature dependence is given by

$$\beta_\gamma \propto e^{\left(\frac{-0.02}{V_T}\right)} \qquad (2\text{-}41)$$

As mentioned earlier, at a constant base-emitter voltage all the currents have essentially an exponentially increasing dependence on temperature as seen in Figure 2-10.

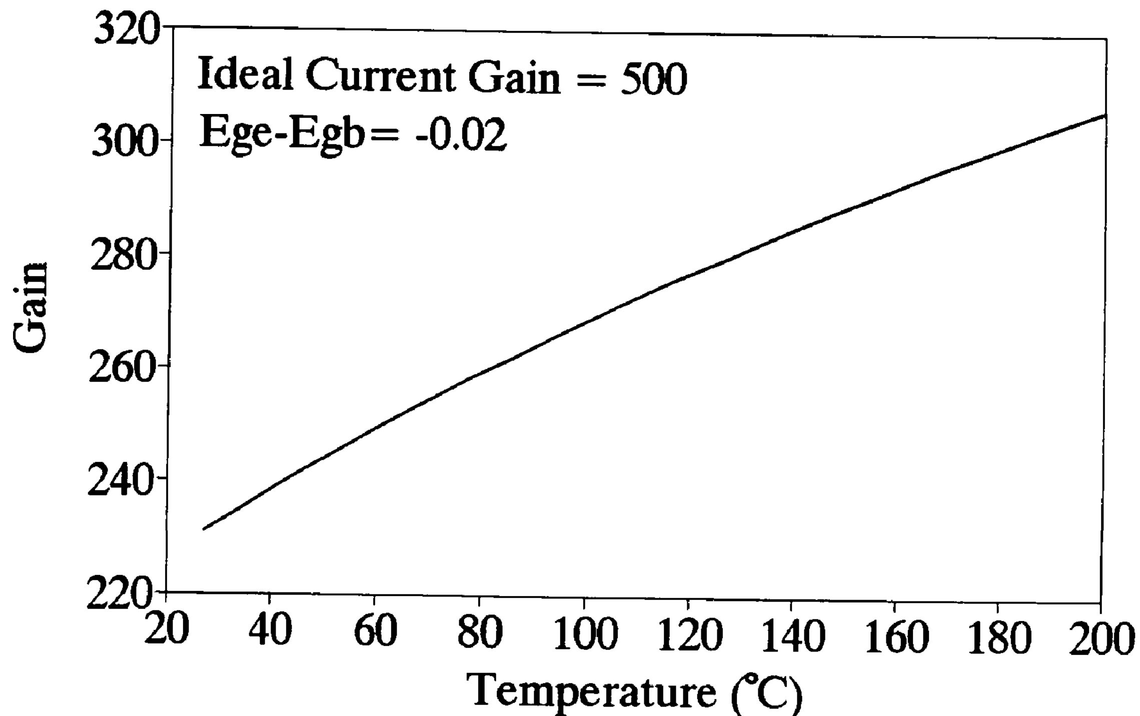

Figure 2-9. Temperature dependence of current gain for a BJT where high emitter doping has caused a base-emitter change in bandgap.

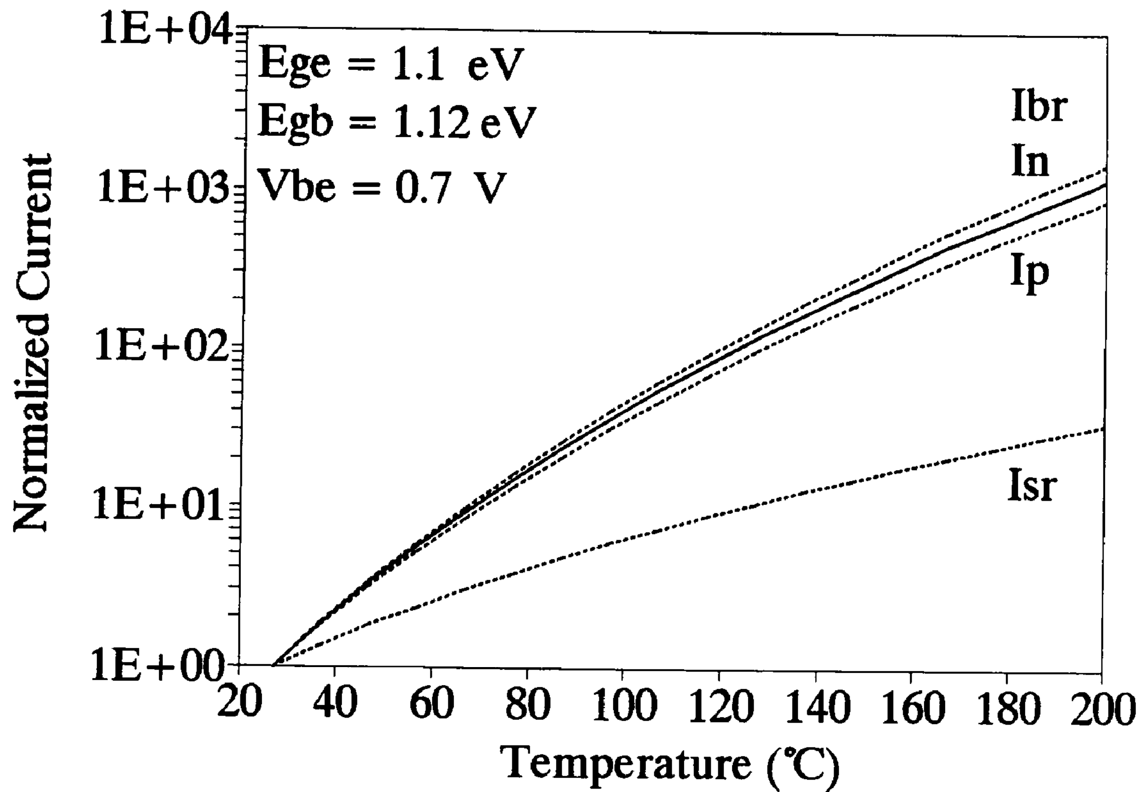

Figure 2-10. Calculations of the temperature dependence of the BJT current components assuming a 0.02 eV change in base-emitter bandgap.

On a linear scale, Figure 2-11 shows SPICE [51] simulations of the base diode characteristics at various temperatures also showing this large exponential increase. Also, at a constant current, the base-emitter voltage decreases linearly with temperature. Figure 2-12 shows a series of actual measurements [52] of V_{be} at elevated temperatures, while Figure 2-13 shows the calculated temperature dependence of V_{be} for the various currents components.

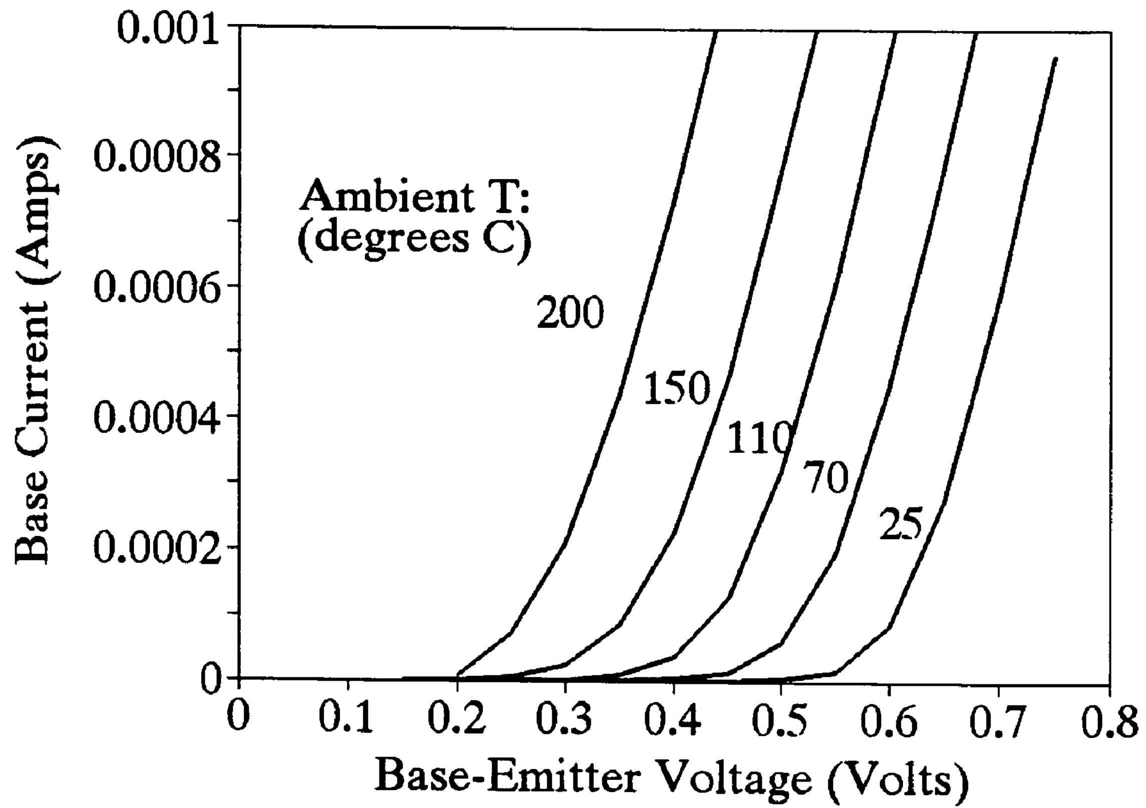

Figure 2-11. SPICE simulation of I_b for a BJT at different ambient temperatures.

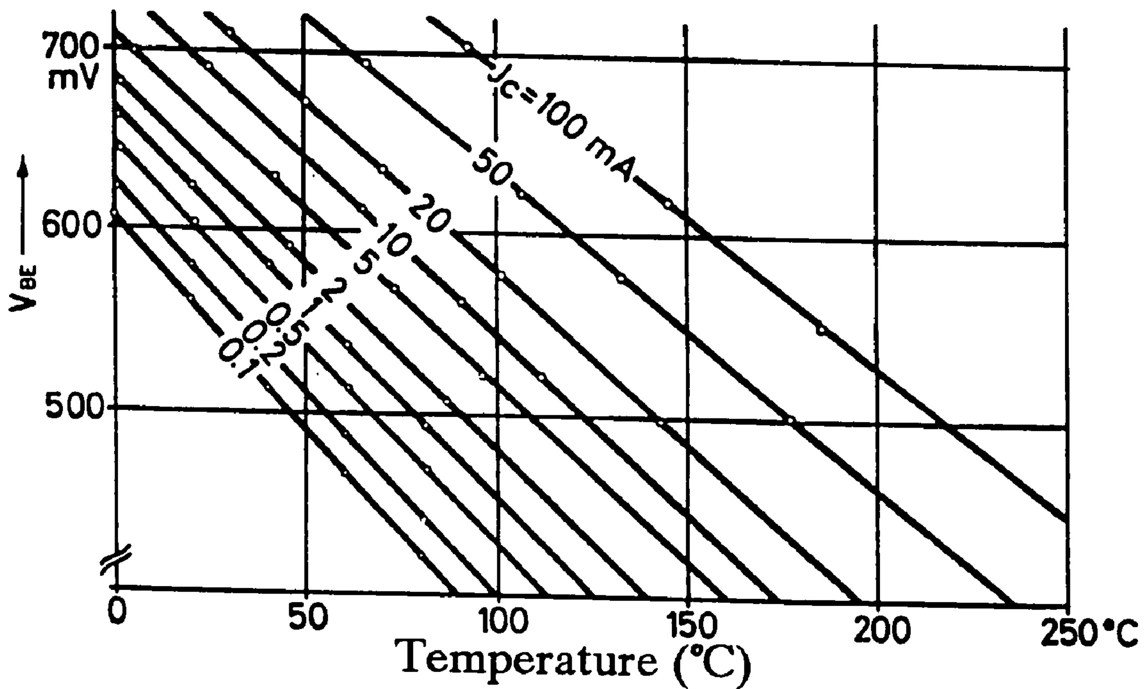

Figure 2-12. Measurements of the temperature dependence of V_{be} for a BJT.

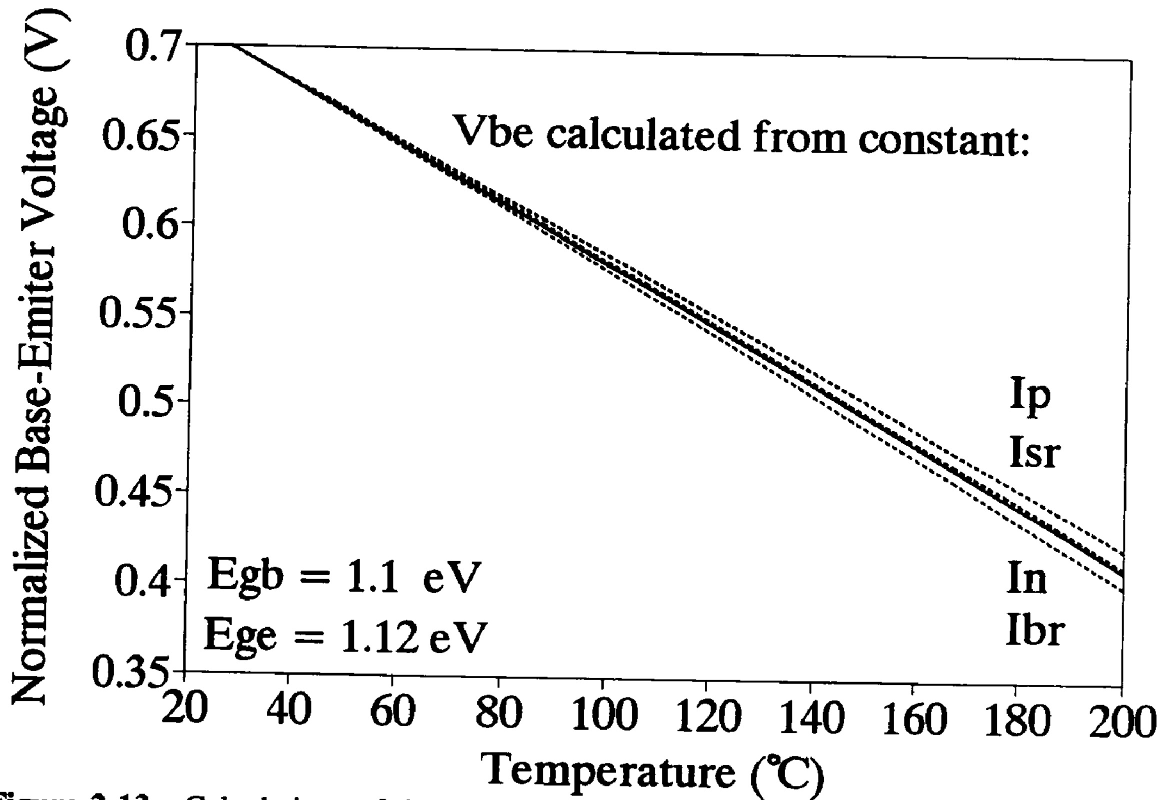

Figure 2-13. Calculations of the temperature dependence of V_{be} for the BJT currents.

There are several consequences of these temperature dependencies. First, the linear dependence of V_{be} on T has been used widely for very accurate active temperature sensors [53-55]. This type of temperature sensing requires calibration of the particular I-V characteristics [52], and is an excellent method of measuring the chip or wafer ambient temperature.

In terms of gain, the BJT has been shown to have reduced performance as temperature decreases. Although not included in this analysis, this reduction does continue below room temperature for conventional structures, and is of concern for circuits intended to operate in this temperature range. The incentive for low temperature operation of any circuit is increased power-delay performance, and reliability [43]. FET

circuits have numerous device related advantages below room temperature and the popular integration of BJTs and FETs (BiCMOS) has brought about the desire to improve the BJT low temperature performance [47].

On the other end of the spectrum, as temperature increases, gain increases. This can cause reliability problems where there is current crowding, and local heating. This 'hot spot' will have an increased gain, and therefore conduct even more current causing a positive feedback situation called thermal runaway. This can very quickly burn out a device. Emitter ballasting resistors can be added to help evenly distribute currents in multi-finger transistors [15].

2.3.2 HBT

As seen in the band-diagram of Figure 2-14, the HBT has a much larger barrier for holes than for electrons [30,56]. This is caused by forming the emitter from a material with a larger bandgap than that of the base. Within β_{α}, this bandgap difference (E_{ge} -E_{gb}) appears in an exponential which is typically about 1×10^5. As a result, the emitter-base doping ratio no longer has to be large in order to achieve a large emitter efficiency. In fact, the base can be doped much greater than the emitter. A large base doping allows the base width to be decreased without increasing the parasitic base resistance. Figure 2-15 shows a typical HBT structure with an n+ wide-bandgap emitter, a p++ base and an n- collector.

Since the emitter efficiency gain is very high, β_{sr} and β_{α} are the limiting factors to the overall gain [56,57]. These gains are due to surface and neutral base recombination respectively. Depending on the effectiveness of surface passivation, either

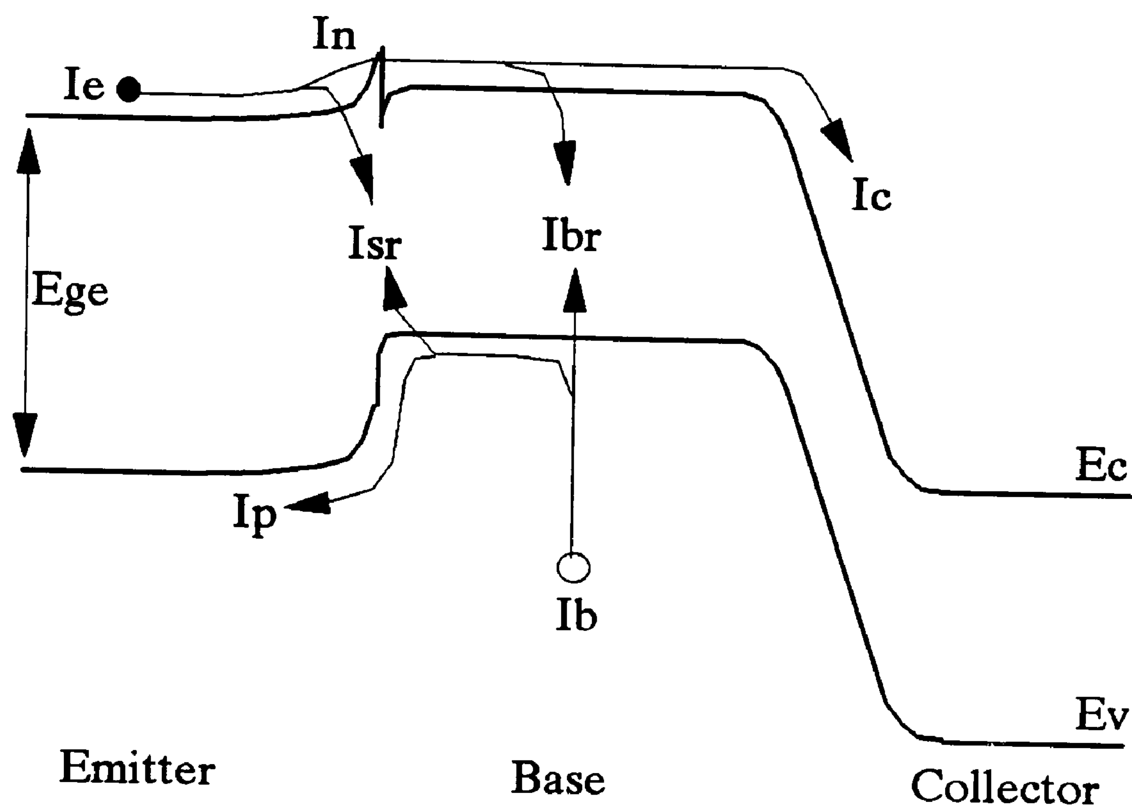

Figure 2-14. Energy band diagram for an HBT.

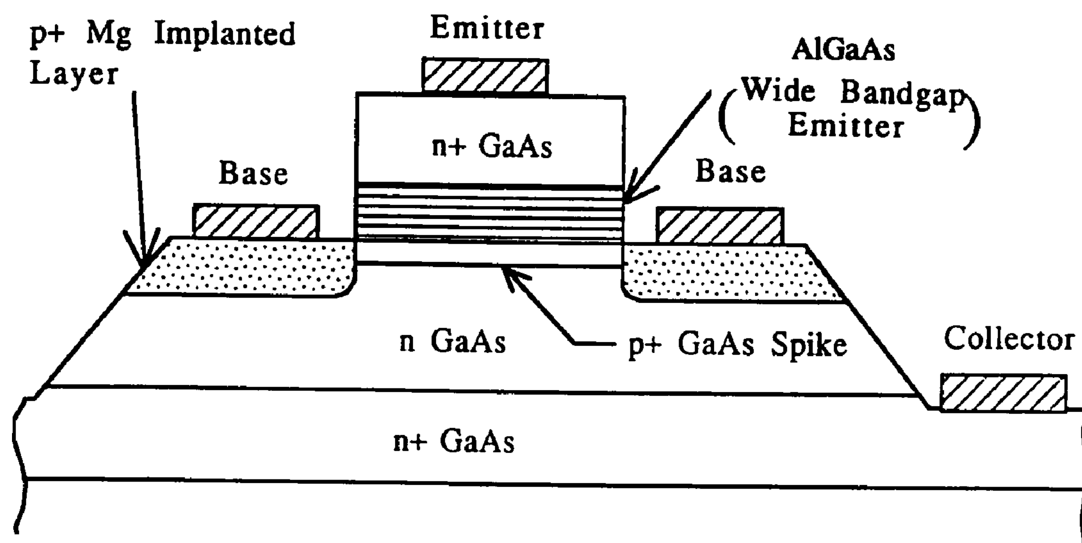

Figure 2-15. Cross section of an AlGaAs/GaAs HBT.

one could be dominant, but certainly at low V_{be} the surface recombination will always dominate because of its $e^{(Vbe/2kT)}$ dependence. Therefore, it is important to analyze the temperature dependence of both β_{sr} and β_{α}.

Within β_{α}, (2-27), L_{nb}^2 is dependent on temperature through the term $V_T\mu_{np}$. For GaAs, therefore, β_{α} is proportional to $T^{-1.3}$. β_{sr} has a more complicated temperature dependance. Its temperature dependent elements are V_T ($\propto T$), μ_{nb} ($\propto T^{-2.3}$)and two exponentials of T. By using the temperature dependencies of (2-16) and (2-19), the overall dependence can be easily evaluated. For the $Al_{0.25}Ga_{0.75}As$ - GaAs system, it is

$$\beta_{sr} \propto T^{0.2} e^{\left(\frac{0.19}{V_T}\right)} \tag{2-42}$$

where the change in bandgap with temperature has not been noted. Figure 2-16 shows calculations of all three gains for the HBT as well as the combined gain β_f taking into account all temperature dependencies including the bandgap change. Notice that the gain *decreases* with temperature which is the opposite behavior from the BJT. This is due to the fact that the change in base-emitter bandgap for these two types are of different signs. In addition, note that for this particular device, I_{sr} dominated over I_{br}, however, if the surface recombination can be reduced, β_{α} would dominate, making the total gain less temperature dependent. An artifact of this gain decrease with temperature is the unique feature of the HBT to exhibit negative differential resistance in its collector characteristics as shown in Figure 2-17.

The dependence of the currents on temperature for the HBT has also been calculated and is shown in Figure 2-18. I_p and I_{sr} show similar behavior to that of a BJT.

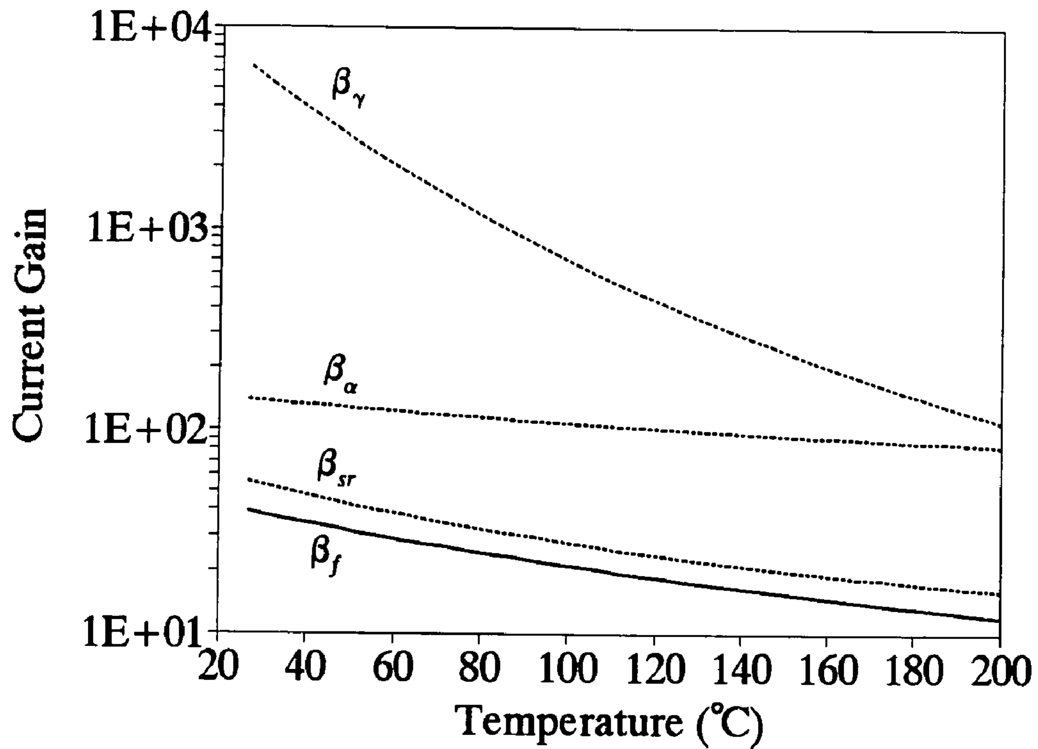

Figure 2-16. Temperature dependence of the components of current gain for the HBT.

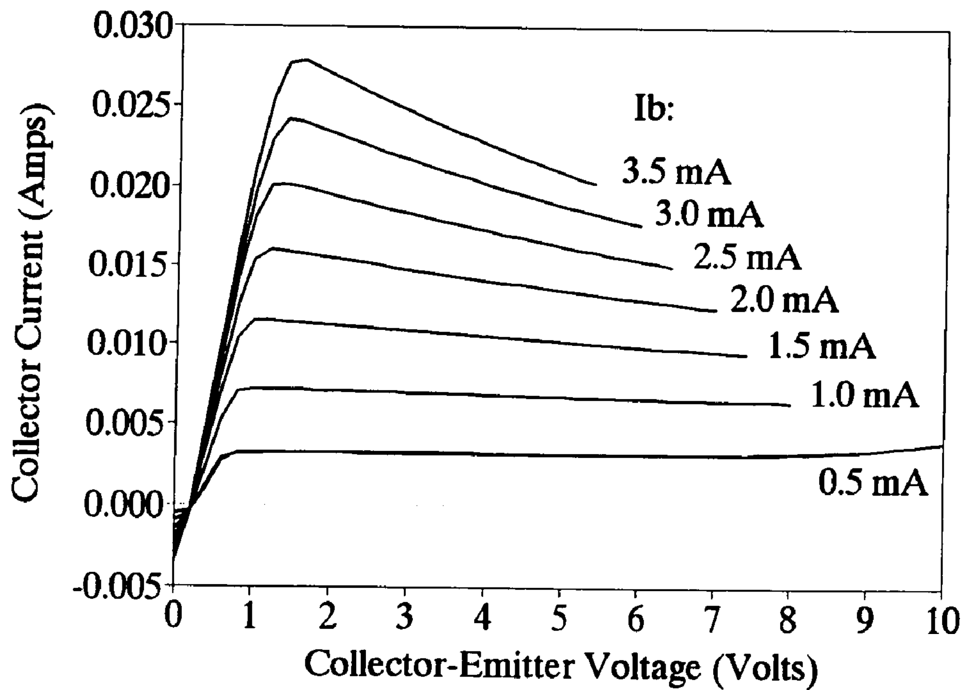

Figure 2-17. Collector characteristics for an HBT in the common emitter configuration.

I_{br} shows a small increase with temperature and I_n actually decreases with temperature. This decreasing I_n results in the observed gain reduction with temperature. Since I_{sr} and I_{br} are the dominant components comprising the base current, the base-emitter characteristics for the HBT have similar characteristics to that of the BJT with exponential $I_b(T)$ and linear $V_{be}(T)$. Figure 2-19 shows calculations of this linear V_{be} change for the various current components. Actual device measurements are presented in Section 3.1.1.

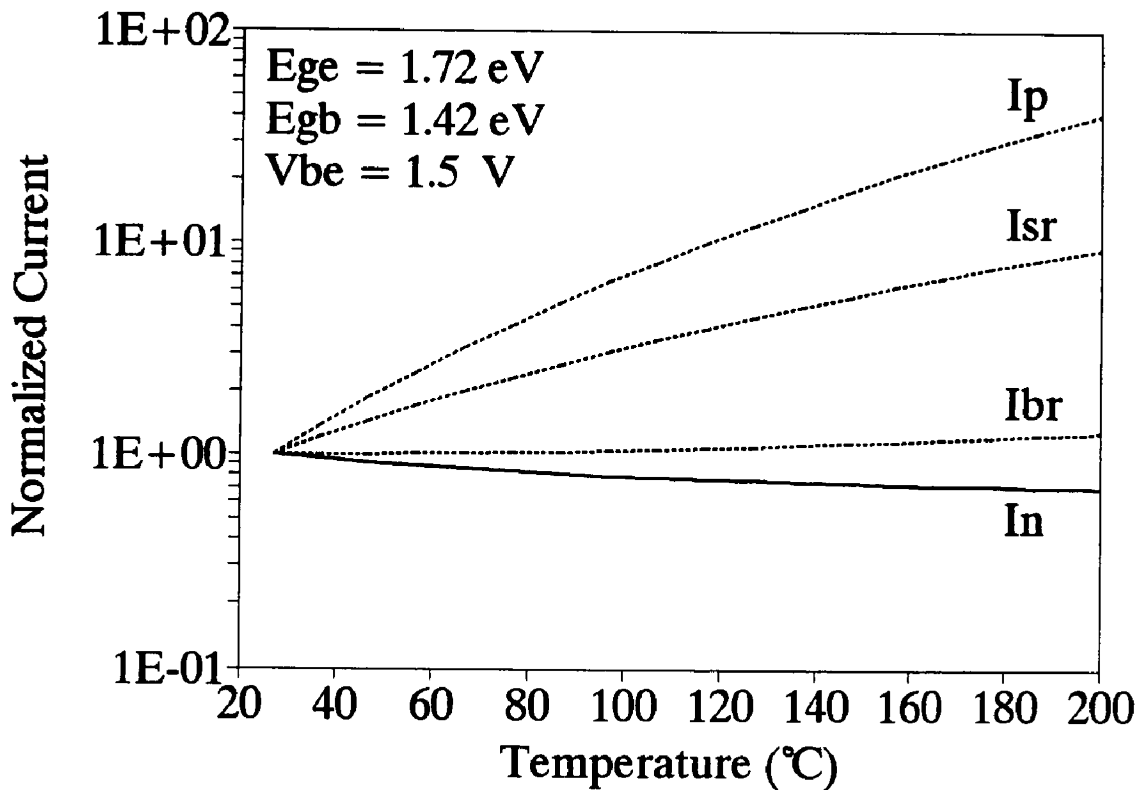

Figure 2-18. Temperature dependence of the current components in an HBT.

As with the BJT, the HBT can also be used to sense temperature using $V_{be}(T)$. This technique is an important one for this work and is used to accurately sense the wafer ambient temperature as described in Section 3.1.3.

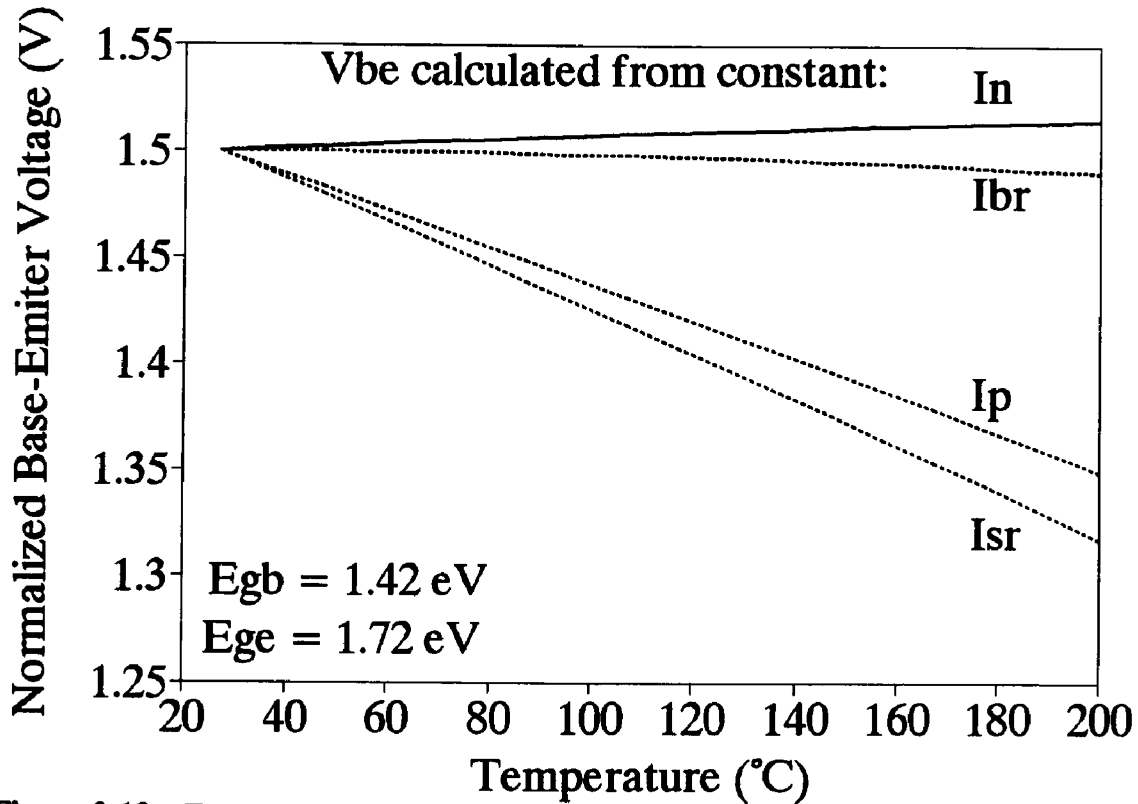

Figure 2-19. Temperature dependence of V_{be} for the current components in an HBT.

As derived earlier, gain decreases with increasing temperature. This causes problems for the high temperature operation of HBTs. In general, compound semiconductor materials such as GaAs have the capability of better high temperature performance than Si because of their wider bandgap. Thus, high temperature operation is a desirable application if the device gain performance can be maintained.

In addition to high ambient temperatures affecting characteristics, self-heating is a significant effect. It is difficult to reduce self-heating for devices based on GaAs because of its high thermal resistivity (three times that of Si). With the current advanced state of material purity and accurate growth techniques, the electrical characteristics of HBTs have optimized well, and ultimately the HBT power performance is limited by the

thermal effects.

Even though gain decreases with temperature, thermal runaway can also occur for the HBT. When it is biased at constant V_{be}, I_b increases exponentially with T and can dominate over any gain decrease with T. Emitter ballasting resistors have also been used for some HBT power transistors, to reduce this problem [58]. Often, however, the standard parasitic contact and bulk emitter resistances are sufficient for this purpose.

2.4 DISCUSSION

It has been shown that for both the BJT and the HBT the effect of temperature plays a very important role in the overall characteristics. As noted, there are exponential as well at power law dependencies on temperature for all of the currents. When forming current gain equations, some of these temperature terms cancel each other out, however, when there is a base-emitter bandgap change there is still a strong temperature dependence. Since the design of the HBT is based upon this bandgap change these effects are of significant importance. Additionally, for the HBT, gain is often limited by surface recombination which has many temperature dependent terms.

Chapter 3
HBT THERMAL EFFECTS ON LOW FREQUENCY CHARACTERISTICS

In this chapter several modeling and characterization techniques are presented which enable the more efficient integration of HBTs into high power circuits. Since self-heating is quite significant in such applications, thermal effects become a limiting factor to performance. Through Pulse testing and dc thermal measurements, it is shown how thermal effects can be quantified and isolated from other gain-degrading effects. This leads to an accurate understanding of the HBT at high power densities and leads to accurate modeling of these effects.

Large signal modeling of the HBT is also presented, where the model includes both base-emitter and current gain thermal effects. It simulates both dc and transient thermal behavior, and can be used for CW microwave operation. This model is useful for simulating device characteristics with different heat-sink configurations, allowing the use of on-wafer measurements to predict packaged device performance. In addition to the simulation of the electrical characteristics, the actual junction temperature is calculated which gives an indication of the thermal limitations of the device in all modes of operation including dc, pulsed and RF.

3.1 EXPERIMENTAL

To fully analyze the thermal effects on the HBT, many types of low frequency measurements have been performed. dc measurements inside of an oven have been

performed to analyze the effect of an elevated ambient and to calibrate the base-emitter I-V characteristics with temperature. Self-heating effects have been characterized for sets of collector current measurements leading to calculations of thermal resistance between the intrinsic base and the external ambient. Pulsed measurements have also been performed to measure device characteristics in the absence of self-heating and leads to an analysis of the device thermal time-constant and associated thermal capacitance.

3.1.1 dc Characterization

When applying dc bias or RF power to a transistor, the power dissipated within the device results in self-heating. This increased junction temperature can be very significant and causes temperature related effects to be significant. As described in Section 2.3.2, one such thermal effect for the HBT is the decrease of current gain with temperature, when the base current is held constant. This was shown in Figure 2-17 as negative differential resistance in measurements of collector characteristics.

The base-emitter I-V characteristics also have a strong dependence on temperature. Figure 3-1 shows measurements of I_b at several elevated ambient temperatures from 20°C to 200°C. . It can be seen that at constant V_{be}, I_b increases drastically with temperature, and was shown in Section 2.2.2 to have an exponential dependence. At constant I_b, this figure shows that V_{be} decreases with temperature. To illustrate this particular dependence more clearly, Figure 3-2 shows a plot of V_{be} versus the ambient temperature for several values of fixed I_b. This change in V_{be} is found to have a linear dependence on temperature of approximately -1.4 mV/°C. This measured

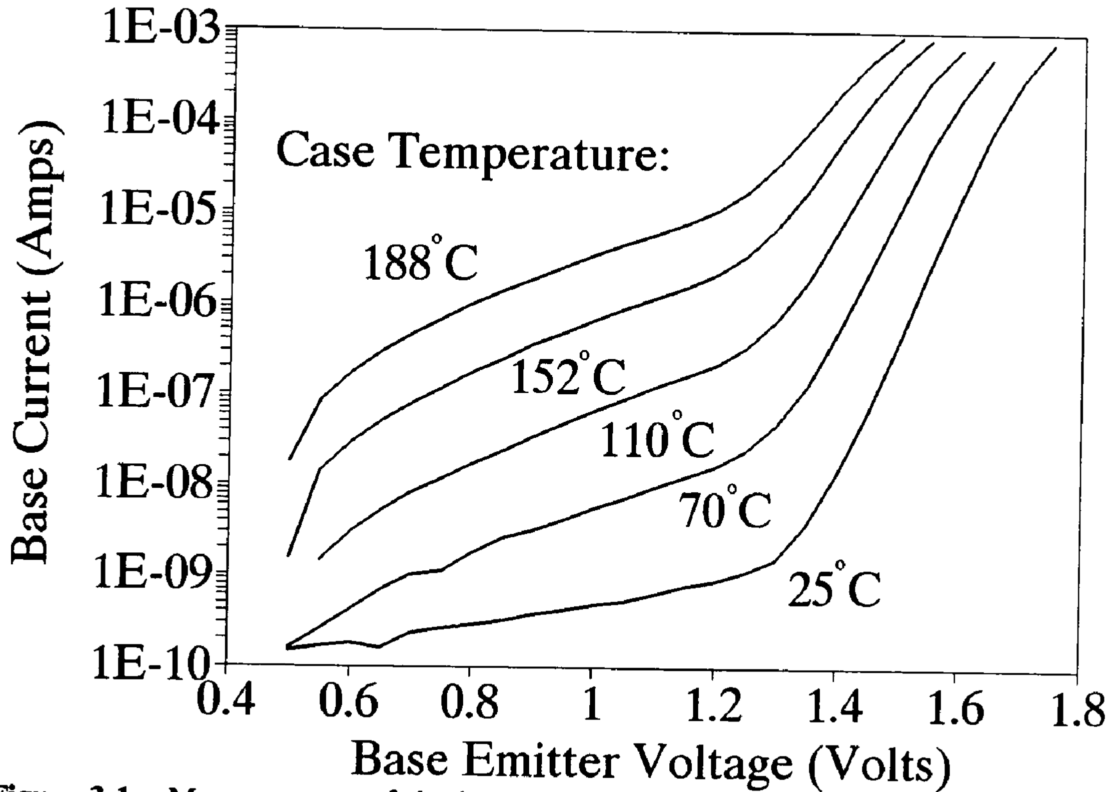

Figure 3-1. Measurements of the base-emitter characteristics for the HBT at several ambient temperatures.

data can be used as a calibration to later calculate the actual junction temperature under normal operating conditions. For this set of data, the collector voltage was chosen to be in the forward active region, but kept at a minimum to limit the power dissipation. V_{be} was, however, found to be largely independent of collector voltage when tests were performed at low power densities where self heating is negligible. This does not hold true for conventional BJTs where an increase in V_{ce} causes the B-C depletion region to increase, and the effective base width to narrow. This decrease in base width, increases both the collector current (Early effect), and base current. In an HBT, the base is always very heavily doped, eliminating any base width modulation, resulting in a constant V_{be}

with collector voltage [59].

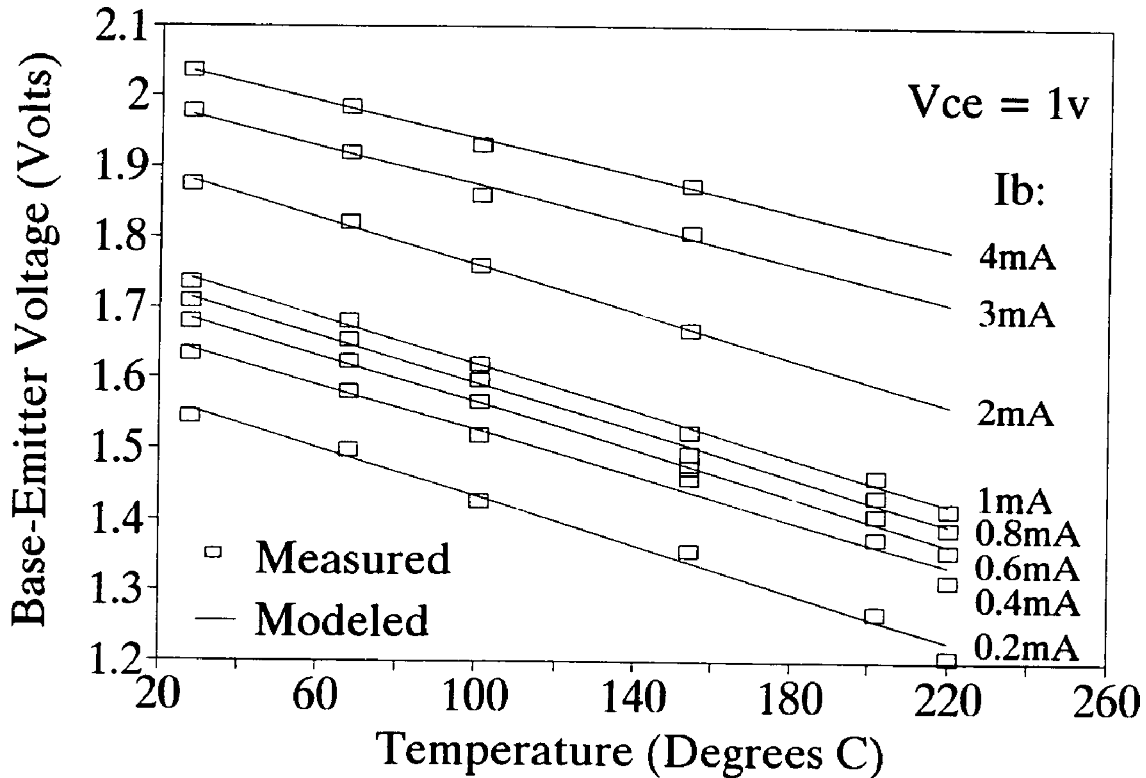

Figure 3-2. Temperature dependence of V_{be} for the HBT at constant base currents.

3.1.2 Pulsed Characterization

To analyze the low-frequency transient thermal effects on the HBT, on-wafer pulsed measurements have been performed on many devices. Figure 3-3 shows the circuit diagram of the pulsed measurement system designed for this work. R_1 and R_2 are used as a voltage divider in order to utilize the full voltage range of the pulse generator. The series combination of these resistors is designed to match the 50 Ω source impedance of the pulse generator. R_B is used to measure I_b using a differential oscilloscope while

the small capacitor C_B stabilizes ringing on the rise and fall of the base pulse. On the collector side, R_C is used to measure the collector current and the large C_C maintains a constant dc voltage reference and is the path for the I_c pulse.

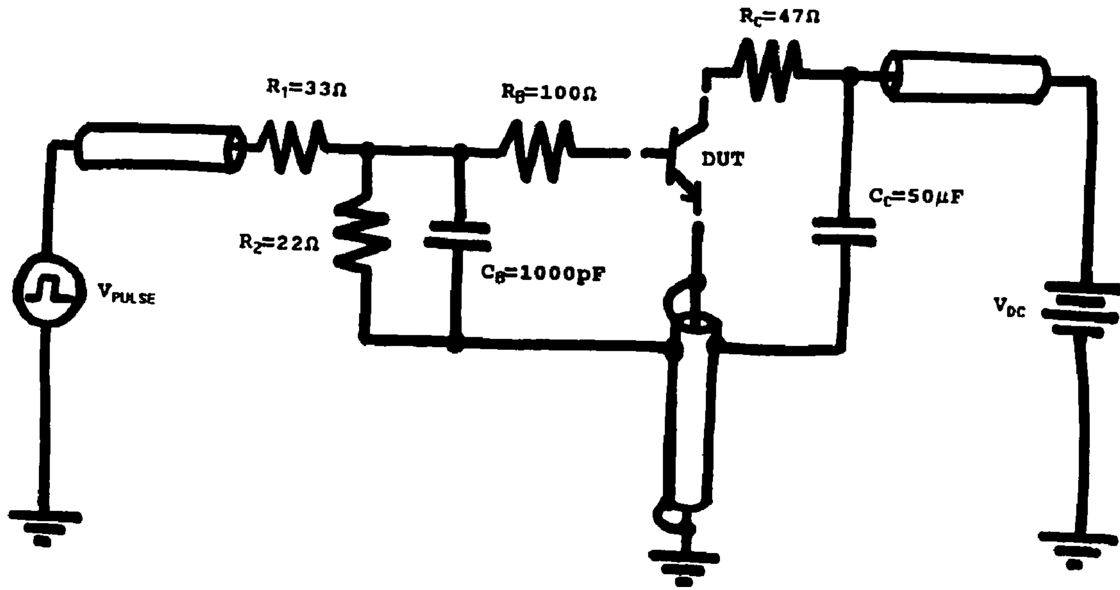

Figure 3-3. 110 ns pulsed measurement system used to measure the HBT collector characteristics.

All pulsed measurements are performed manually using an oscilloscope to ensure accuracy and base and collector current correspondence with time. First, a constant dc voltage is applied to the collector, then base voltage pulses are applied. The pulsed V_{bc} is adjusted to reach the desired I_b, then I_c is measured from the oscilloscope.

To fully understand the behavior of the pulsed HBT characteristics, Figure 3-4 shows the HBT base-emitter diode characteristics using a linear scale. The load line indicated is for the source resistance of the pulse generator. When the base pulse is applied and has reached its maximum, the device V_{bc} has increased to the indicated

100 ns position. At this point, the device has just begun to heat up. This continues for several microseconds until an equilibrium temperature is reached. As the junction heats up, the device's base characteristics change along the source load-line causing V_{be} to decrease and I_b to increase. This can be seen in the waveforms of Figure 3-5 showing the source voltage pulse and the device V_{be}.

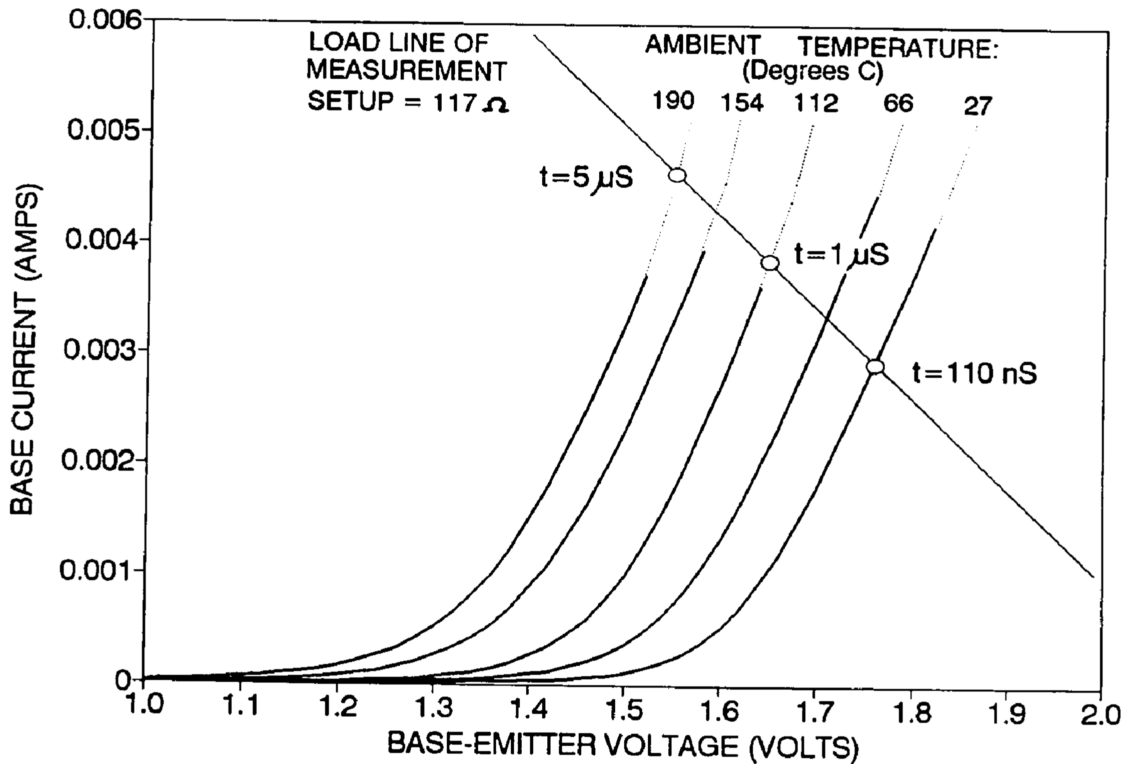

Figure 3-4. Pulsed-source load line superimposed on the HBT base-emitter characteristics at several junction temperatures.

Measurements of I_b and I_c are performed at the time of maximum V_{be} where the junction temperature is still close to the ambient. For these HBTs, this time was approximately 110 ns. Since gain decreases with temperature, I_c is expected to decrease as the device heats up. Figure 3-6 shows this decrease of I_c with a time-constant of about

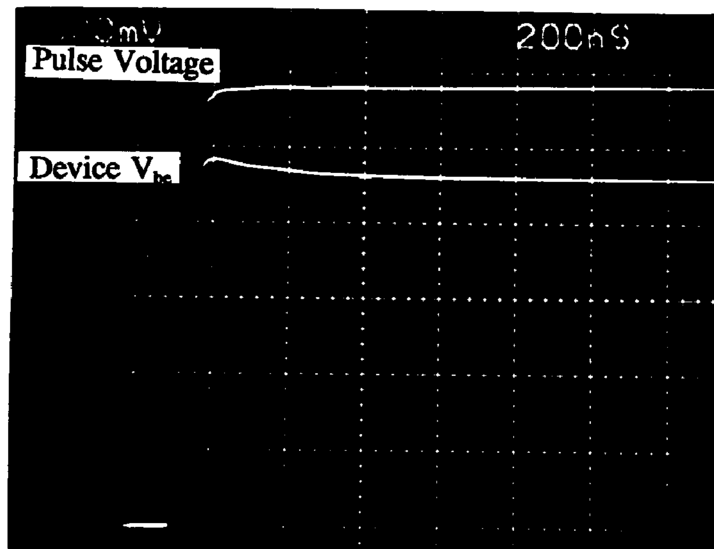

Figure 3-5. Oscilloscope traces of the pulse-generator voltage and the actual V_{be} of the HBT. The V_{be} decrease is caused by the influence of the source load-line during heating.

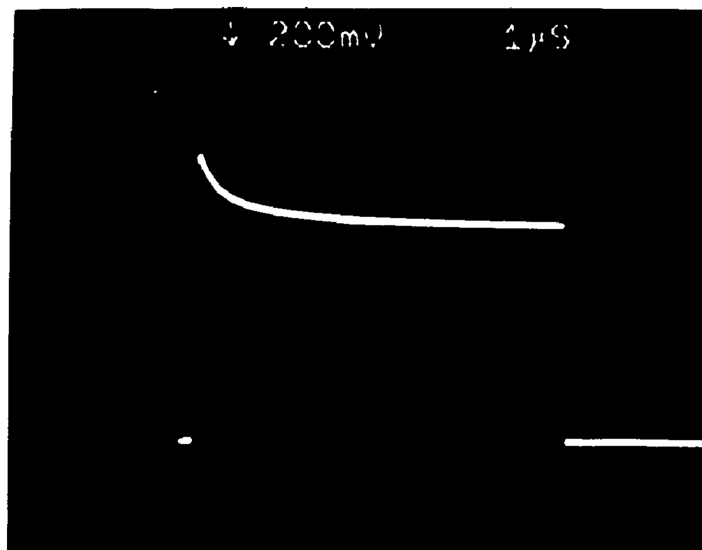

Figure 3-6. Collector current response to a base voltage pulse. The decrease in I_c is caused by self-heating.

0.5μs. In the hot condition, the base current has also risen, therefore gain reduction is even more severe than I_c would indicate. In the measurement setup, the constant collector reference voltage is not directly on the collector, however the real collector voltage is easily calculated from the already measured current through R_C.

Using this measurement system, pulsed collector characteristics were measured by manually adjusting the pulse and bias, and reading values off the oscilloscope. These measurements are shown in Figure 3-7 along with a continuous wave (CW) dc measurement. The solid lines show measurements performed with base pulses of 1μs at a repetition rate of 1 ms and duty cycle of 0.1%. Base and collector current measurements were performed at t=110 ns. The dashed lines show measurements

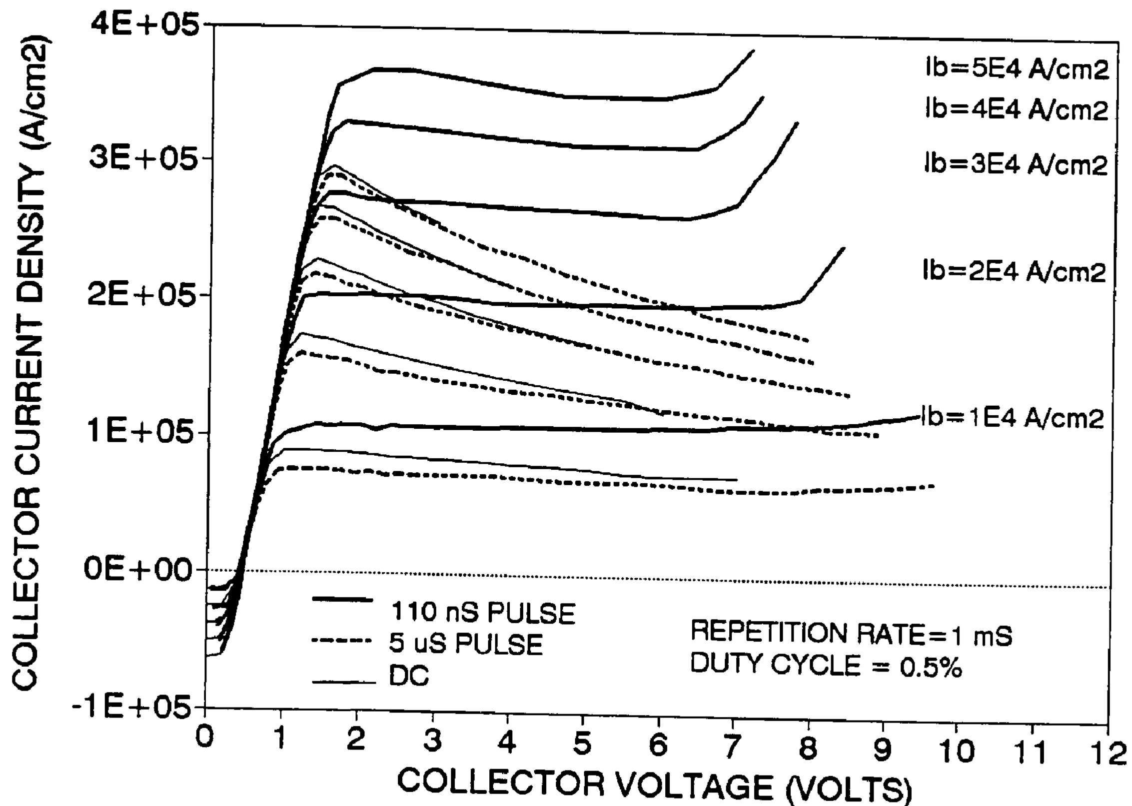

Figure 3-7. Pulsed and dc characteristics of an HBT. The reduction of self-heating causes the pulsed characteristics to show much less negative differential resistance.

performed with base pulses of 5 μs at a repetition rate of 1 ms and duty cycle of 0.5%. Measurements for this case were performed at t=5 μs, when the majority of junction temperature rise was complete.

The dramatic reduction in negative differential resistance for the 110 ns case illustrates the reduction in thermal effects and represents the device's true characteristics in the absence of significant self-heating. The waveforms of Figure 3-8 show that at low power densities, when there is only slight self-heating, the temperature effects are only observable as a slight change in base-emitter characteristics. In this case, the collector current also follows the increasing base current. At high power levels, however, the decrease in collector current is the dominant thermal effect as shown in Figure 3-9.

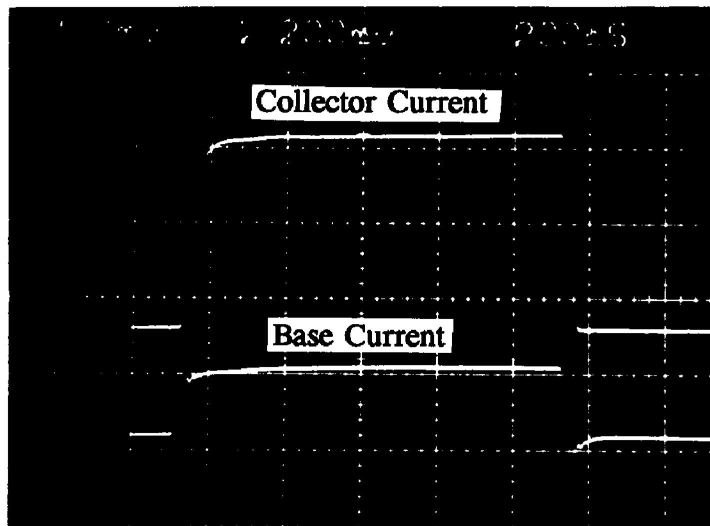

Figure 3-8. HBT pulsed response at low dissipated power (minimal self-heating).

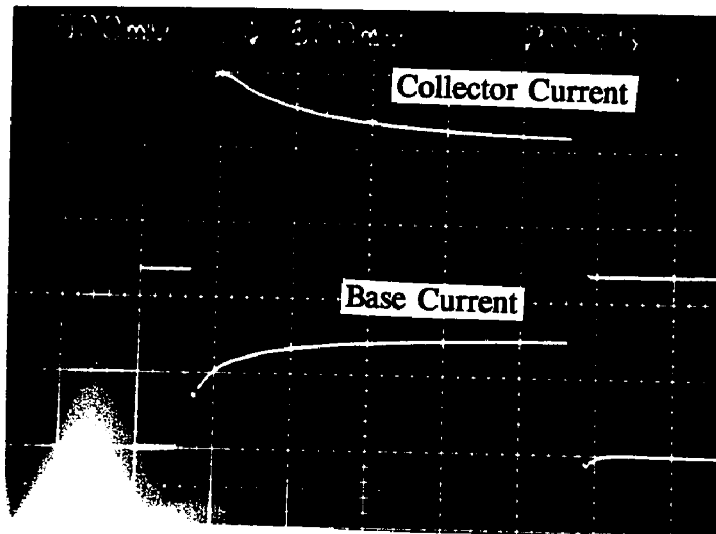

Figure 3-9. HBT pulsed characteristics at high dissipated power (large self-heating).

Since this particular device was subjected to extremely large current and power densities, its gain degraded slightly with each measurement explaining the discrepancy between the dc and 5μs measurements. After the pulsed measurements were completed, an additional dc measurement was performed to confirm this effect as shown in Figure 3-10. This permanent damage is attributed to the well known temperature induced diffusion of the Beryllium doping in the base [60].

3.1.3 Junction Temperature Analysis

Pulsed and dc thermal effects are easily observed for the HBT, but in order to model these effects they must be quantified for a particular HBT. One step toward quantifying these effects is to derive the device's thermal resistance from the intrinsic

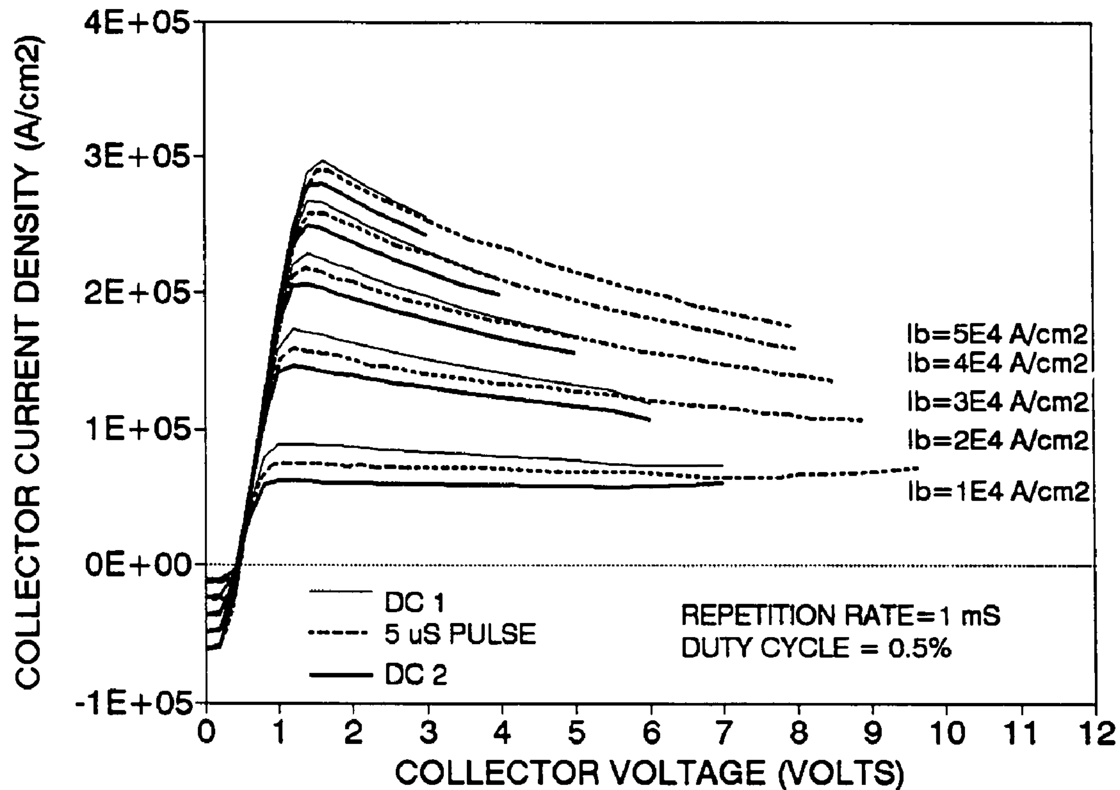

Figure 3-10. Sequential measurements showing a permanent decrease in device gain.

base region to the external ambient environment [61,62]. This thermal resistance (R_{th}) can then be used to calculate the actual junction temperature from the dissipated dc power using the relationship $T=T_0+(R_{th}\ P_{dc})$, where T_0 is the ambient temperature, and P_{dc} is the dc power. Several methods can be utilized to measure R_{th}, including electrical [59,63-66], infrared and visible optical [67,68], and three-dimensional numerical simulations [61,69-71]. In this work, the dc electrical method is used, where the measured base-emitter voltage (V_{be}) was found to be a very accurate indicator of the actual junction temperature [72].

This technique for thermal resistance determination requires two sets of measurements. First, base-emitter diode characteristics are measured in an elevated

temperature ambient. These measurements are a calibration of the device characteristics, noting that with I_b held constant, V_{be} changes linearly with temperature. Next, in a room temperature ambient, dc power is applied to the HBT and the base-emitter characteristics are monitored and used to calculate the actual junction temperature. Many such measurements will lead to an average value of R_{th}.

In a room temperature ambient, the dc collector I-V characteristics were measured into the high-power region. Simultaneously, the base-emitter characteristics were monitored. Figure 3-11 shows the V_{be} characteristics corresponding to the collector I-V plot of Figure 3-12. The decrease in V_{be} with temperature is used in conjunction with

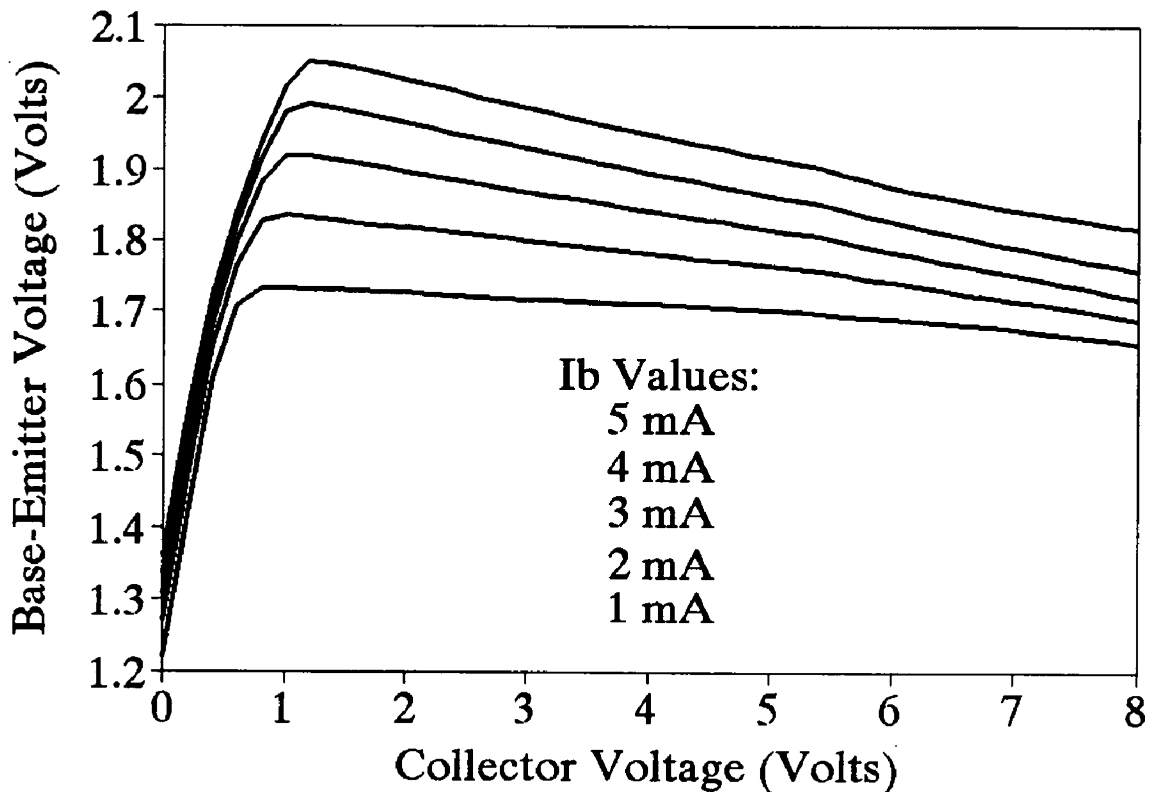

Figure 3-11. V_{be} characteristics of an HBT at constant I_b. V_{be} decreases due to self-heating at high power levels.

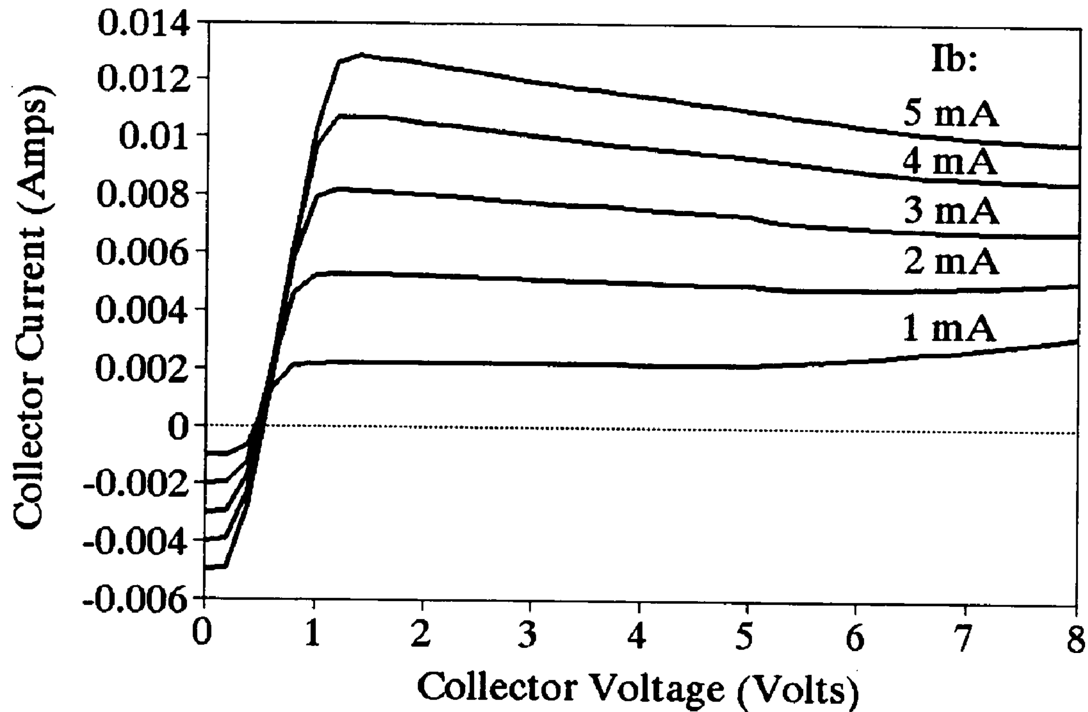

Figure 3-12. Collector current corresponding to the V_{be} measurements of Figure 3-11.

the I_b-V_{be} calibration of Figure 3-2 to calculate the junction temperature at each dc measurement point. Also, the corresponding dissipated power can be computed as $P_{dc}=I_bV_{be}+I_cV_{ce}$. The thermal resistance can be quantified by plotting the calculated junction temperature versus this dc power as shown in Figure 3-13. The average slope of these series of points is the thermal resistance, R_{th}=2.9°C/mW which *is* a high value, but consistent with the low thermal conductivity of GaAs and the thick 25 mil substrate [60].

By using this R_{th}, temperature contours can be drawn on the I-V characteristics to calculate the junction temperature at various power dissipation levels.
as shown in Figure 3-14 indicating a large maximum junction temperature of 250°C.

Also by using R_{th}, a relationship between current gain and junction temperature

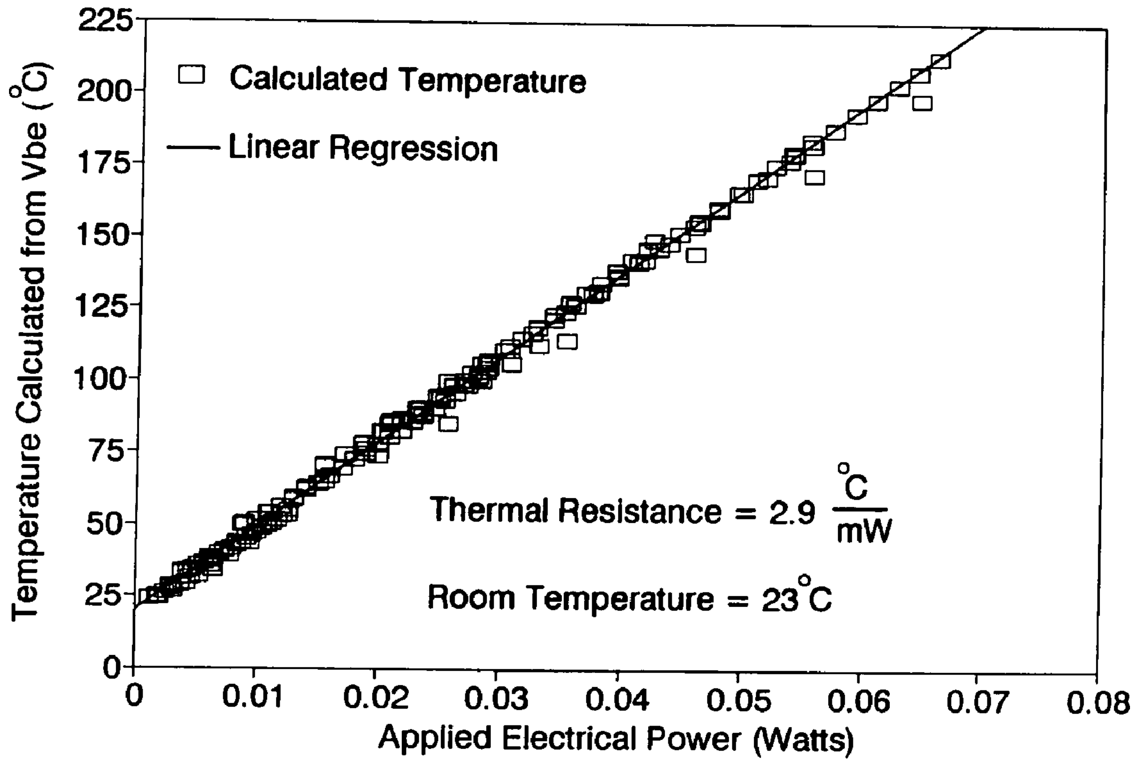

Figure 3-13. Determination of thermal resistance by using calibrated V_{be} characteristics

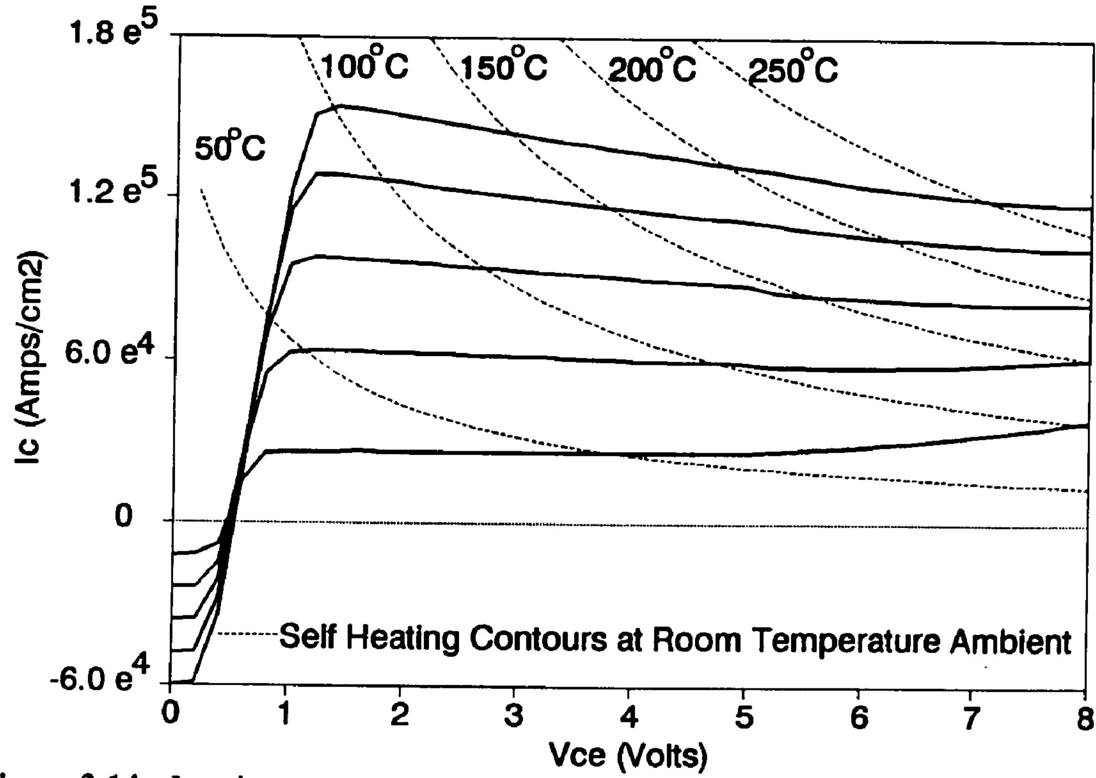

Figure 3-14. Junction temperature contours superimposed on collector characteristics.

can be derived for these characteristics and is shown in Figure 3-15 for $V_{cc}<5$ V. Above 5 V a soft breakdown region masks the intrinsic gain behavior. For modeling purposes, the gain can be seen to have approximately a linear decrease with temperature. In addition, these gain lines can be extrapolated back to room temperature to give the expected gain in the absence of self-heating. In this way, other high current effects can be separated from the thermal effect.

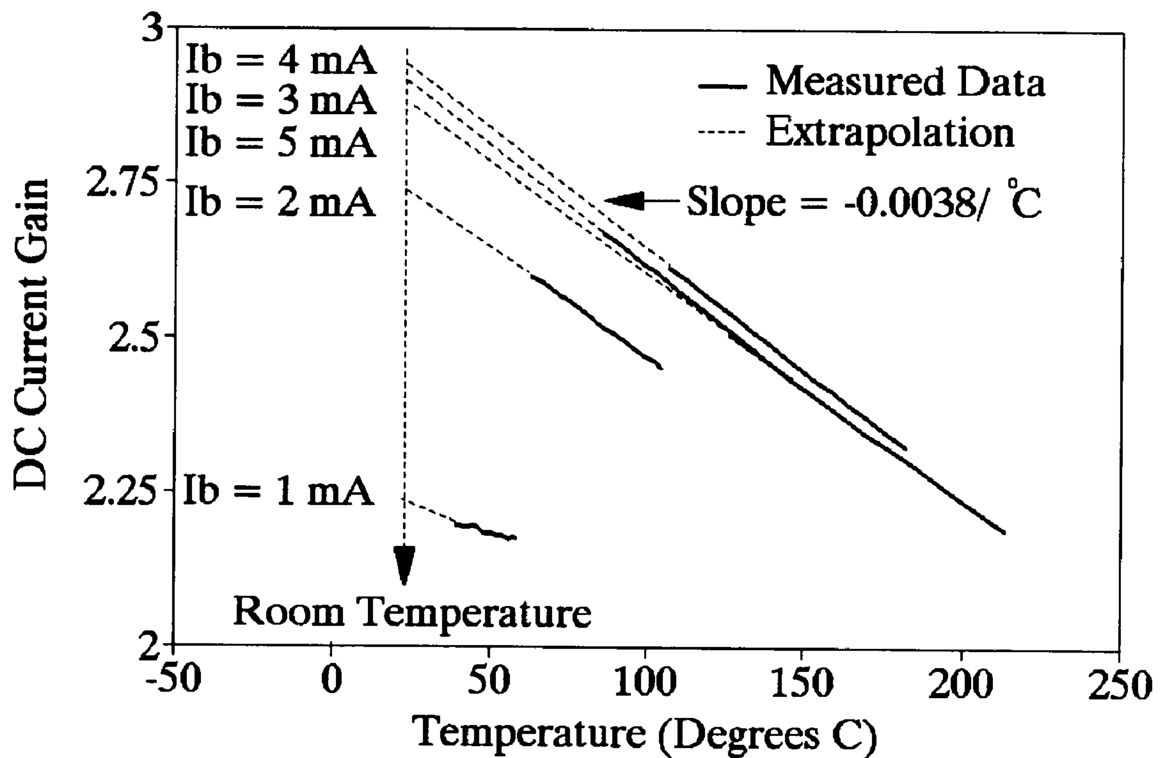

Figure 3-15. Current gain degradation with temperature for the HBT.

Pulsed testing was also performed on this particular device. Collector characteristics were measured in the 110 ns condition, before there was any significant self-heating, and are shown in Figure 3-16. Also shown on the figure are horizontal

lines indicating the extrapolated room temperature predictions derived form the dc thermal measurements. These show excellent agreement with the pulsed characteristics, both of which indicating the device characteristics in the absence of self heating. This agreement ties together well, the dc and pulsed measurement techniques and gives confidence in both methods for determining room temperature device characteristics and thermal parameters.

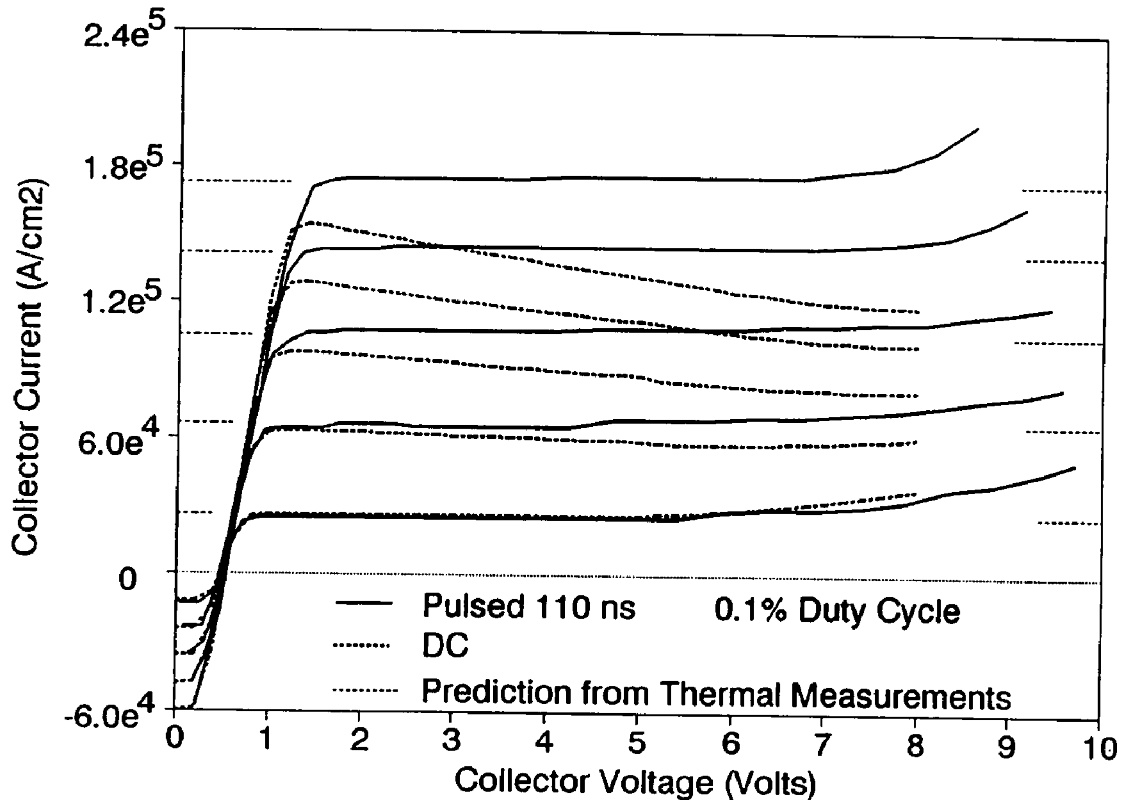

Figure 3-16. Comparison of pulsed measurements and those predicted from dc thermal calculations.

3.2 MODELING

The characterization of thermal effects by dc and pulsed techniques has been utilized by including them into an empirical large-signal model. This model has been

implemented as a user-defined model in the commercial microwave circuit simulation package, LIBRA, from EEsof Inc. [73]. Pulsed and dc characteristics have been simulated and compare well with measured data [74].

3.2.1 Large Signal Model

This hybrid-pi type model, shown in Figure 3-17, has been developed based on the Ebers-Moll topology [23,75], where many transport parameters are extracted from bias-dependent small-signal S-parameter measurements [72]. The base emitter I-V characteristics are simulated as a diode including surface recombination and a bias dependent transit time. The base collector junction is modeled as an intrinsic and an extrinsic reverse-biased diode. The bias-dependence of current gain is modeled with a constant component, plus two components dependent exponentially on I_b. The two exponentials account for the observed decrease in gain at both low and at high base currents.

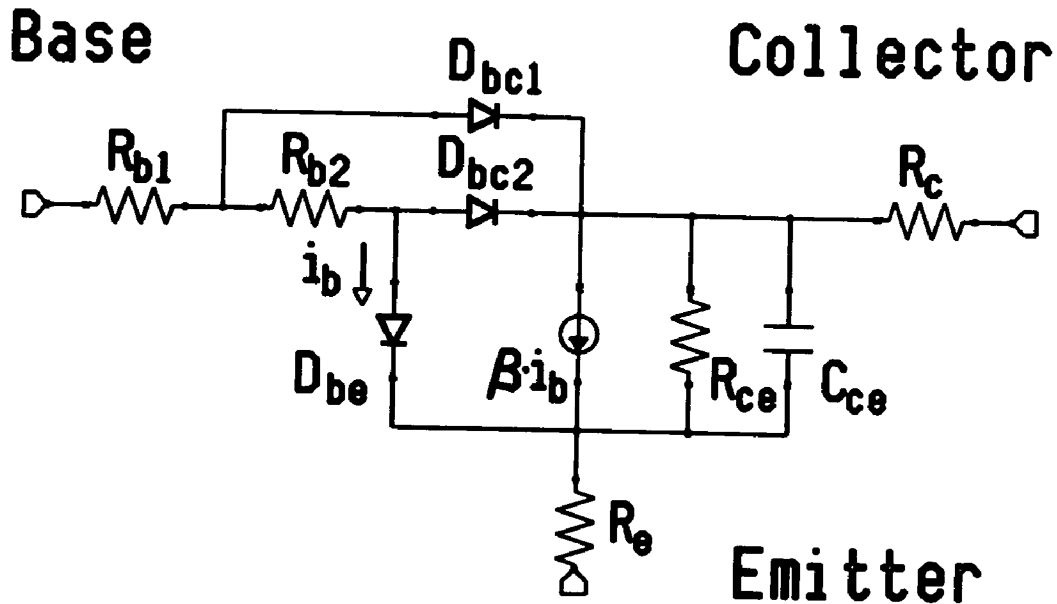

Figure 3-17. Large signal model used for modeling HBT transport and thermal effects.

Parameter extraction was performed to obtain the initial bias dependence of the parameters excluding thermal effects. The current gain, transit times and parasitic emitter and base resistance were extracted form low frequency S-parameters by a simplified equivalent circuit. The parasitic collector resistance and inductance was extracted from S-parameters at the zero collector current offset points at high base currents. The base-collector parameters were extracted from reverse-bias data. Knowing the parasitic parameter values the intrinsic parameter values were evaluated according to the equivalent circuit. Successive steps were used to fit the nonlinear function to the bias-dependent element values. Figure 3-18 illustrates the fitting of current gain, β, where a locus of ten β values from ten sets of S-parameter data are used to define constants in the fitted curve equation.

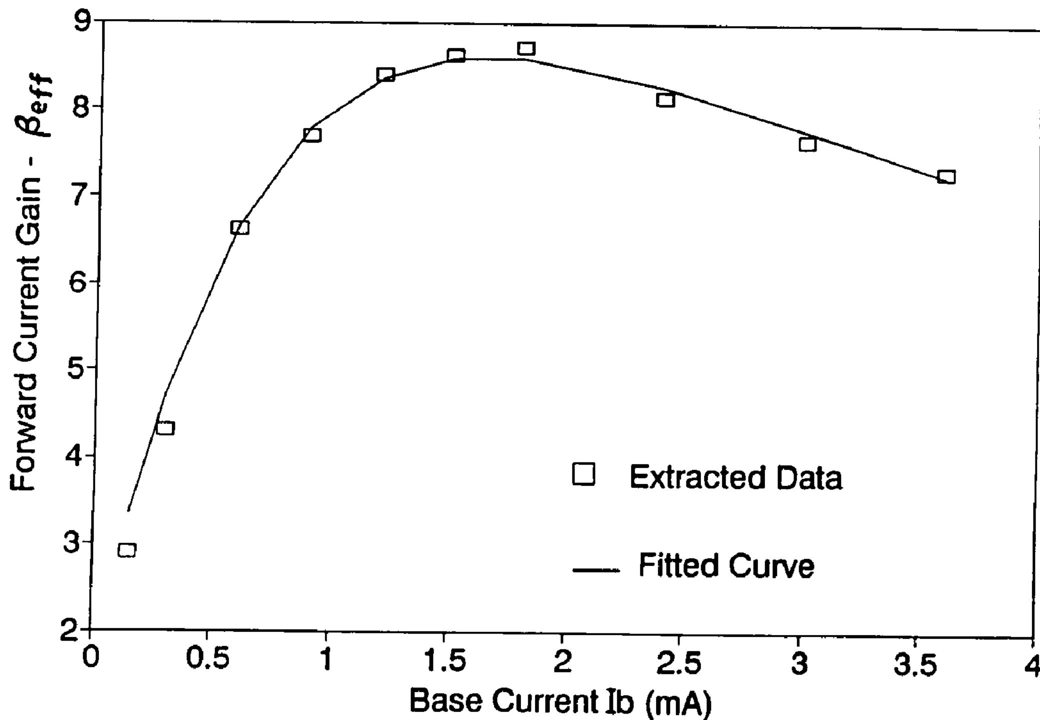

Figure 3-18. Large signal current gain element fit to data extracted from bias-dependent S-parameter measurements.

3.2.2 Incorporation of Thermal Effects

Thermal effects are incorporated into the model equations, based on the observed dc and pulsed I-V characteristics described earlier. Due to the correspondence between electrical and thermal circuits (for example: $V=I \cdot R \Leftrightarrow \text{Temperature}=\text{Power} \cdot R_{th}$) [61,63,76,77], the junction temperature is calculated using a simple R-C circuit shown in Figure 3-19. R_{th} is the thermal resistance calculated earlier, $C_{th}=172$ pF is the thermal capacitance required to obtain the observed thermal time constant of 0.5 μs from pulsed characteristics. The i_{th} current is a time varying source proportional to the power dissipated in the device. I_{th} is a constant source simulating a certain ambient temperature. These applied currents produce a voltage (V_{temp}) across the R-C network which becomes proportional to the actual junction temperature. To the simulator, V_{temp} is simply another voltage which can be used to effect the overall transistor characteristics.

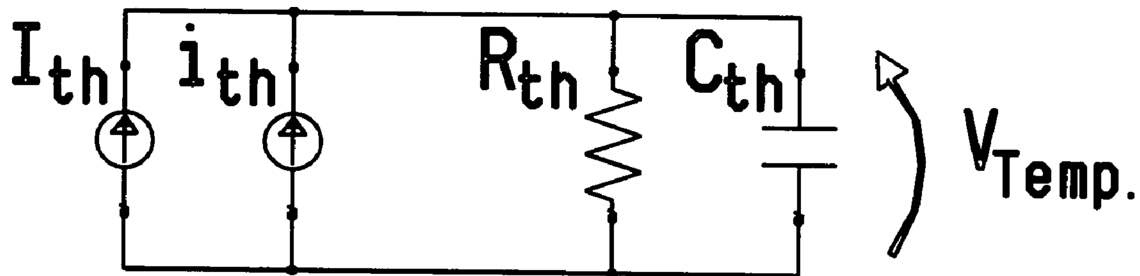

Figure 3-19. Thermal circuit used within the large signal model to emulate the transient change in junction temperature.

This thermal circuit has been added to the large signal model described previously. The base-emitter and current gain elements of the large signal model have been modified to vary dynamically according to the transient temperature, V_{temp}. The

model decreases V_{be} linearly with temperature following the slope of Figure 3-2, and decreases the current gain linearly according to the slope in Figure 3-15. The unique elements of this model are listed in Table 3-1. Not listed in this table are the circuit capacitance terms which are simple lumped elements. The diodes in the model also have capacitance which is modeled as the complete diffusion and depletion capacitance as implemented in SPICE [78].

3.2.3 Model Implementation

This model, implemented in the harmonic balance simulator, LIBRA, consists of a subroutine written in C, which calculates branch currents and charges, based on a set of node voltages. These calculations include the nonlinear emitter and collector diode characteristics, the nonlinear gain, and temperature dependencies shown in Table 3-1. This subroutine also calculates the derivatives of each current and charge with respect to each node voltage as required by LIBRA [79]. The total circuit, including the temperature sub-circuit, consists of eight nodes, requiring the calculation of eight currents and charges. The derivatives of each of these with respect to all their dependent nodes, results in the calculation of 38 conductances and 38 capacitances. A simulation run consists of a series of iterations in which LIBRA calculates the node voltages based on the model's currents, charges and derivatives. The flow chart in Figure 3-20 shows the sequence of operations performed within the user defined model. The C code for this user-defined model is listed in Appendix A.1. In addition Appendix A.2 - A.4 contains example calls to this model for dc, pulsed and microwave power simulations.

Base-Emitter	
$V_{be}' = V_{be} - (K_{vbe} V_{temp})$ $I_{be} = I_{se}\left[e^{\left(\frac{V_{be}'}{n_e V_T}\right)} - 1\right] + I_{ses}\left[e^{\left(\frac{V_{be}'}{n_{es} V_T}\right)} - 1\right]$ $\tau_b = \tau_0 + \tau_1 e^{-K_\tau I_{be}}$ $I_b = I_{be} + I_{bc} + I_{bcx}$	V_{be}' = due to thermal effects V_{be} = with no thermal effects V_T = kT/q K_{vbe} = a constant V_{temp} = junction temperature I_{be} = base diode current I_{se} = saturation current n_e = ideality factor I_{ses} = for surface recombination n_{es} = surface recombination ideality factor τ_b = transit time τ_0, τ_1, K_τ = constants I_b = total base current
Base-Collector	
$I_{bc} = I_{sc}\left[e^{\left(\frac{V_{bc}}{n_c V_T}\right)} - 1\right] + I_{scs}\left[e^{\left(\frac{V_{bc}}{n_{cs} V_T}\right)} - 1\right]$ $I_{bcx} = I_{sx}\left[e^{\left(\frac{V_{bc}'}{n_x V_T}\right)} - 1\right]$ $I_c = I_{ce} - I_{bc} - I_{bcx}$	I_{bc} = intrinsic diode current V_{bc} = intrinsic V_{bc} I_{sc} = saturation current n_c = ideality factor I_{scs} = for surface recombination n_{cs} = surface recombination ideality factor I_{bcx} = extrinsic diode current n_x = extrinsic ideality factor V_{bc}' = extrinsic V_{bc} I_c = total collector current
Collector-Emitter	**Thermal Circuit**
$\beta_f = \beta_0 + a_2 I_{be} e^{(-a_3 I_{be})} + a_4 I_{be}^2 e^{(-a_5 I_{be})}$ $\beta_0 = a_1 - (K_b V_{temp})$ $\quad I_{ce} = \beta_f I_{be} - \beta_r I_{bc}$	$i_{th} = \lvert I_b V_{be}'' \rvert + \lvert I_c V_{ce}'' \rvert$ $I_{th} = \frac{T_0}{R_{th}}$
β_f, β_r = forward, reverse current gain a_1, a_2, a_3, a_4, a_5, K_b = constants V_{temp} = junction temperature I_{be} = base diode current	i_{th} = proportional to power I_{th} = simulates ambient T_0 = ambient temperature R_{th} = thermal resistance V_{be}'', V_{ce}'' = terminal voltages

Table 3-1. Formulas used in large signal temperature-dependent modeling.

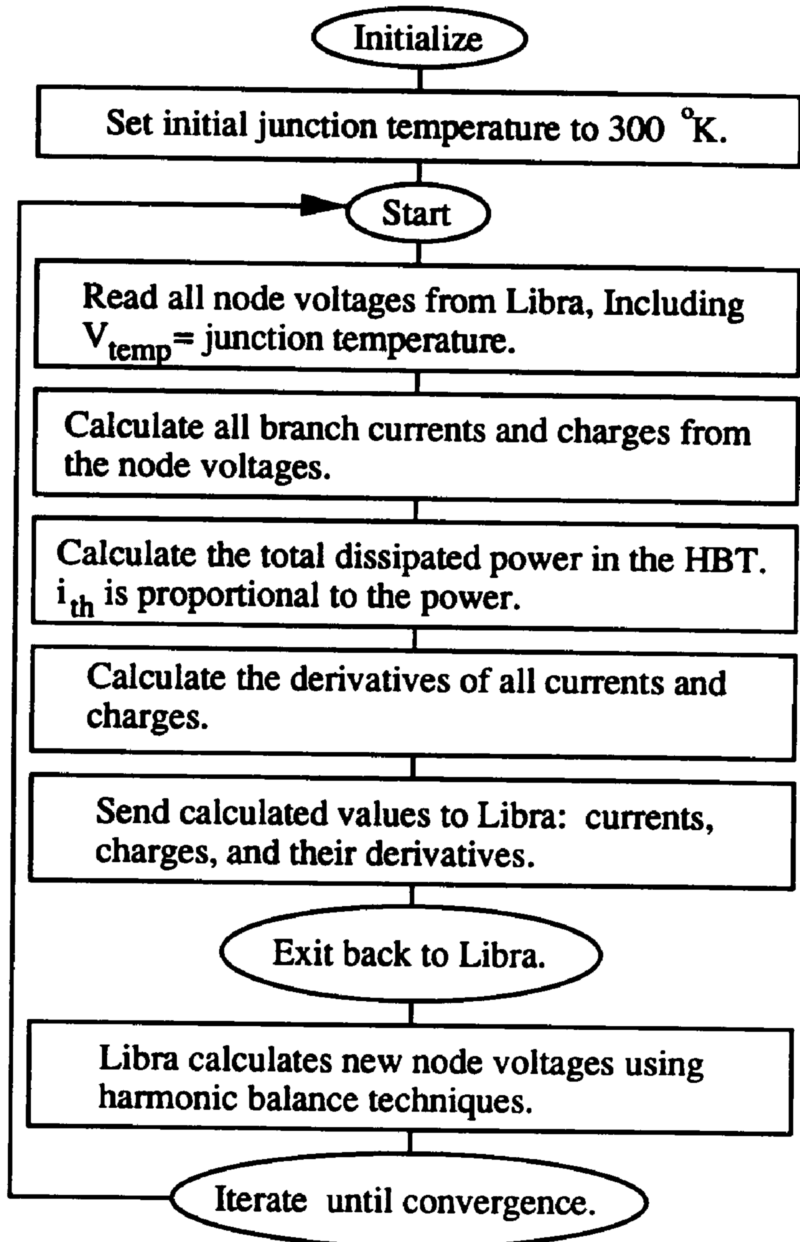

Figure 3-20. Sequence of operations performed during large signal simulations.

3.3 RESULTS AND DISCUSSION

The pulsed waveform results of the large signal model are shown in Figure 3-21. They agree with the corresponding measurements of Figure 3-22, but show a slightly less

dynamic behavior for I_c. This indicates that the model thermal parameters do not quite create the correct balance between the gain reduction and the base current increase. Since the junction temperature is calculated by this model at every current or voltage increment, its waveform versus time can be obtained as seen in Figure 3-23, Figure 4-11 for this simulation. As observed in Section 3.1.2, at the beginning of the pulse the device is at room temperature, and the gain is high. As the device heats up, the base-emitter and gain thermal effects act simultaneously, namely, the gain decreases and the base current increases. These two effects tend to compensate each other when observing the resultant I_c. With an I_b pulse instead of a V_{be} pulse, the model shows that the initial I_c spike is much more severe because there is no compensation of the base-emitter and gain thermal effects. Constant I_b pulses are extremely difficult to achieve in practice, therefore measurements of this type have not been performed.

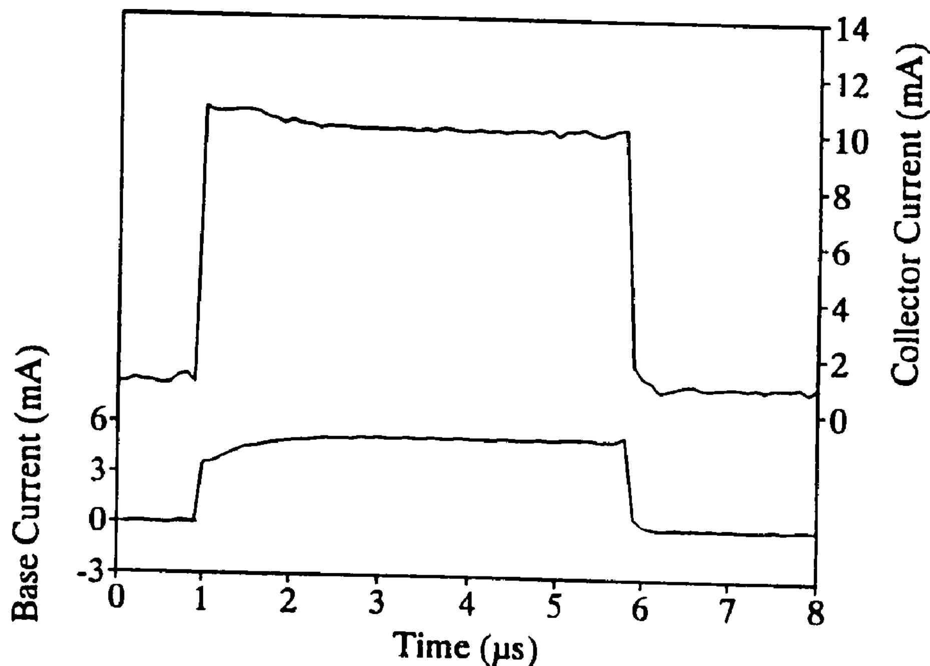

Figure 3-21. Modeled HBT pulsed characteristics.

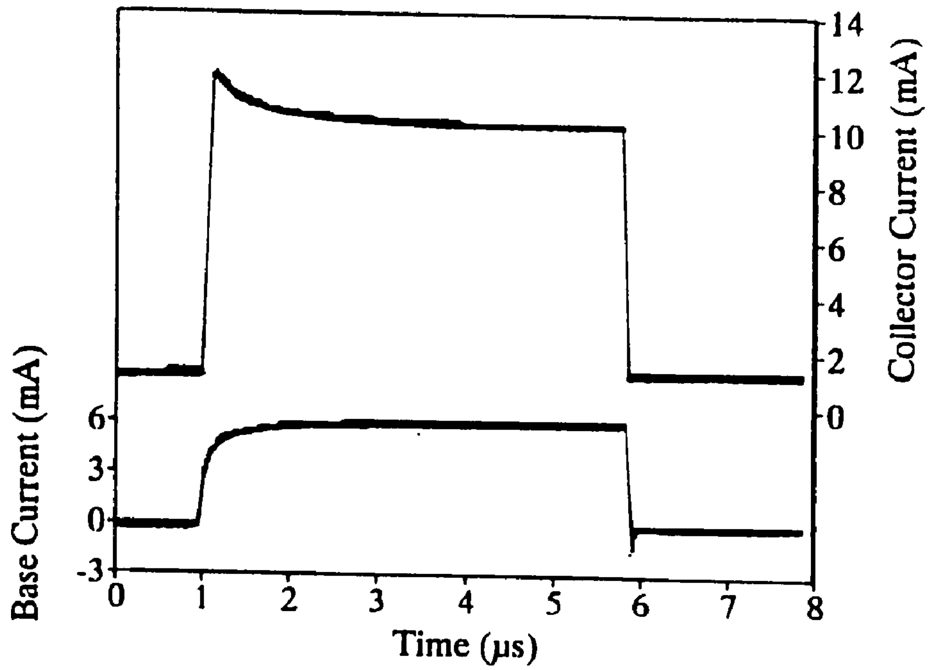

Figure 3-22. Measured HBT pulsed characteristics.

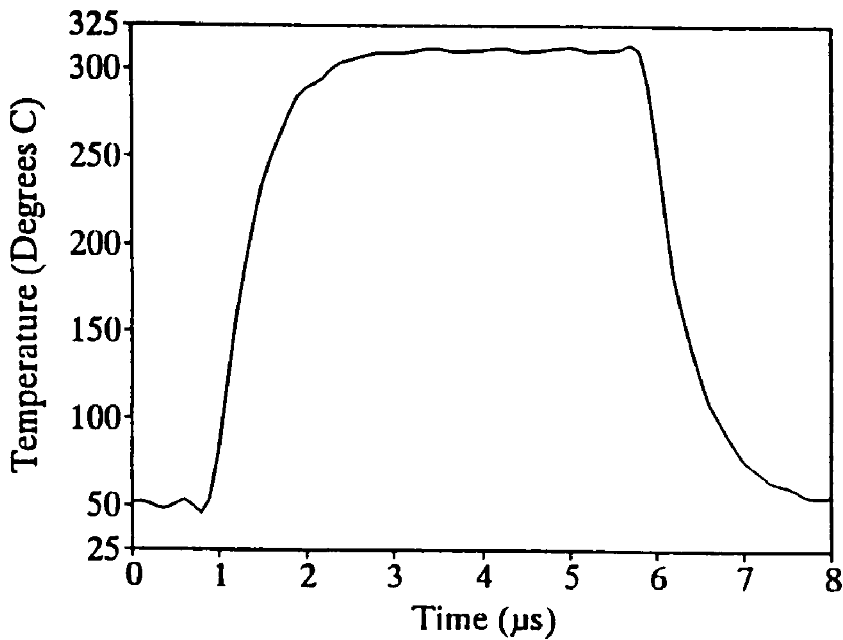

Figure 3-23. Junction temperature waveform during the pulsed simulation.

Figure 3-24 shows the agreement between the modeled and measured dc collector characteristics. The top dashed curve is the model prediction without including thermal effects. This is also shown in Figure 3-25 where it can be seen to agree well with the measured pulsed collector characteristics for this device.

This model has also been used to simulate microwave CW operation. Because of the long thermal time constant, the simulated junction temperature is a steady state value, and the model adjusts the I-V relationship accordingly. The model, however, has not been confirmed against high ambient temperature microwave measurements.

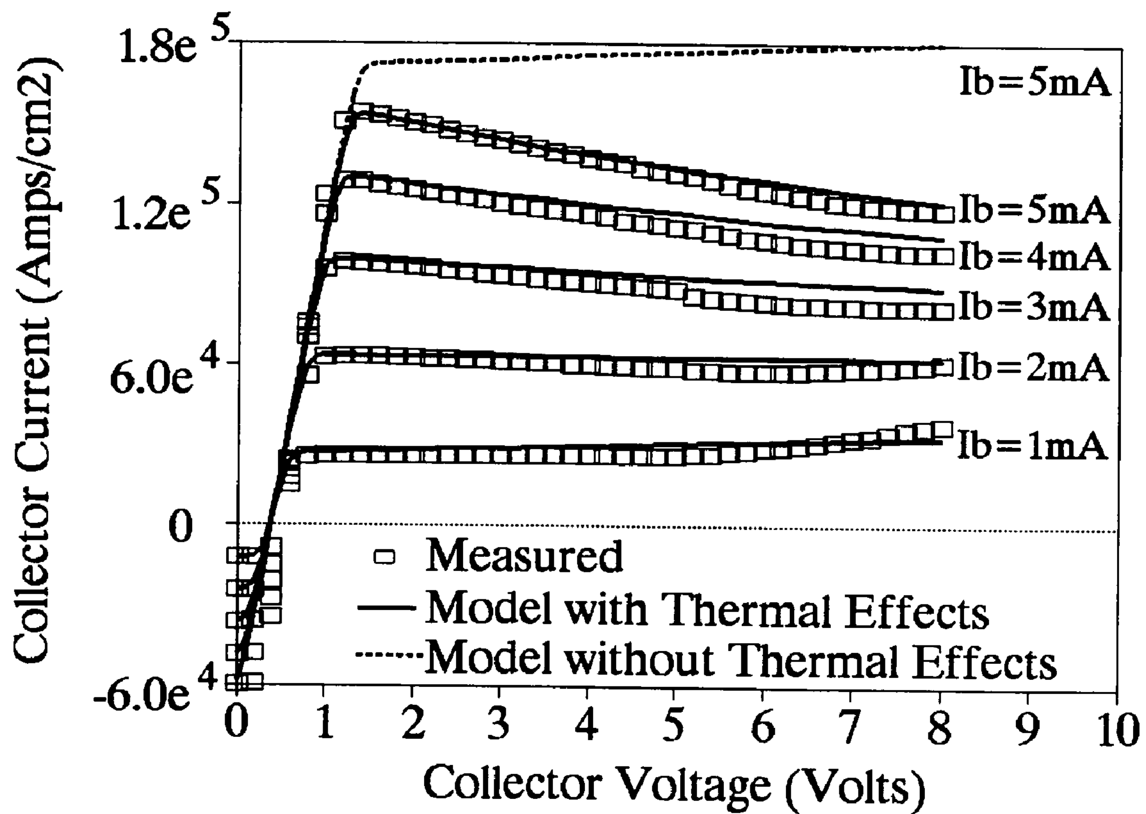

Figure 3-24. Comparison of large signal model simulation with dc characteristics.

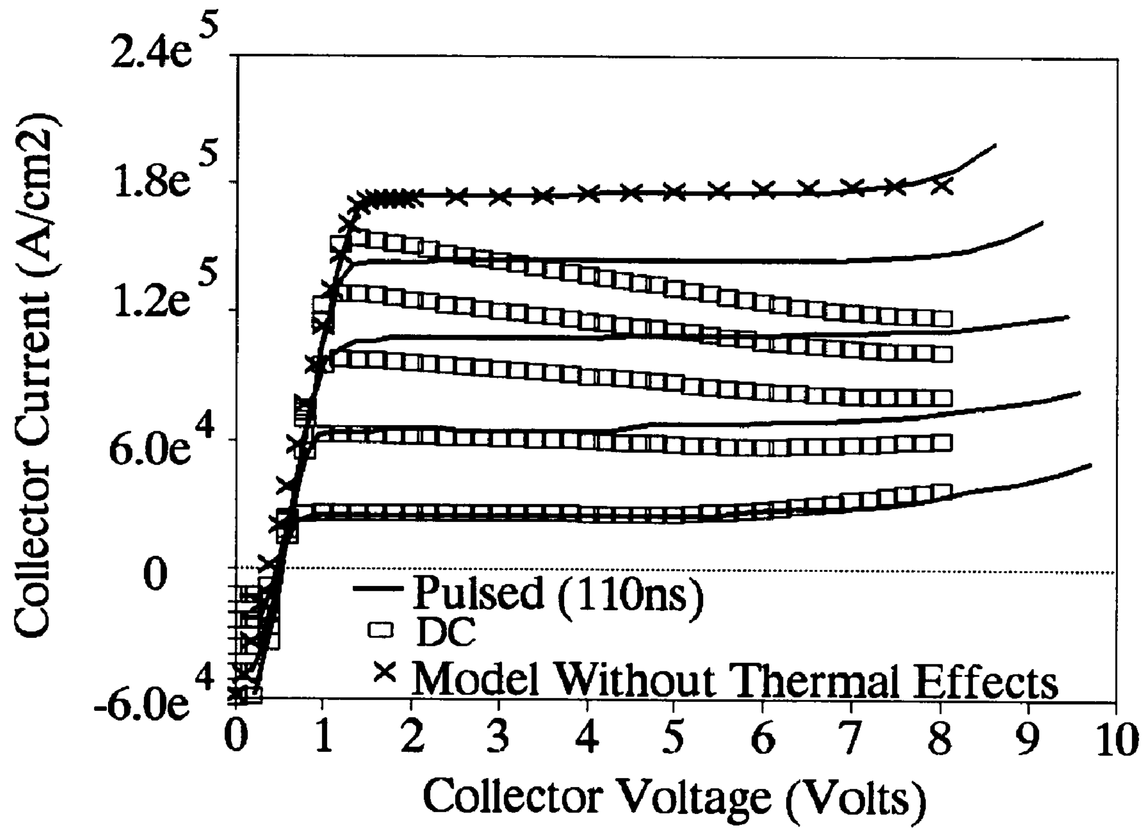

Figure 3-25. Comparison of large signal model simulation with pulsed characteristics.

Chapter 4
HBT THERMAL EFFECTS ON MICROWAVE PERFORMANCE

Simulation efforts for the HBT in the past have successfully treated many aspects of small signal [80-85] and large signal [72,86-91] analysis. Temperature effects have been incorporated for several of the large signal analyses, where all temperature dependencies have been based solely on dc characteristics. Some models have simulated pulsed characteristics were the temperature changes with time [74], while others demonstrate the thermal effects by simulating only dc characteristics [45,92-96].

Any useful temperature-dependent model for the HBT must be able to simulate microwave characteristics at various temperatures. In order to accurately simulate the change in these characteristics, the microwave temperature-dependencies must be based on, or confirmed with, microwave measurements, not just dc characteristics. This chapter analyzes the small signal microwave characteristics of the HBT under a wide range of temperatures and bias conditions through S-parameter measurements, equivalent circuit modeling, and physical modeling. The goal is to analyze the change in microwave equivalent circuit elements with temperatures and bias to provide a basis for developing a large signal temperature-dependent model.

The measurements described in this chapter were performed on an AlGaAs/GaAs carbon doped HBT. The device had three emitter fingers measuring 1.5μm by 6μm with the material structure shown in Table 4-1.

Layer	Material	Doping ($1/cm_3$)	Thickness(Å)
Emitter Cap	n+ GaAs	$5x10^{18}$ Si	2500
Emitter Cap	n+ $Al_{0.25}Ga_{0.75}As$	$2x10^{18}$ Si	50
Emitter	**n** $Al_{0.25}Ga_{0.75}As$	$5x10^{17}$ Si	950
Base	p++ GaAs	$4x10^{19}$ C	1000
Collector	**n-** GaAs	$4x10^{16}$ Si	4000
Sub-Collector	n+ GaAs	$5x10^{18}$ Si	5000
Isolation Spacer	si AlAs	$< 5x10^{15}$	1000
Buffer	si GaAs	$< 3x10^{14}$	1000
Substrate	si GaAs	$< 3x10^{14}$	625 μm

Table 4-1. Material thickness and doping structure.

4.1 EXPERIMENTAL

To investigate the variation of microwave parameters with temperature, a variable-temperature measurement system was constructed. With this system, S-parameter measurements were performed on a device at temperatures varying from room temperature to 226°C. The measurement system, shown in Figure 4-1, consists of an HP8510B network analyzer to perform the S-parameter measurements, an HP4142B to supply the variable dc bias, Gore-Tex flexible cable, Tektronix coplanar on-wafer probes and, a West-Bond hot chuck.

The chip containing the test device was bonded to a TO-3 package by high-conductivity silver epoxy ($\sigma \approx 1x10^4/\Omega cm$). Heat sink compound was applied to the back side of the TO-3 package and then bolted to the hot chuck. A simple heat-shield was attached to the probes to reduce probe-body heating via convection and radiation from

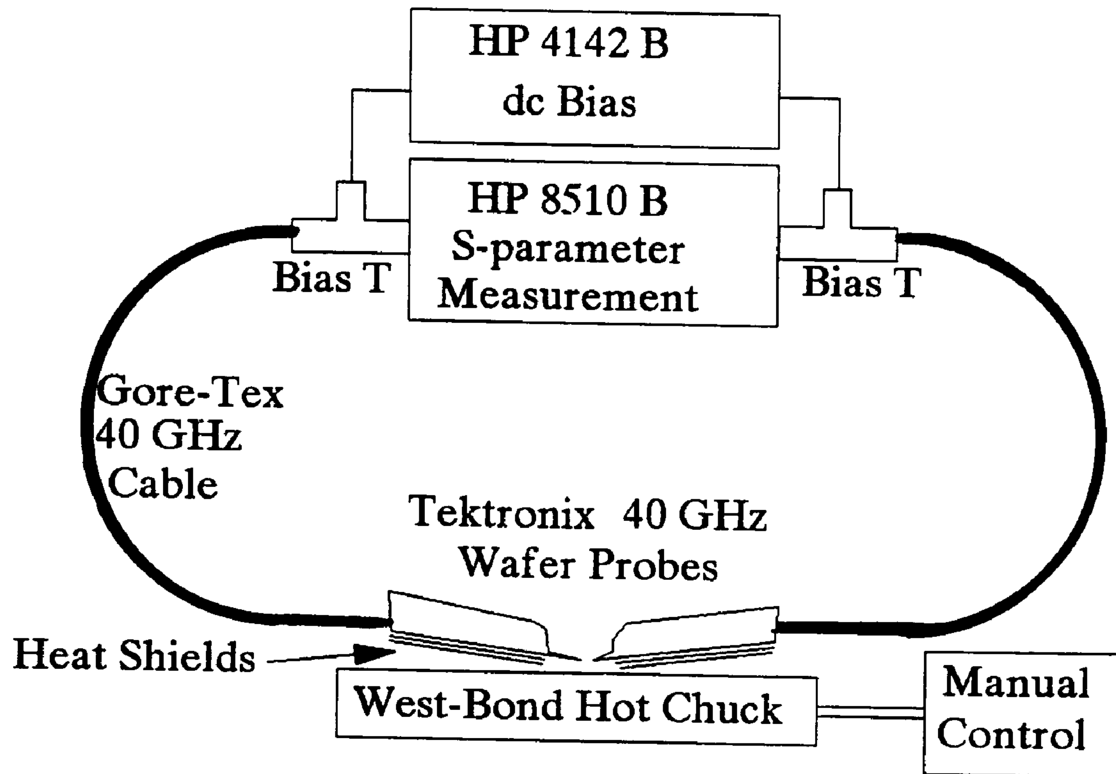

Figure 4-1. Variable temperature S-parameter measurement system.

the hot chuck. Figure 4-2 illustrates the two-fin structure of these heat shields. Even with these heat shields, the probe body, as well as a portion of the Gore cable, heats up during measurements. Tektronix and Gore confirm that these components can withstand temperatures up to 150°C and 75°C respectively, but since the electrical characteristics of these components change with temperature, calibrations must be performed often.

Full two-port on-wafer calibrations were performed before each set of S-parameter measurements at a particular temperature. The short-open-load-thru (SOLT) type calibration was performed using a Tektronix Tek-96 on-wafer calibration substrate. The dc resistance of the 50 Ω load standard was measured and utilized in the calibration at each temperature. This resistance, however, only changed by 0.8 Ω over the 200°C

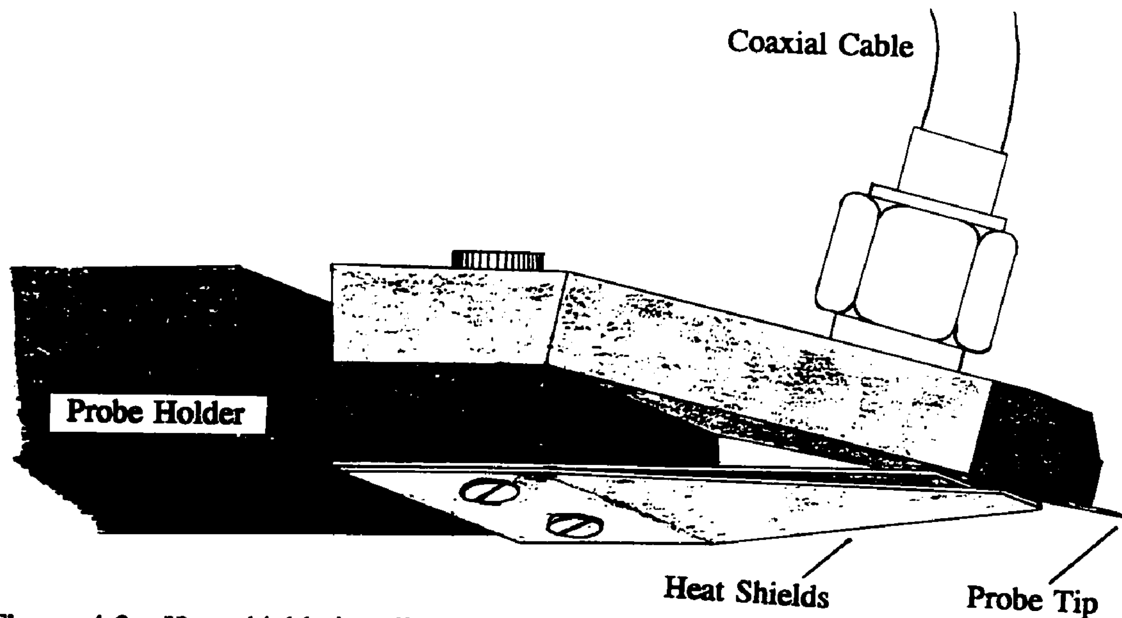

Figure 4-2. Heat shields installed to protect probe-body overheating.

range. The completed calibration corrects for losses and phase delays caused by all components from the tip of the probes to the measurement point within the network analyzer [97,98].

To measure the actual ambient temperature presented to the device under test, the diode characteristics of a neighboring HBT were monitored. The base and emitter of this HBT were wire-bonded to leads, and while applying a small constant base current, the base-emitter voltage(V_{be}) was measured periodically during the entire testing sequence. Since the diode characteristics are very sensitive to temperature, the actual wafer temperature can be easily calculated. The V_{be} characteristics of this device were calibrated using several fixed ambients inside an oven, and Figure 4-3 shows these linear V_{be} characteristics versus temperature.

For the particular series of S-parameter measurements to be described, a wide

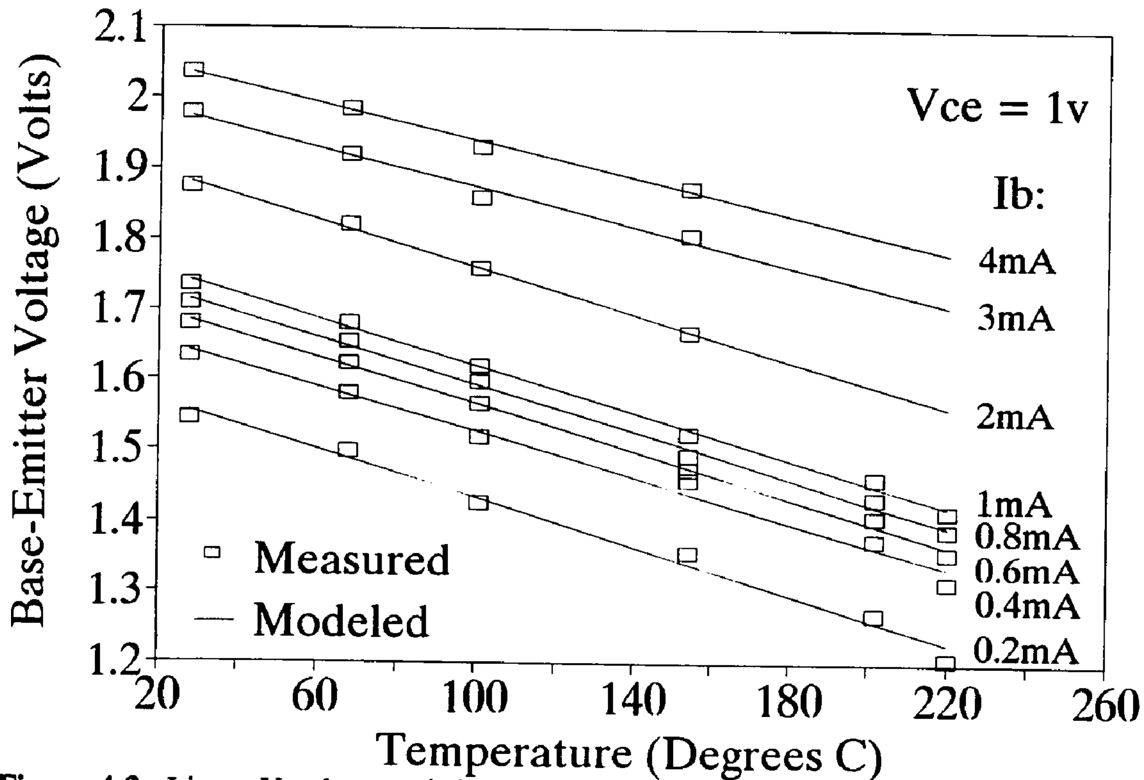

Figure 4-3. Linear V_{be} characteristics used for calibration of wafer ambient temperature.

range of temperatures and bias conditions were implemented. The ambient wafer temperatures were calculated to be 23, 84, 123, 171, and 226°C. This covers the typical range of junction temperatures encountered during normal device operation. Actual junction temperature is evaluated later using thermal resistance and dissipated power. At each of the five temperatures, S-parameter measurements were taken at 28 bias points as shown in Figure 4-4. These bias points cover many regions of operation including forward active, saturation, cutoff, negative I_c, and the I_c=0 point. This range of bias values was chosen to enable the full characterization of the major physical mechanisms which contribute to the HBT characteristics.

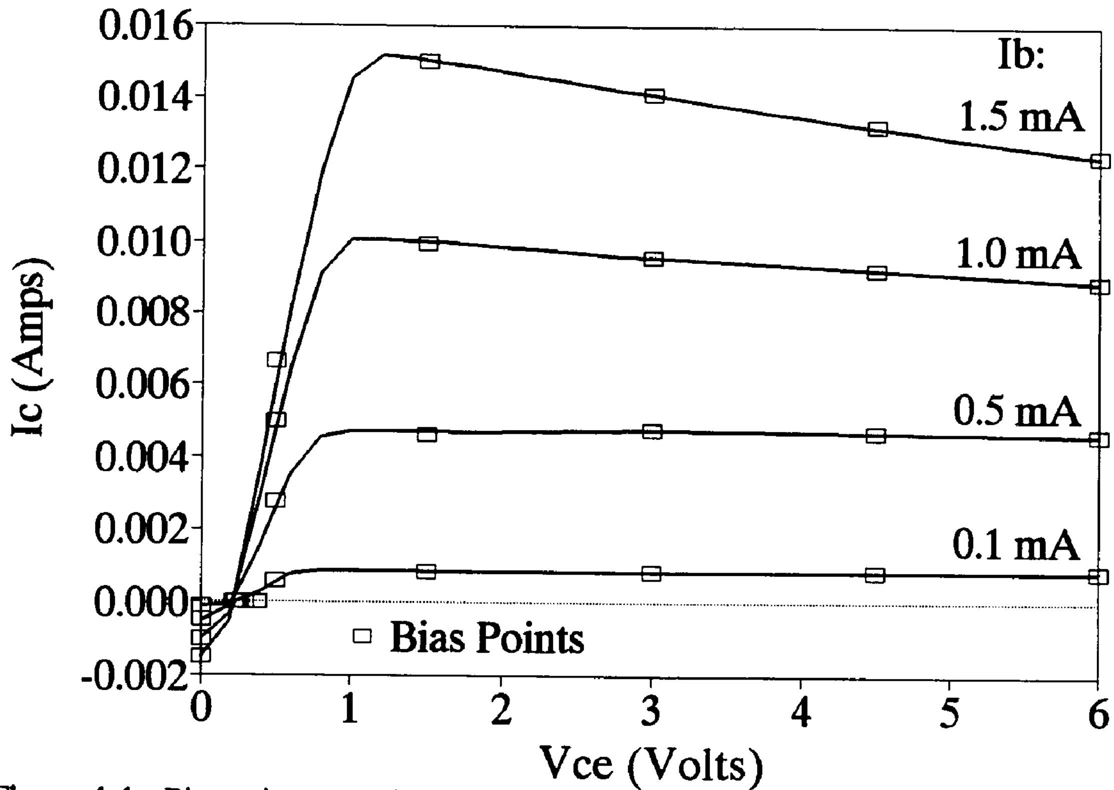

Figure 4-4. Bias points used for elevated temperature S-parameter measurements.

4.2 THEORY AND ANALYSIS

Before developing a large signal model, it is necessary to establish the dynamic behavior of various device elements with bias and temperature. The technique used in this work was to measure and model the microwave characteristics at many bias points and many temperatures. Microwave parameters were extracted for a simple equivalent circuit from the measured S-parameter data. To aid in the interpretation of these element values with bias and temperature, a physical model based on material parameters and geometry was used to calculate theoretical values.

Of course, all parts of the HBT are expected to be affected by temperature, but the base-emitter diode and the current gain are known to have the most significant change

with temperature [74,99]. Therefore, the microwave elements corresponding to these areas are analyzed most extensively.

4.2.1 Bias- and Temperature-Dependent Equivalent Circuit

The microwave equivalent circuit used for this temperature investigation is the simple Pi-model shown in Figure 4-5. This equivalent circuit, which treats all areas of the HBT with lumped elements, was found to match the HBT characteristics up to 10 GHz in all bias conditions. R_{eb} and C_{eb} model the base-emitter diode, R_{cb} and C_{cb} model the base-collector diode, g_m is the transconductance, and R_{ec} is the output resistance. R_b, R_c, and R_e are parasitic contact and bulk resistances, and C_{ec} is the emitter-collector metalization crossover capacitance.

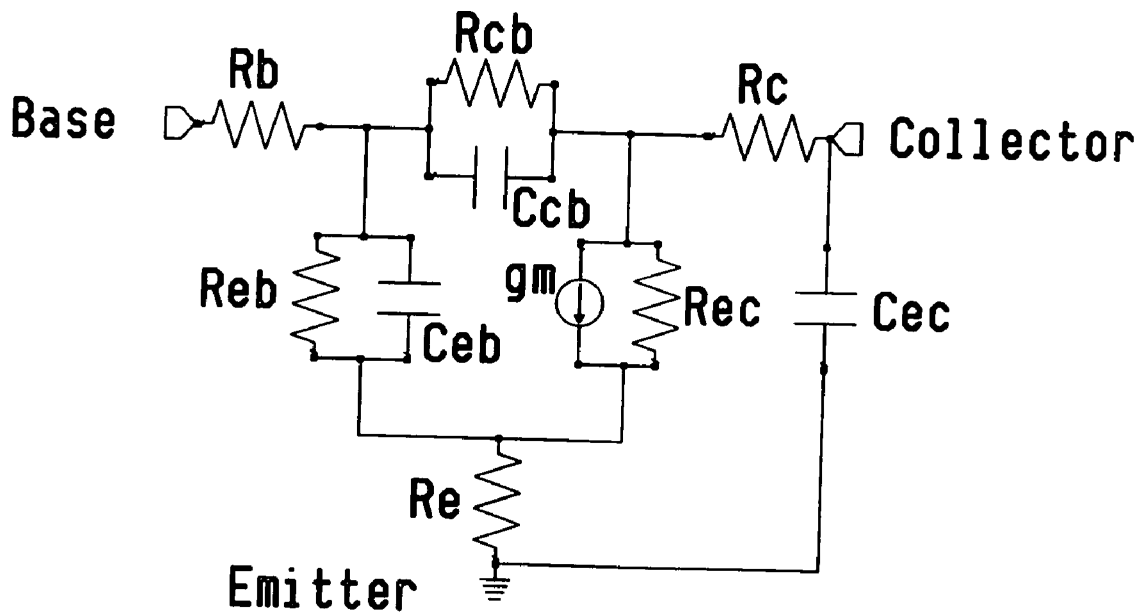

Figure 4-5. Microwave equivalent circuit used for bias- and temperature-dependent parameter extraction.

At each bias point, for each temperature, a unique set of equivalent circuit element values were extracted. Initial element values were calculated by using a one-dimensional physical model based on material properties and dc measurements. This model is described in the next section. From these initial values, the circuit simulator LIBRA [73], was used to optimize all element values to fit the measured S-parameter data. Element values determined from this equivalent circuit are termed 'measured' throughout this chapter but are actually *extracted values* from measured S-parameters.

4.2.2 One-Dimensional Physical Model

The one-dimensional physical model used for this work is based on the theory presented in Section 2.2. Basically, the terminal currents are calculated from first principles using device dimensions, material properties, junction temperature, and applied voltages. The temperature dependence of many of the material properties for both GaAs and AlGaAs were included in this physical modeling. These include the bandgap, Eg, the intrinsic carrier concentration n_i, the saturation velocity, v_{sat}, the emitter electron mobility, μ_{ne}, the base hole mobility, μ_{pb}, and the collector electron mobility, μ_{nc}. The actual calculations are performed in a spreadsheet which provides ready assess to all calculations of material parameters and flexibility to add additional analyzes without full recalculation. The capability for including self-heating and constant current boundary conditions are implemented using the spreadsheet to solve the interdependencies.

In the model there is room for a limited amount of fitting by changing the surface and bulk recombination velocity and lifetime for the model since these values are very

process dependent and difficult to predict theoretically. In addition, the parasitic resistances (R_b, R_c, and R_e) which are used for the model calculations are measured values from dc analyses. These resistances did deviate from attempted model predictions probably due to misalignment and over-etching during processing.

Several standard assumptions have been made for the model calculations. First, all material is assumed to have uniform doping and composition with abrupt junctions. This assumption is quite accurate, since the device was designed to be uniform and abrupt by using MBE growth. The commonly used depletion approximation and quasi-neutrality were also assumed [23].

As described in Section 2.2, Maxwell-Boltzmann statistics [25] were applied assuming a linear gradient of holes in the quasi-neutral base, resulting in the Shockley equation [15] for the emitter-collector transport current. This current is a function of the internal V_{be} which does not include the base and emitter parasitic resistance effects. These effects are included afterwards. High level injection (velocity saturation) [100,101], the Kirk effect (base push-out) [102,103], and Shockley-Read-Hall (SRH) recombination [23] in the base were also included in this emitter-collector current. For the base-emitter current, which is also a function of the internal V_{be}, SRH bulk recombination and reverse hole injection were included, both having an $e^{(Vbe/kT)}$ dependence. Also included was surface and depletion region recombination, both with an $e^{(Vbe/2kT)}$ dependence. In addition, the model includes the base-collector diode transport current which is a function of the internal V_{cb} and temperature.

Once the terminal currents are calculated from internal voltages, the actual *terminal* voltages are evaluated accounting for the parasitic R_c, R_b and R_e. As a second order effect, the external pad to pad leakage resistance was included ($R \approx 500$ MΩ). This strictly measured quantity effects only the low V_{be} characteristics, and is probably due to substrate and surface leakage.

Device self-heating is included by using a measured thermal resistance which is assumed to remain constant with temperature. The junction temperature is used for all calculations of material properties and transport equations, iterating until the equations are self-consistent.

Several microwave parameters are calculated from two sets of I-V characteristics with slightly offset V_{be}. As in Section 2.2.4 the small signal base-emitter resistance is given by

$$R_{eb} = \frac{\Delta V_{be}}{\Delta I_b} \tag{4-1}$$

For a constant V_{be}, I_b will increase exponentially with temperature (T). Therefore for a given change in V_{be}, the change in I_b will increase causing R_{eb} to decrease exponentially with T. The transconductance is

$$g_m = \frac{\Delta I_c}{\Delta V_{be}} \tag{4-2}$$

and for similar reasons will increase exponentially with T. C_{eb} is given by the slightly more involved expression:

$$C_{eb} = C_{je} + g_m \tau_b \tag{4-3}$$

and was shown to increase with T.

4.3 RESULTS AND DISCUSSION

Both the dc I-V characteristics and the microwave element values have been calculated using the physical model for all measured temperatures and bias points. A comparison of I-V characteristics confirms the validity of the model and indicates the magnitude of possible error. A comparison of calculated and measured microwave elements confirms the accuracy of the equivalent circuit extraction and the degree to which the bias- and temperature-dependence of these elements agrees with device physics predictions.

4.3.1 I-V Characteristics

To test the agreement of the physical model to the measured results, first the dc I-V characteristics were compared. Figure 4-6 shows this comparison between the measured and modeled base and collector currents (Gummel plot) for the two extreme temperatures measured, 23°C and 226°C. The slope of I_c in the log-linear region is proportional to $e^{(Vbe/kT)}$, while the slope of I_b is approximately proportional to $e^{(Vbe/2kT)}$. As described in the last section, the 2kT dependence is due to the surface and depletion region recombination current. The surface recombination velocity and bulk recombination lifetime were adjusted to improve the fit for the 23°C curve and were assumed to be temperature independent. At high V_{be}, both I_c and I_b show a saturation

due to the series base and emitter resistances. At low V_{be} a pad to pad resistive leakage dominates over the diode transport current and causes the flattening of the characteristics.

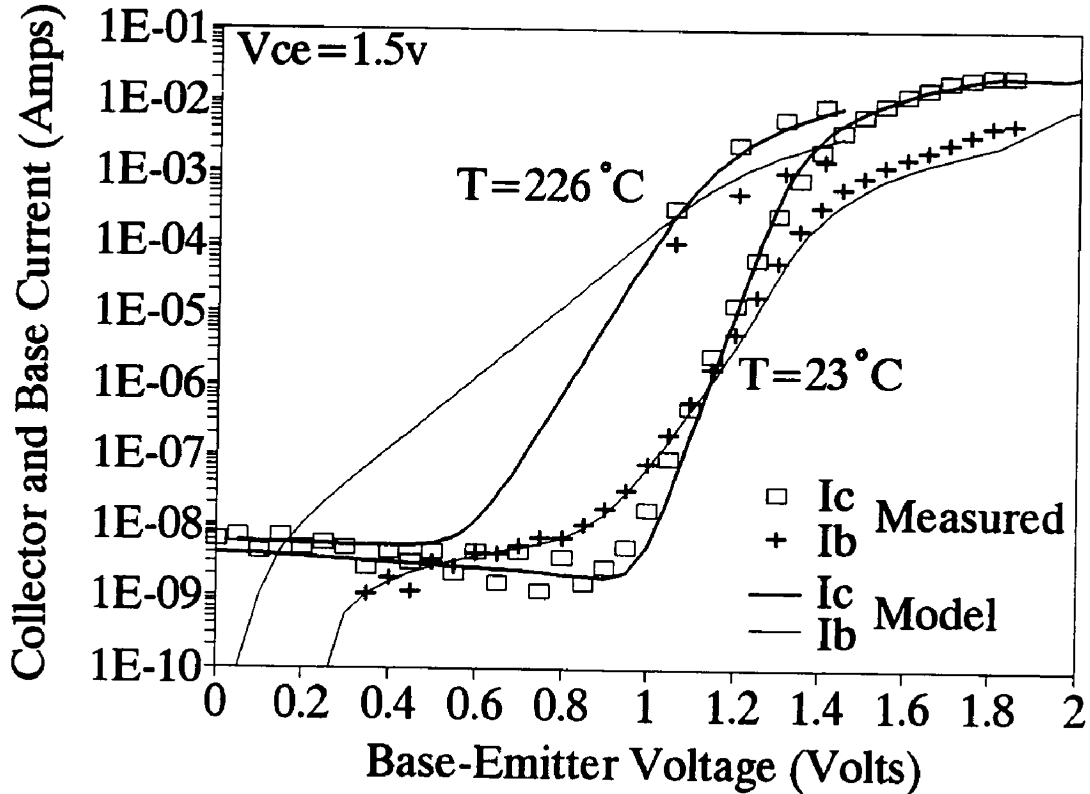

Figure 4-6. Measured and modeled Base and Collector currents for the HBT at two temperatures.

Since the base-collector currents are also accounted for in this model, the collector current characteristics versus collector voltage can be calculated. Figure 4-7 shows a comparison of measured and modeled room temperature collector characteristics. The measured points correspond to bias points for subsequent S-parameter measurements. Figure 4-8 shows the corresponding V_{be} characteristics. Likewise, Figure 4-9 and Figure 4-10 show the collector and corresponding base-emitter characteristics for the 226°C measurements.

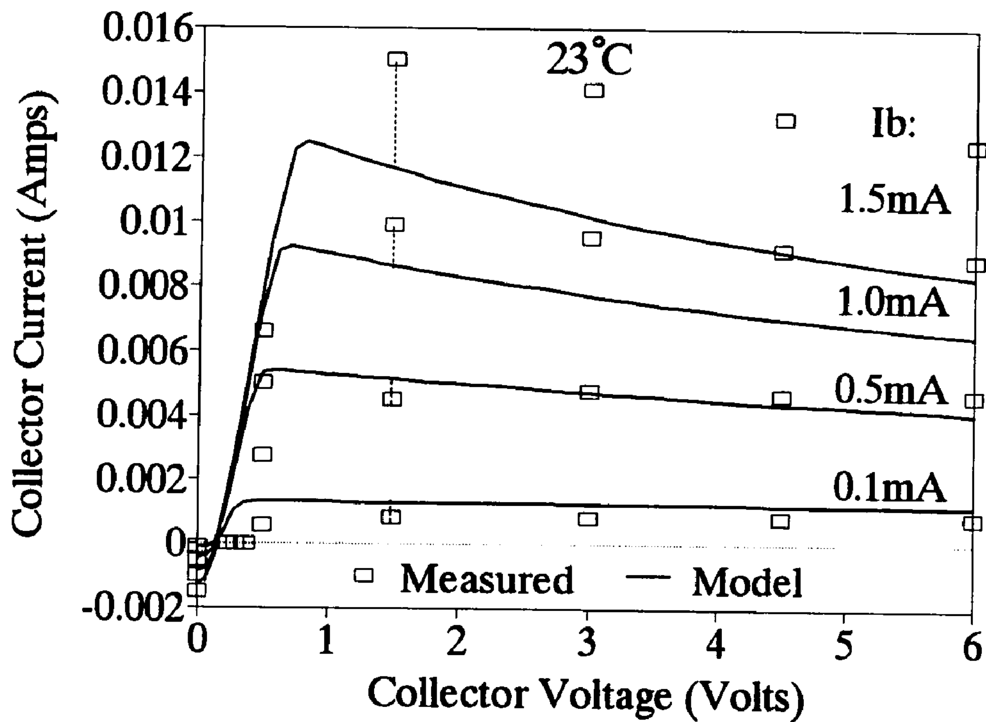

Figure 4-7. Physical Modeling of room temperature collector characteristics.

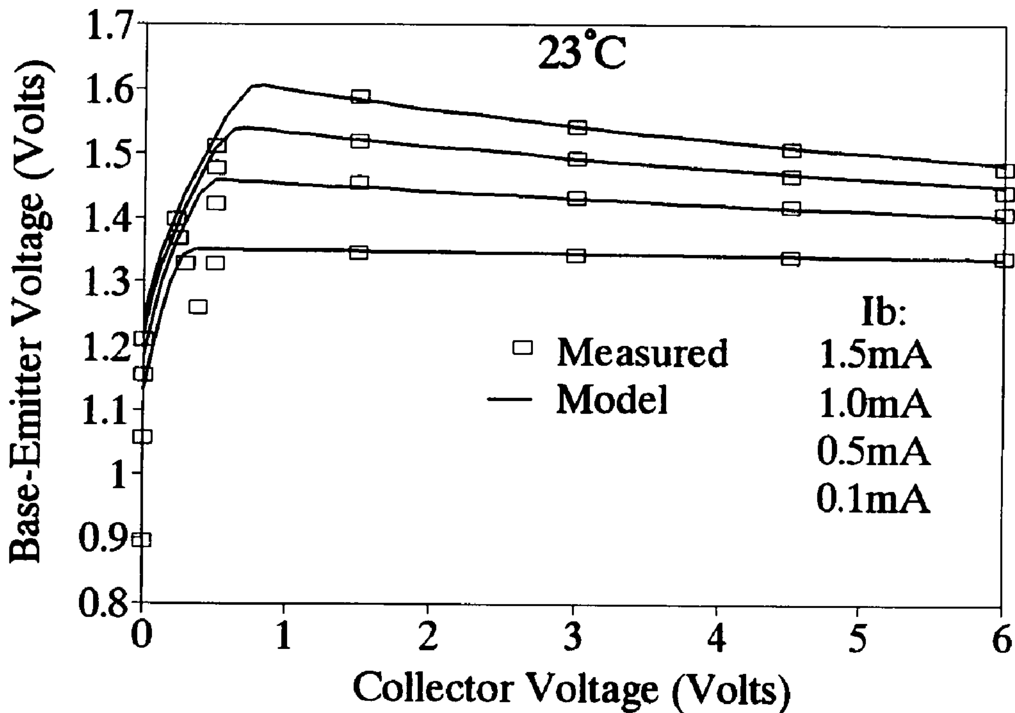

Figure 4-8. Physical modeling of V_{be} associated with characteristics of Figure 4-7.

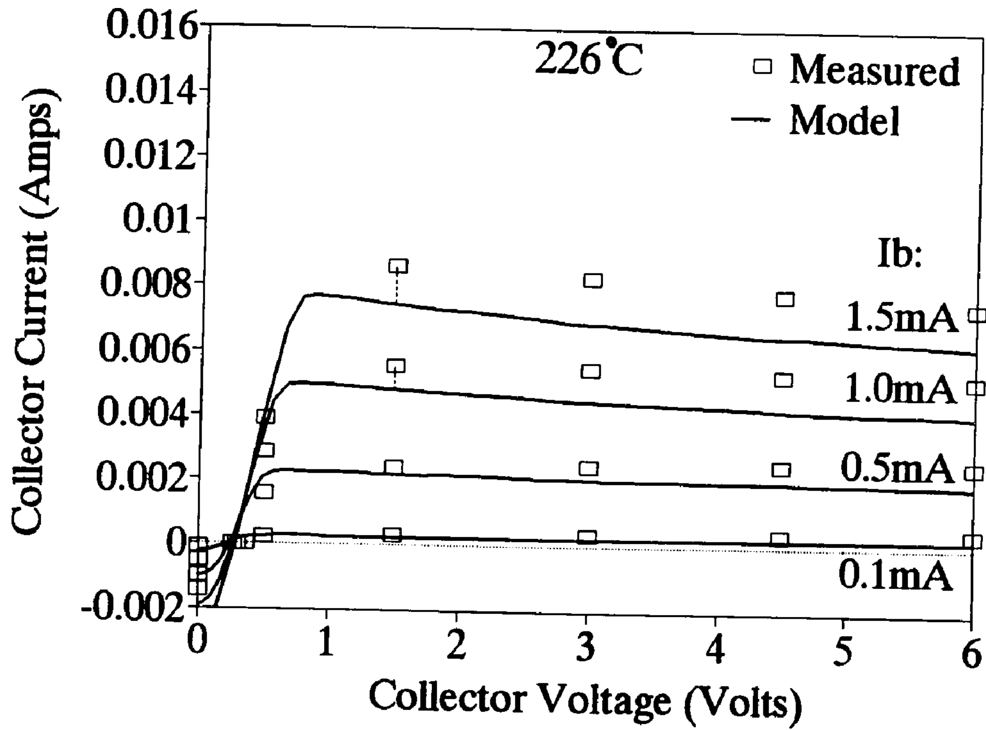

Figure 4-9. Physical modeling of collector characteristics at 226°C.

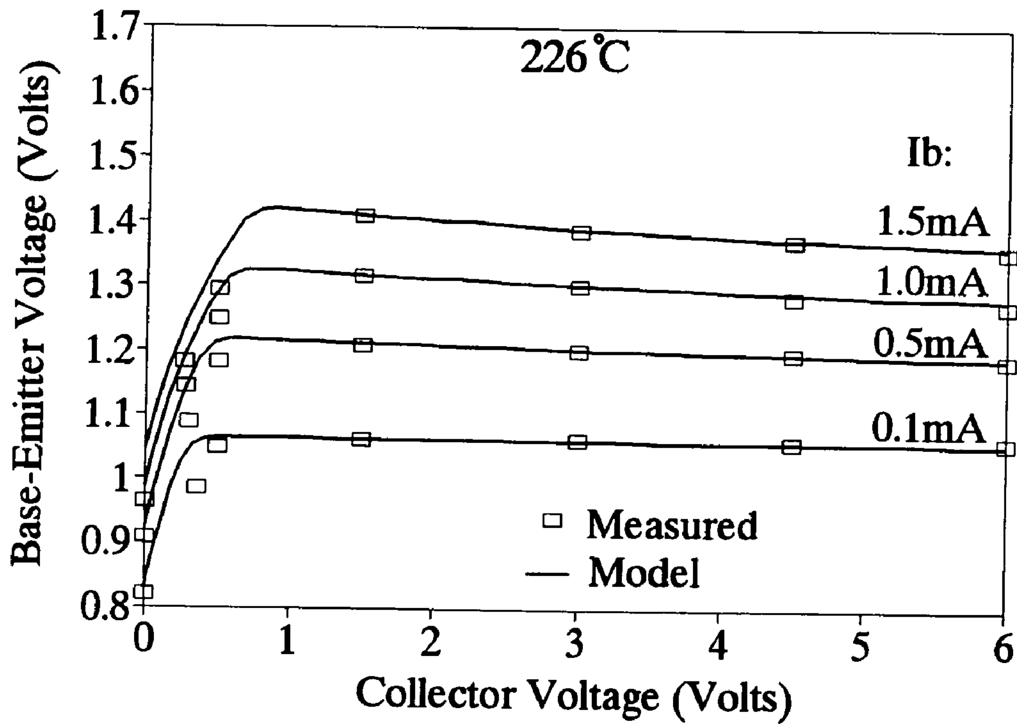

Figure 4-10. Physical modeling of V_{be} associated with characteristics of Figure 4-9.

A constant base current boundary condition is used for each series in these calculations. Since calculating I_b and I_c are based on a given V_{be}, the value of the base current boundary condition is modified to correspond to an actual measured V_{be}. Therefore, for the model calculations, the value of this constant I_b for each series is slightly different than the applied I_b values of the measurements. The I_b values differ by less than a factor of two for all calculations. In this way, the most accurate results can be obtained when considering the error in *both* the base-emitter characteristics and the collector characteristics. Even so, much of the error between modeled and measured appears in the collector characteristics. The error in the magnitudes of I_c is due to the accumulation of errors in input material parameters which is analyzed in detail for the microwave elements to be presented in Section 4.3.2.2.

The model also includes self-heating, accounting for the decrease in I_c and V_{be} with increasing collector voltage seen at all temperatures. Figure 3-23, Figure 4-11 shows the modeled junction temperature corresponding to the calculations in the previous four figures. It can be seen in Figure 4-7 that the slopes of the room temperature collector characteristics are different than those of the measurements. This is due to the fact that the model uses a thermal resistance which is assumed constant with temperature. The thermal resistance value is measured as one average value over the whole temperature range of interest when actually the thermal resistivity increases with temperature [91,104]. The overall result is that the thermal resistivity for the model is high for the room temperature case, causing the model to predict a more dynamic temperature change with power, and causing the collector characteristics to change more

dynamically than the measured result.

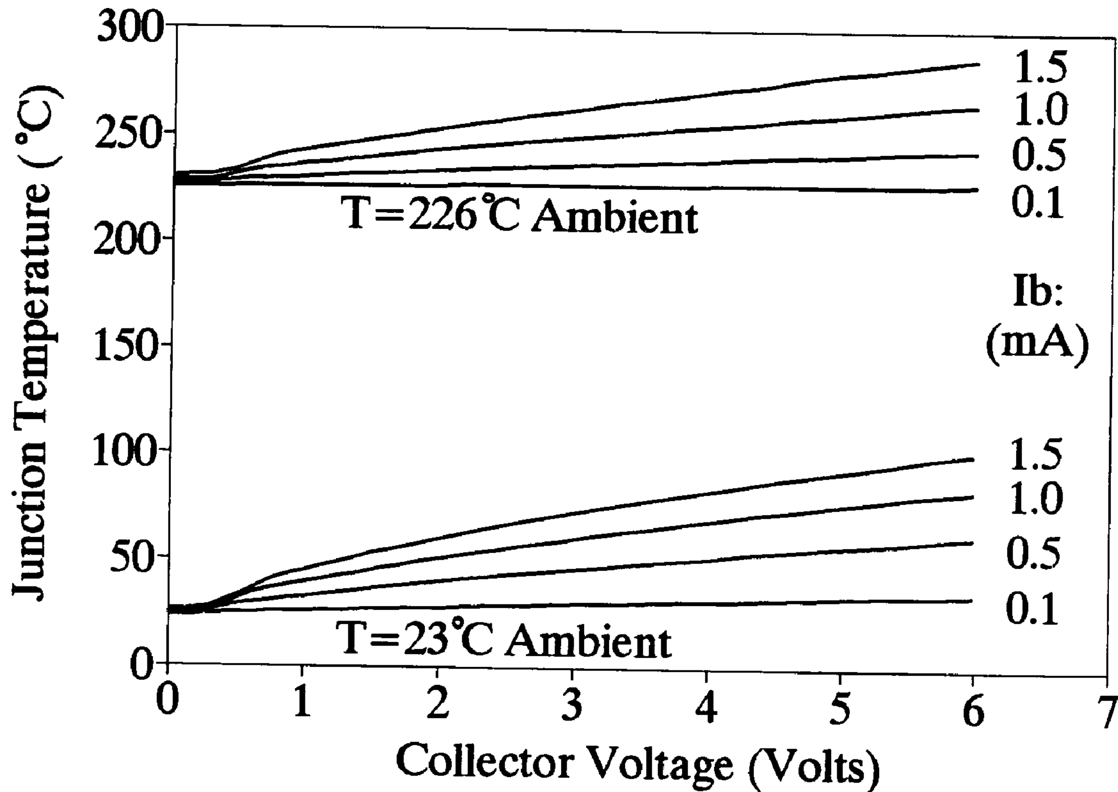

Figure 4-11. Junction temperatures calculated by the physical model for the previous room temperature and 226°C simulations.

4.3.2 Small Signal Analysis

For a complete comparison to the measured element values (derived from the S-parameters), the model was evaluated at all five measurement temperatures. Figure 4-12 shows an enlarged view of the Gummel plot of Figure 4-6. This plot shows the measured and modeled base and collector currents at all measurement temperatures. The model tends to show more I_c saturation than the measured I_c while the opposite is true for I_b. This difference also shows up in the calculations of microwave elements, and is

probably due to the lumped approximation for the parasitic base and emitter resistances.

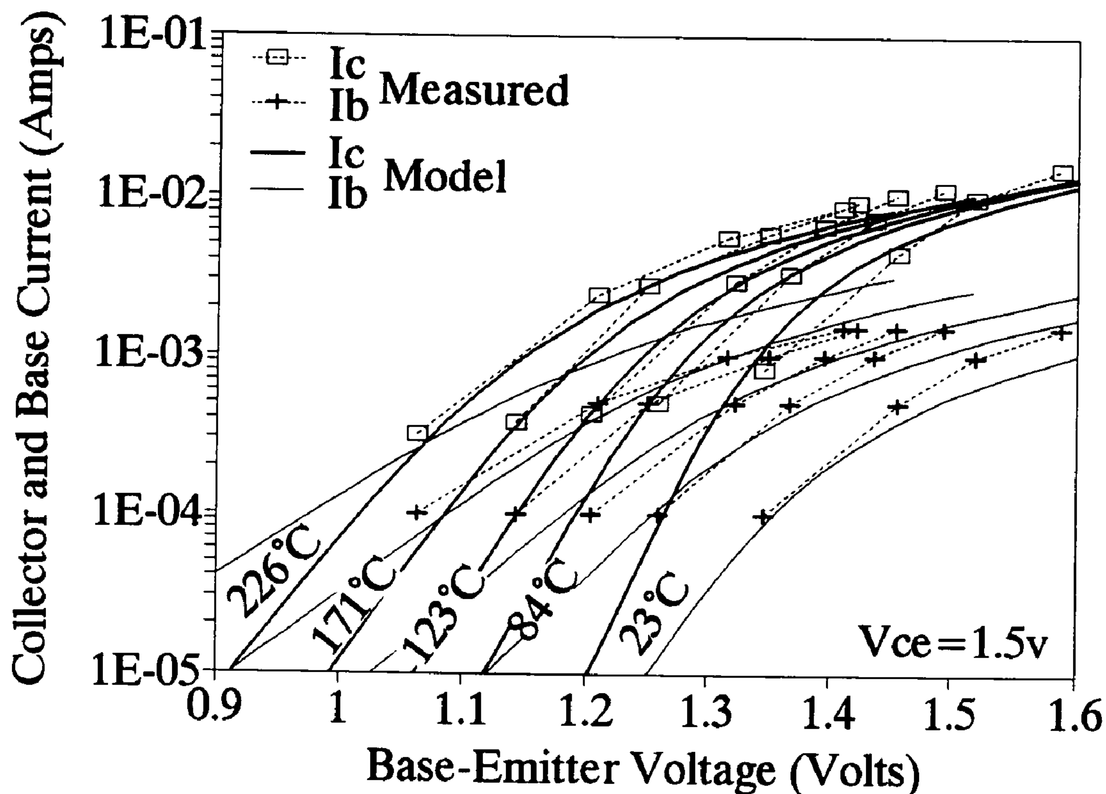

Figure 4-12. Gummel plot including physical model calculations and measurements at all evaluated temperatures.

4.3.2.1 Microwave Circuit Elements

Figure 4-13 shows the temperature dependence of R_{eb} versus V_{be} corresponding to the same bias points in Figure 4-12. As described previously, R_{eb} is expected to decrease with temperature because of the larger change in I_b at high temperatures for a given change in V_{be}. The saturation effect as V_{be} increases is caused by the parasitic R_b, and R_e taking up an increasingly larger portion of the applied external V_{be}. As a result, the actual internal diode V_{be} does not increase as quickly in this region. In the absence of this saturation, R_{eb} decreases by an average of 1.3% per°C indicating the change at

a constant *internal* V_{be}. This change is simply an average since the exact magnitude of change depends on the particular bias region and temperature as seen in the figure.

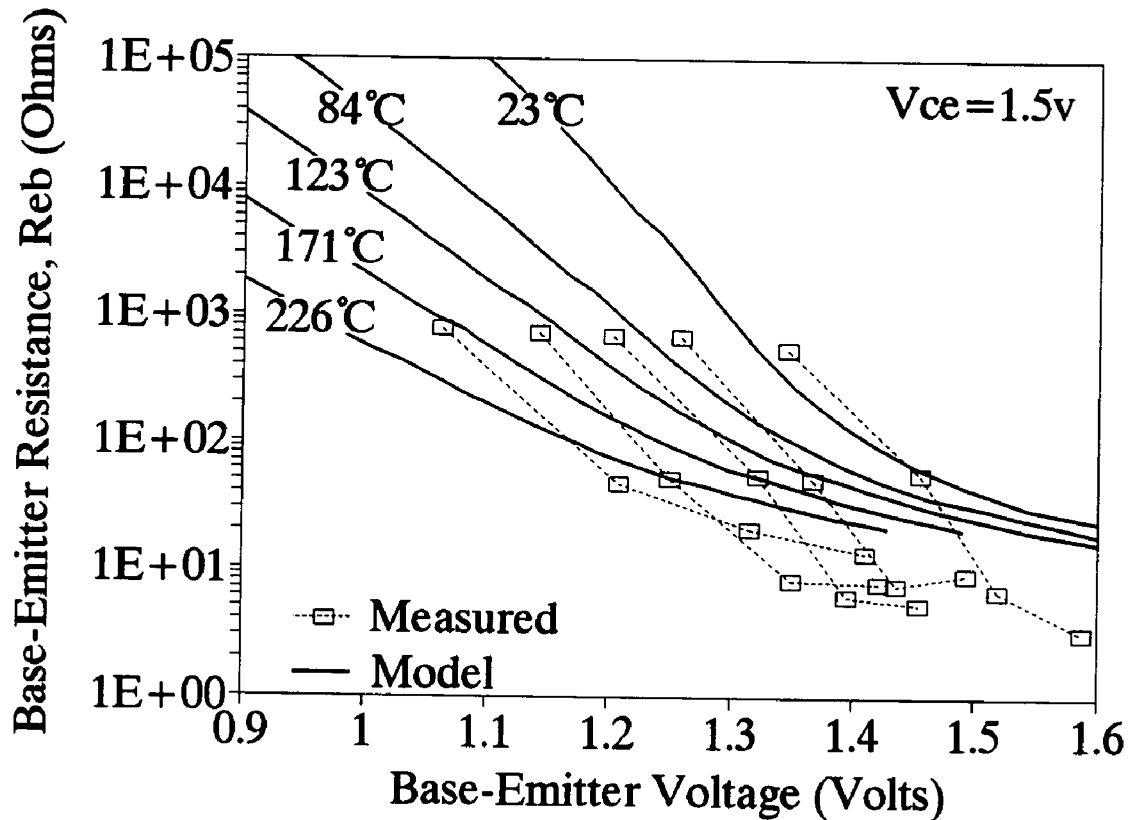

Figure 4-13. Model calculations and measurements of the base-emitter resistance, R_{eb}.

Figure 4-14 shows g_m for the five temperatures and shows the expected increase with temperature for a given V_{be}. Again, in the absence of saturation, g_m increases by an average of 1.4% per°C. Since the current gain is defined as $\beta = R_{eb}g_m$, β will increase slightly with temperature at constant V_{be}. Normally, however, the current gain is analyzed as a function of constant I_b. At constant I_b, V_{be} decreases with temperature as seen in Figure 4-3. The net result, as evidenced by the negative differential resistance

in the I-V plots of Figure 4-7 and Figure 4-9, is that current gain decreases with temperature.

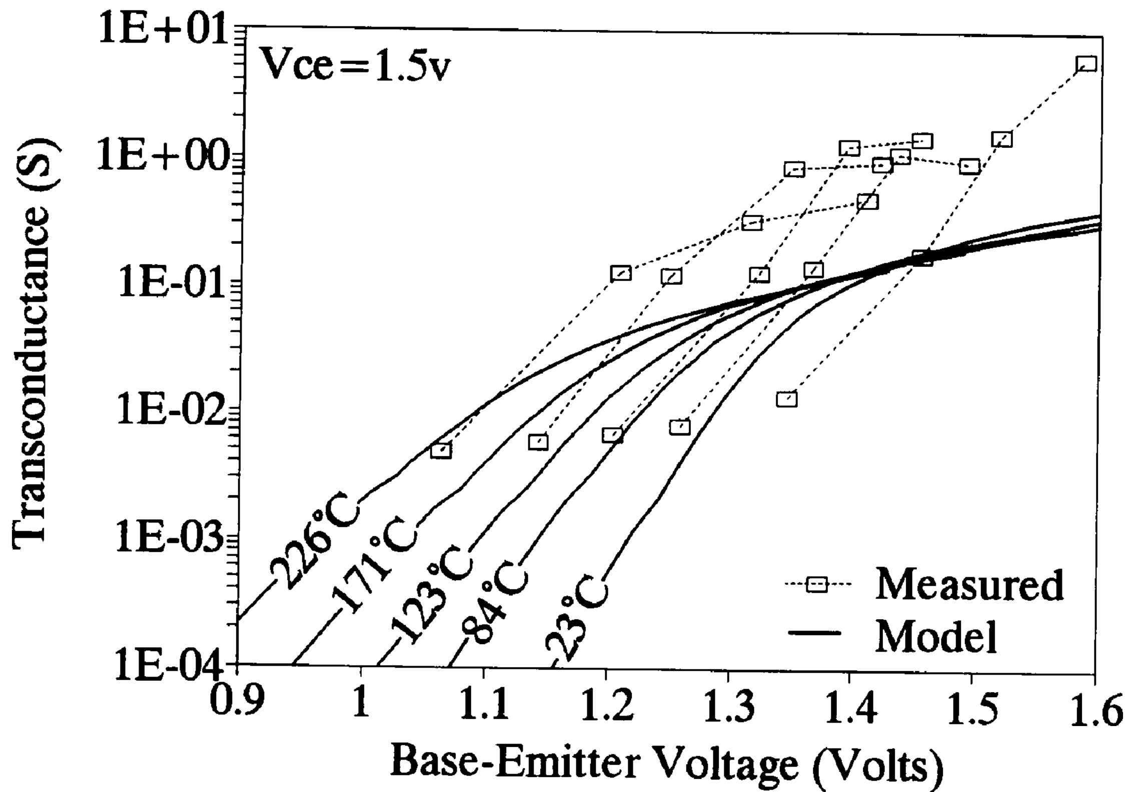

Figure 4-14. Model calculations and measurements of transconductance, g_m.

Figure 4-15 shows the components of modeled C_{eb} along with the measured values at room temperature. For all of the bias points measured it can be seen that the diffusion capacitance dominates. Diffusion capacitance is due to the enhanced distribution of minority charge in the base during the forward bias condition and is expected to increase with temperature as shown in Figure 4-16. In the absence of saturation, C_{eb} increases by an average of 0.8% per°C.

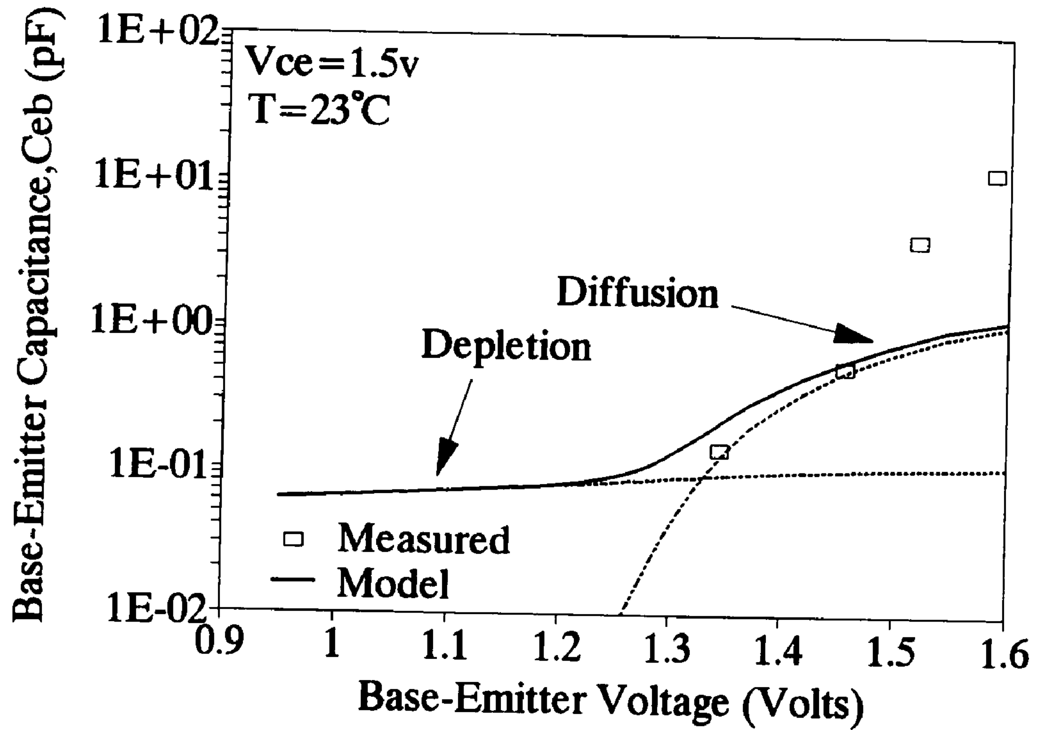

Figure 4-15. Model calculation of base-emitter capacitance showing depletion and diffusion components.

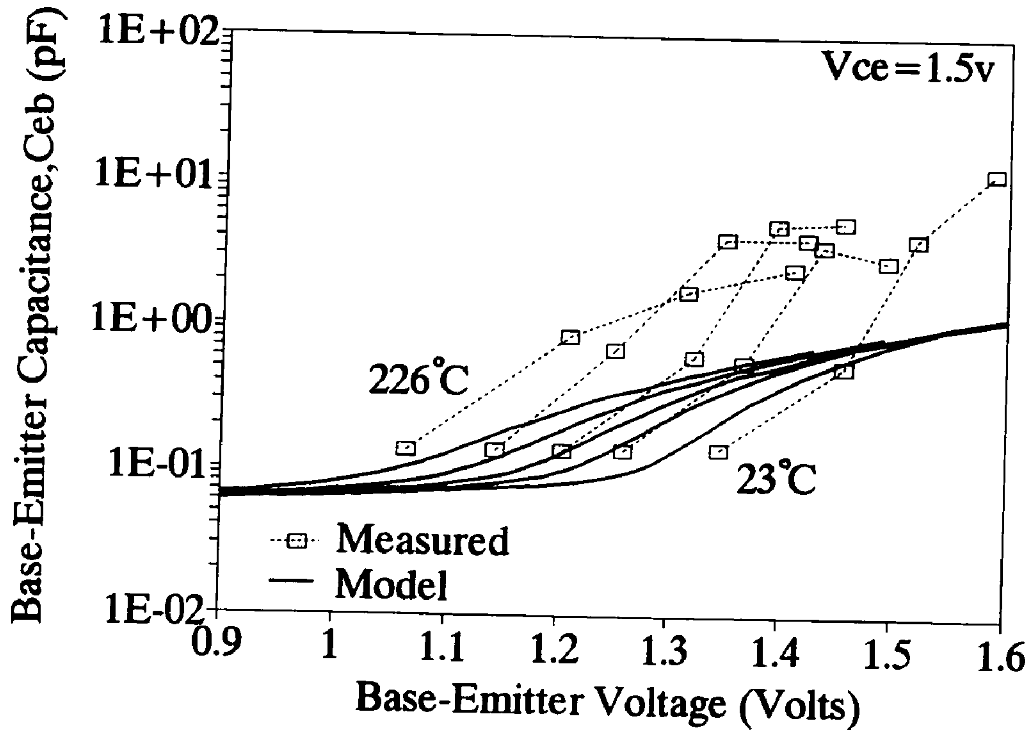

Figure 4-16. Model calculations and measurements of the base-emitter capacitance, C_{eb}.

4.3.2.2 Error Analysis

There is a certain error in the magnitude of the model calculations as well as in the way the curves saturate at high V_{be}. As mentioned earlier, the difference in saturation behavior is due to the fact that single values of parasitic base and emitter resistances were used for the calculations. This choice was made since the goal of this work is to analyze the *intrinsic* HBT temperature effects. The error arises since these resistances, particularly the base resistance, are actually distributed and change with bias. In addition, these resistor values used in the calculations were obtained experimentally from dc analyses and are expected to be somewhat different at microwave frequencies. Figure 4-17 shows the measured base and emitter parasitic resistances. The emitter resistance, R_e, which has a large effect on the saturation behavior, was generally found to be smaller than the dc value, in addition to being bias- and temperature-dependent. Over the measured bias range, R_e changes in some cases by 70%. The difference in saturation behavior between the measured and modeled microwave element values is due mainly to this change in R_e and is consistent among all of the elements.

Also related to this error in resistance values is an error due to the general use of a one-dimensional model. In general, a one-dimensional model has been found to be accurate to first order for the HBT. However, there are certainly two-dimensional effects present, including non-uniform distributions of current and voltage as well as non-uniform distributions of temperature.

Additional error is introduced from the accumulated error from the large number of material parameters used as inputs. These parameters such as the mobility, bandgap,

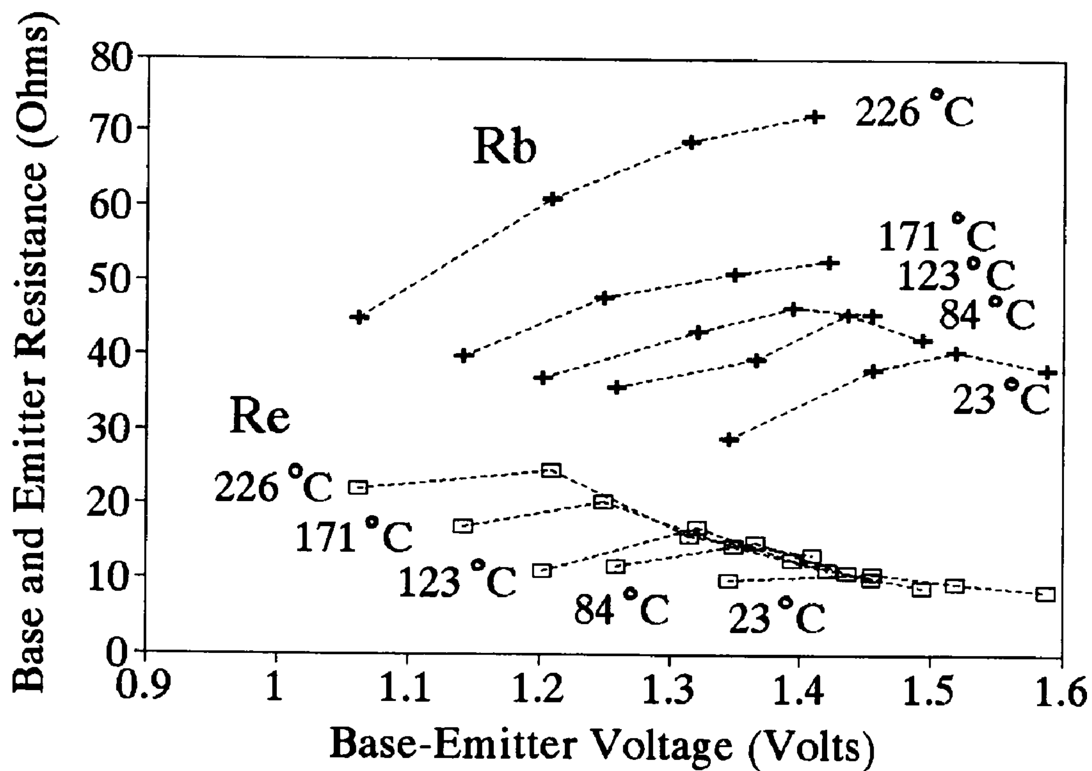

Figure 4-17. Measured parasitic base and emitter resistances versus base-emitter voltage. For the physics-based model calculations these resistances are assumed to be constant.

and intrinsic carrier concentration are formulas fit to measured data and therefore have some error. In addition, these parameters can have a significant variance when considering devices grown and processed at different facilities. An analysis of the total error has been performed by evaluating the model allowing the values of material properties to vary by $\pm 20\%$ and the parasitic resistances to vary by $\pm 70\%$. Figure 4-18 through Figure 4-20 show this accumulated error for the considered microwave elements at room temperature.

The device used in this particular analysis is not representative of the current

state-of-the-art, having a relatively large surface recombination, and large base resistance. It is still very useful for demonstrating the methodology of extracting the temperature dependence of the microwave circuit elements, and for comparing the magnitudes of change with those from device physics.

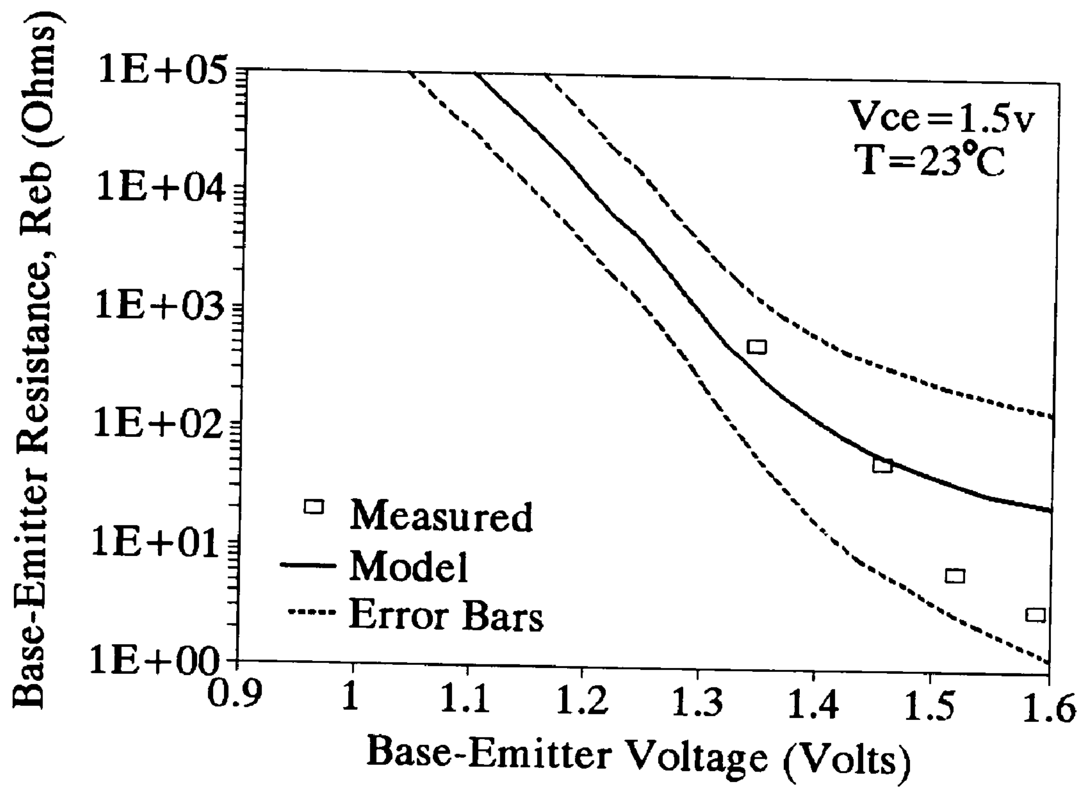

Figure 4-18. Error analysis for R_{eb}, accounting for a ±20% error in material parameters and a ±70% change in parasitic resistances.

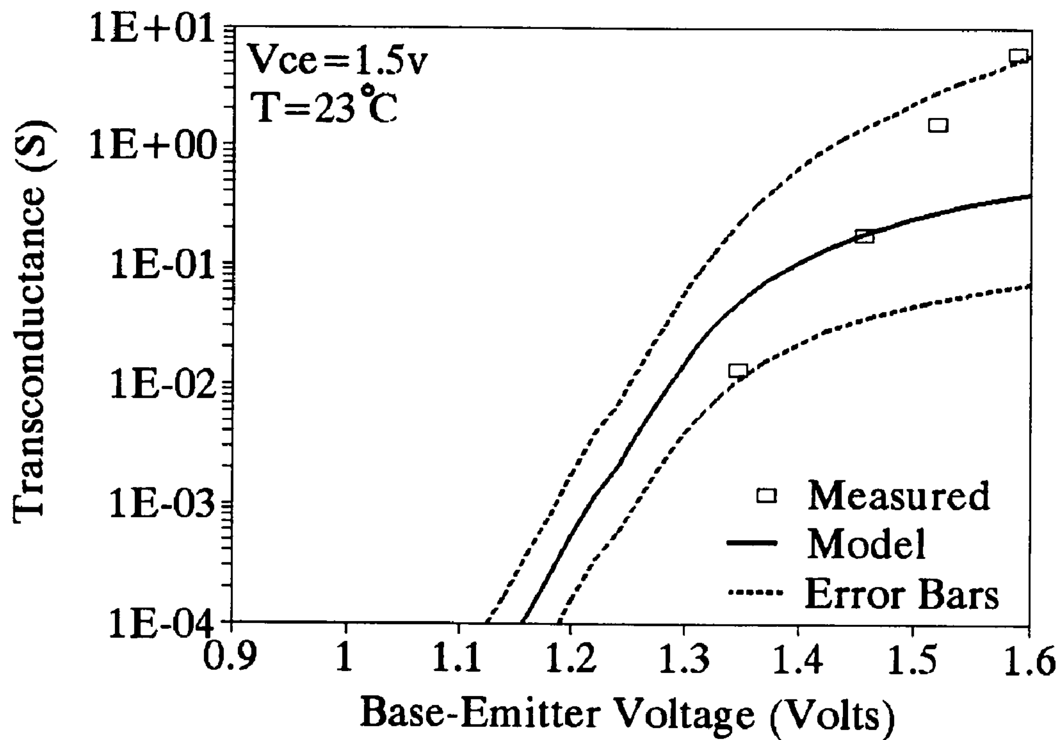

Figure 4-19. Error analysis for g_m under the same conditions as for Figure 4-18.

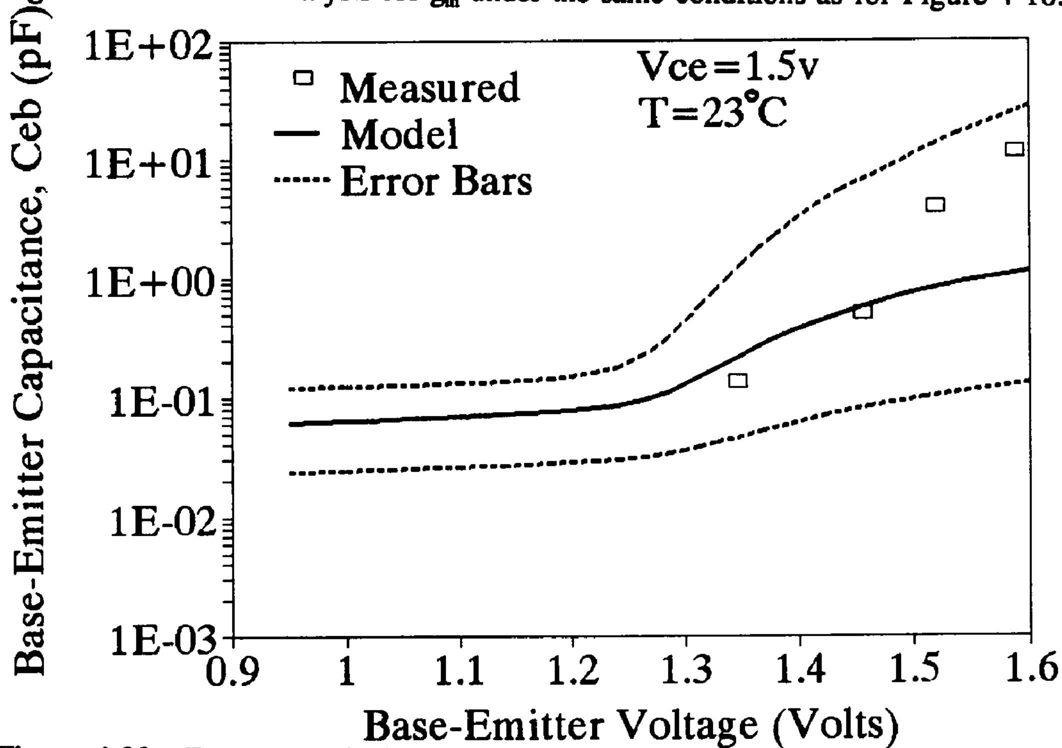

Figure 4-20. Error analysis for C_{eb} under the same conditions as for Figure 4-18.

4.3.2.3 Transit Times and Cutoff Frequencies

A useful measure of the overall high frequency performance of a transistor is the unity gain cutoff frequency, f_T, and the maximum frequency of oscillation, f_{MAX}. These can be calculated from measured S-parameters through conversions to H-parameters and power gain characteristics [105]. These quantities are illustrated in Figure 4-21 for a particular bias point, where f_T is the 0 dB intercept of $|H21|$ and f_{MAX} is the 0 dB intercept of the maximum available gain/maximum stable gain. The values of f_T and f_{MAX} can also be estimated from circuit theory and device physics as [30,106,107]

$$f_T = \frac{1}{2\pi\tau_{ec}} \tag{4-4}$$

$$f_{MAX} = \sqrt{\frac{f_T}{8\pi R_b C_C}} \tag{4-5}$$

where the transit times are

$$\tau_{ec} = \frac{V_T}{I_c}(C_{eb} + C_{bc}) + \tau_b + \frac{X_d}{2V_{sat}} + R_c C_c \tag{4-6}$$

$$\tau_b = \frac{W_b^2}{2V_T\,\mu_{nb}} + \frac{W_b}{v_{sat}} \tag{4-7}$$

V_T is the thermal voltage (kT/q), C_c is the total collector capacitance ($C_{ce}+C_{cb}$), and X_d is the base-collector depletion width.

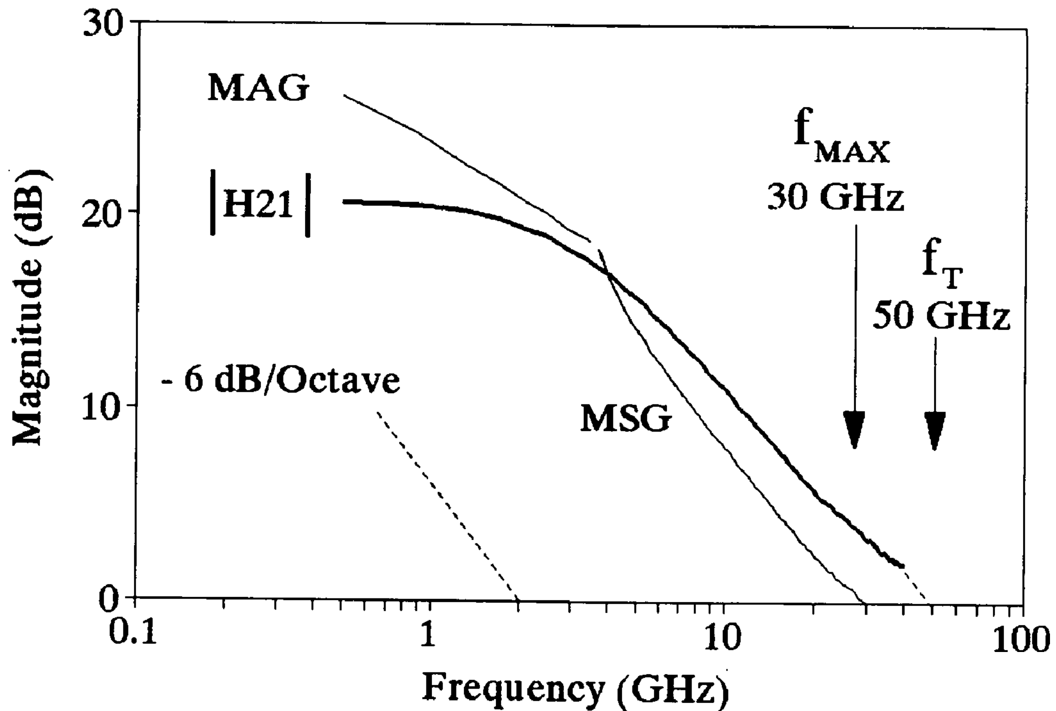

Figure 4-21. Measurements of |H21| and maximum available gain/maximum stable gain, showing the f_{MAX} and f_T figures of merit.

There are several terms in τ_{cc} which produce conflicting effects with increasing V_{be} bias and increasing temperature, but the overall effect for τ_{cc} is to decreases with increasing V_{be} bias due to the exponential increase in I_c. In response, f_T increases with bias. Both f_T and f_{MAX} have been calculated and measured for the HBT in the previous analysis at all the bias points and are shown in Figure 4-22 and Figure 4-23. There is a discrepancy between the overall magnitudes between the measured and model due to the model uncertainty described earlier. However, the trends agree well in both magnitude and direction of change.

Figure 4-24 and Figure 4-25 show the same f_T and f_{MAX} data plotted as a function of temperature for constant I_b. Again, the relative magnitude and direction of change

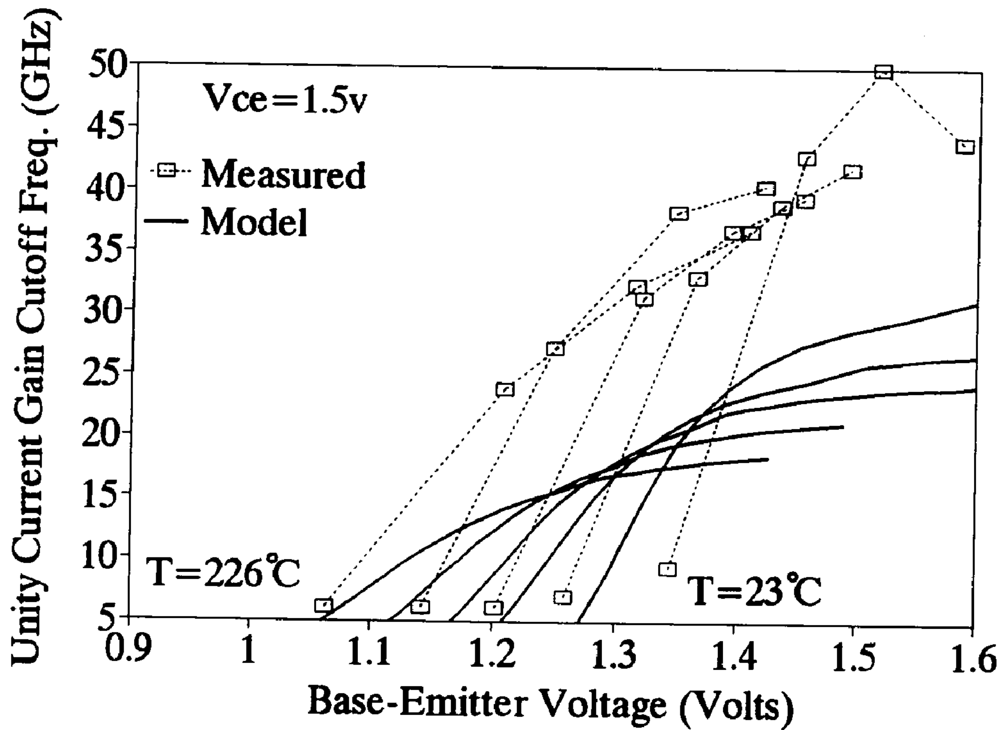

Figure 4-21. Model calculations and measurements of unity gain cutoff frequency, f_T.

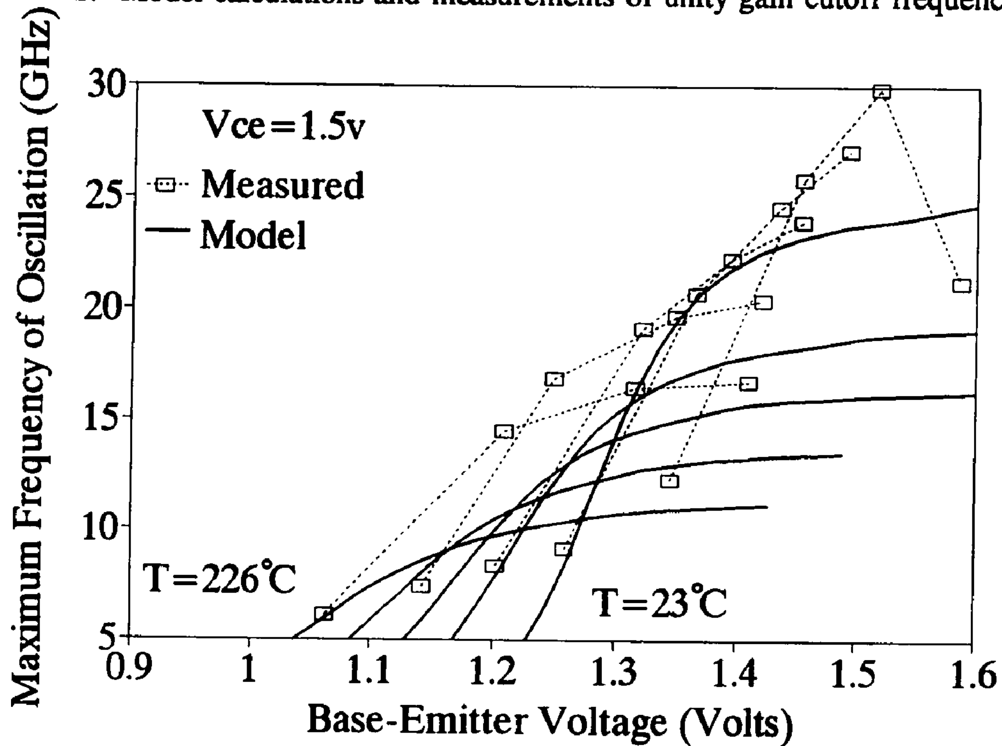

Figure 4-22. Model calculations and measurements of maximum frequency of oscillation, f_{MAX}.

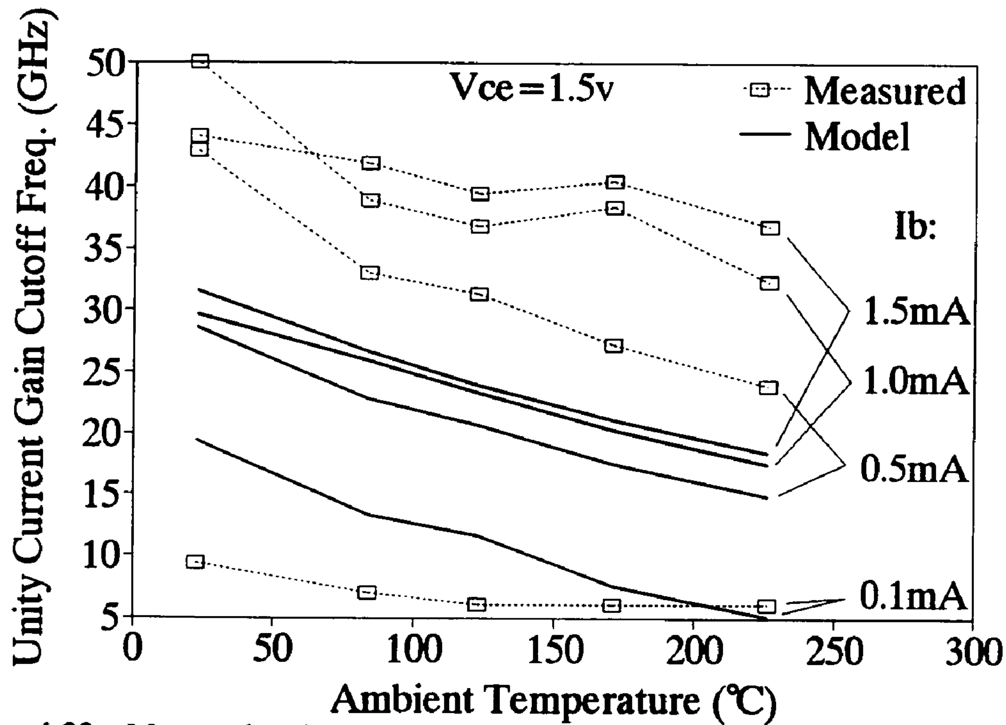

Figure 4-23. Measured and modeled f_T as a function of temperature.

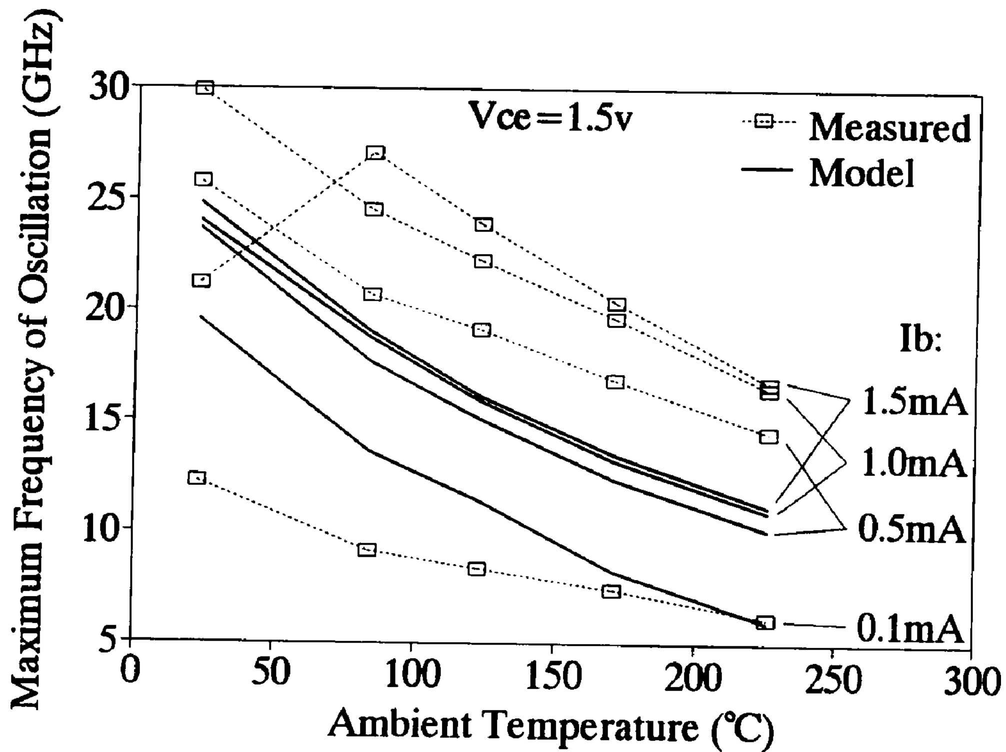

Figure 4-24. Measured and modeled f_{MAX} as a function of temperature.

agree well, indicating a drop in f_T of approximately 0.2% per°C and a drop in f_{MAX} of 0.3% per°C. The added temperature dependance of f_{MAX} is due to the increasing parasitic base resistance with temperature. These percentage drops in cutoff frequencies are useful for estimating the temperature dependence for other devices at varying power dissipation levels and varying ambients. In addition, these values show qualitative agreement with others' strictly numerical modeling work [108,109] and a report on low-temperature HBT measurements [110].

Chapter 5
CONCLUSION

In this work, the effect of an increased junction temperature on the HBT has been characterized and modeled. Measurements and analysis were performed under a wide range of stimulus conditions including dc, pulsed, and microwave . Under these conditions, elevated ambient temperature and self-heating effects were measured and analyzed to result in expressions suitable for incorporation into equivalent circuit models. Modeling was performed for these conditions using several techniques including one-dimensional numerical modeling based on semiconductor physics, as well as large signal and small signal equivalent circuit modeling.

5.1 OVERVIEW

The dependence of the HBT I-V characteristics on temperature was theoretically evaluated to determine the most temperature-sensitive components. A variation in junction temperature was shown to have the largest effect on the base-emitter diode characteristics and the current gain. The significant temperature dependence of these two aspects of the HBT is supported by experimental observations and is the focus of this work. Other aspects of the HBT, such as transit times and parasitic elements, have also been analyzed versus temperature as necessary to complete the understanding and modeling.

The characterization of dc thermal effects has been accomplished in two types of

measurements: those involving elevated ambient temperatures and those involving device self-heating. In the elevated ambient condition, measurements were performed inside of an oven up to 200°C. At constant base-emitter voltage V_{be}, the base current I_b, was found to increase exponentially with temperature. At constant I_b, V_{be} was found to decrease linearly with temperature typically by 1.4 mV/°C. This linear dependence was found to be consistent for a range of base current levels and collector voltages and was used as a calibration of the device for subsequent measurements. Also during elevated ambient measurements, the current gain was found to decrease as expected from theoretical evaluations.

The HBT was also characterized at room temperature for a wide range of dc power dissipation levels. These measurements evaluate the self-heating that takes place by using the I_b-V_{be} calibrated characteristics. The thermal resistance was calculated using these dc techniques and found to be approximately 2.9°C/mW. This high value is due to the large thermal resistivity of the 25 mil GaAs substrate. The dc current gain was also evaluated at constant I_b and shown to have a linear decrease with temperature. By extracting this temperature-dependence a technique was shown to evaluate other high-power effects separately.

For the dc condition, one dimensional physical modeling was performed, as well as large signal equivalent circuit modeling. The physical modeling, based on material parameters and geometry, was used to confirm and explain the observed characteristics with temperature. The magnitude and direction of both the base I-V and current gain thermal effects agreed well with measured data. This physical model was also used as

a starting point for estimating small signal equivalent circuit element values for subsequent microwave modeling.

A large signal temperature-dependent equivalent circuit model was also developed and used to simulate dc characteristics. Element values were dynamically changed by the model based on the actual calculated junction temperature derived from the device power dissipation. The equivalent circuit topology and equations were implemented in a commercial microwave circuit simulator as a user-defined model, and exhibited excellent agreement with dc measurements. Being incorporated into this simulator, the model can also be used for pulsed and microwave simulations.

Pulsed I-V measurements were performed to characterize the HBT before self-heating had occurred, as well as to characterize the thermal time-constant associated with the heating. 110 ns pulsed measurements of collector current were performed at duty cycles as low as 0.1% to obtain sets of I_c-V_{ce} characteristics. These demonstrated a dramatic reduction in the current gain thermal effect. In addition, these measurements agreed well with the calculations of room temperature gain based solely on dc and elevated ambient measurements. The dynamic base I-V characteristics were also observed to agree with dc high temperature measurements.

Long pulse-width measurements were performed to determine the thermal time-constant for the self-heating which was found to be 0.5μs. This was used in conjunction with thermal resistance to evaluate a thermal capacitance for the device.

The previous large signal equivalent circuit was also used to simulate pulsed

characteristics. The portion of the model which determines junction temperature was based on circuit theory and used a thermal capacitance to create the observed time constant for self-heating. Simulations agreed with measurements to first order, exhibiting all the observed effects, but in slightly smaller magnitude.

S-parameter measurements were performed at microwave frequencies for a wide range of bias conditions and ambient temperatures. Effects observed from the raw data included a drop in frequency response with temperature, specifically f_T decreased by approximately 0.2% per°C and f_{MAX} decreased by 0.3% per°C. Small signal equivalent circuit parameters at constant V_{be} were extracted from the S-parameter data up to 10 GHz for all temperatures. The base-emitter resistance was found to decrease with temperature by an average of 1.3% per°C while the base-emitter capacitance increased by 0.8% per°C. The gain element, transconductance, was found to increase by 1.4% per°C at constant V_{be}. It was shown that this increase of transconductance at constant V_{be} is consistent with a decrease in current gain at constant I_b.

One dimensional physical modeling was used to confirm the trends observed from the measured element values versus temperature. This modeling is an extension of the dc physical modeling and agreed with the magnitude and direction of change in measured element values. The absolute magnitudes between the measured and modeled elements exhibited some error which was evaluated and shown to be consistent with a $\pm$40% error in the material constants for model inputs.

5.2 APPLICATIONS

The characterization results and modeling tools developed for this work have application for improving HBT device and circuit design specifically for high power operation. The characterization results give general trends attributed to increased junction temperature, separating them from other high power effects. Also provided is the ability to estimate the high-power dc and frequency performance from a small set of measured data. The modeling tools can be used to enhance discrete device performance by predicting responses to changes in the physical HBT structure. Circuit performance can be enhanced by using the large signal model to design-in thermal effects before the fabrication process. The combination of the characterization techniques and the modeling developed in this work are valuable for predicting final packaged device performance using only on-wafer measurements. This can provide significant cost reduction in development cycles. The effect of different heat sink thermal resistivities on device performance can be evaluated and power-dissipation limits can be determined in all modes of operation including dc, pulsed and CW.

5.3 FUTURE RESEARCH

From the bias- and temperature-dependent small signal characterization and modeling, a microwave large signal temperature-dependent model can be developed which has its basis on device physics. Microwave large signal elements will dynamically follow the locus of small signal elements versus bias for a particular temperature. In

addition, the actual and theoretical change in this locus with temperature has been presented and can be added to the large signal dependencies.

Since the currently existing large signal model is based on room temperature microwave measurements, and on dc and pulsed thermal effects, it can be used effectively to develop biasing topologies which reduce the dependence of circuit performance on temperature. for instance, if an HBT is biased with constant V_{be} instead of constant I_b, the base I-V temperature effects partially compensate for the gain reduction effect on collector current. A strictly constant V_{be} bias, however, can lead to thermal runaway through the exponential increase of I_b with temperature. Based on the developed models of these effects, circuit topologies which are adaptive in nature can maintain constant dc and microwave performance over a range of bias and input power levels.

REFERENCES

[1] W. Shockley, "Circuit Element Utilizing Semiconductive Material," U.S. Patent No. 2,569,347, Filed June 26, 1948, Issued September 25, 1951.

[2] N.L. Wang, *et al.*, "Millimeter-Wave AlGaAs-GaAs HBT Power Operation," IEEE Microwave and Guided Wave Letters, Vol. 2, No. 10, October 1992, pp. 397-399.

[3] W.J. Ho, *et al.*, "Producibility and Performance of the Microwave Power HBT," 1992 GaAs IC Symposium, pp. 263-266.

[4] C.S. Wu, *et al.*, "High Efficiency X-Band Power HBT's," 1992 GaAs IC Symposium, pp. 259-262.

[5] N.L. Wang, *et al.*, "Ultrahigh Power Efficiency Operation of Common-Emitter And Common-Base HBT's at 10 GHz," IEEE Transactions on Microwave Theory and Techniques, Vol. 38, No. 10, October 1990, pp. 1381-1389.

[6] N.L. Wang, *et al.*, "18 GHz High Gain, High Efficiency Power Operation of AlGaAs/GaAs HBT," 1990 IEEE MTT-S Digest, pp. 997-1000.

[7] B. Bayraktaroglu, *et al.*, "Monolithic X-Band Heterojunction Bipolar Transistor Power Amplifiers," 1989 GaAs IC Symposium, pp. 271-274.

[8] M.A. Khatibzadeh, *et al.*, "High Power and High Efficiency Monolithic HBT VCO Circuit," 1989 GaAs IC Symposium, pp. 11-14.

[9] M.A. Khatibzadeh and B. Bayraktaroglu, "High-Efficiency, Class-B, S-Band Power Amplifier," 1990 IEEE MTT-S Digest, pp. 993-996.

[10] R. Ramachandran, *et al.*, "A High-Efficiency HBT MMIC Power Amplifier," 1990 GaAs IC Symposium, pp. 357-360.

[11] N.L. Wang, *et al.*, "4W, 7-12 GHz, Compact CB HBT MMIC Power Amplifier," 1992 GaAs IC Symposium, pp. 301-304.

[12] K.W. Kobayashi, *et al.*, "GaAs Heterojunction Bipolar Transistor MMIC DC to 10 GHz Direct-Coupled Feedback Amplifier," 1989 GaAs IC Symposium, pp. 87-90.

[13] K.W. Kobayashi, *et al.*, "Integrated Complementary HBT Microwave Push-Pull and Darlington Amplifiers with PNP Active Loads," 1992 GaAs IC Symposium, pp. 313-316.

[14] M.G. Adlerstein, *et al.*, "High Power Density Pulsed X-Band Heterojunction Bipolar Transistors," Electronics Letters, Vol. 27, No.2, 17 January 1991, pp. 148-149.

[15] S.M. Sze, Physics of Semiconductor Devices, John Wiley & Sons Inc., New York, 1981.

[16] S. Adachi, "GaAS, AlAs, and $Al_xGa_{1-x}As$: Material Parameters for use in Research and Device Applications," Journal of Applied Physics 58, August 1985, pp. R1-R29.

[17] C.D. Thurmond, "The Standard Thermodynamic Function of the Formation of Electrons and Holes in Ge, Si, GaAs, and GaP," Journal of the Electrochemical Society 122, 1975, p. 1133.

[18] D.D. Tang, "Heavy Doping Effects in p-n-p Bipolar Transistors," IEEE Transactions on Electron Devices vol. ED-27, no. 3, March 1980, pp. 563-570.

[19] W.M. Bullis, *et al.*, "Temperature Coefficient of Resistivity of Silicon and Germanium Near Room Temperature," Solid-State Electronics vol. 11, 1968, pp. 639-646.

[20] L.L. Liou, J. Ebel and C.I. Huang, "Thermal Effects on the Characteristics of AlGaAs/GaAs Heterojunction Bipolar Transistors Using Two-dimensional Numerical Simulation," to be published: IEEE Trans. on ED, Jan. 1993.

[21] J.S. Blakemore, "Semiconducting and Other Major Properties of Gallium Arsenide," Journal of Applied Physics 53, October 1982, pp. R123-R181.

[22] M. Neuberger, Handbook of Electronic Materials, Volume 2, "III-V Semiconducting Compounds," IFI/Plenum, New York, 1971, pp. 15-17.

[23] R.S. Muller and T.I. Kamins, Device Electronics for Integrated Circuits, John Wiley & Sons, New York, 1986.

[24] P.R. Gray and R.G. Meyer, Analysis and Design of Analog Integrated Circuits, Second Edition, John Wiley & Sons, New York, 1984.

[25] B.G. Streetman, Solid State Electronic Devices, Prentice-Hall, Inc, Englewood Cliffs, NJ, 1980.

[26] D. Buhanan, "Investigation of Current-Gain Temperature Dependence in Silicon Transistors," IEEE Transactions on Electron Devices ED16, No. 1, January 1969, pp. 117-124.

[27] S. Selberherr, Analysis and simulation of Semiconductor Devices, Springer-VerlangWien, New York, 1984.

[28] H. Kroemer, "Heterostructure Bipolar Transistors and Integrated Circuits," Proceedings of the IEEE, Vol. 70, No. 1, January 1982, pp. 13-25.

[29] S. Tiwari, Compound Semiconductor Device Physics, Academic Press, Harcourt Brace Jovanovich, New York, 1992.

[30] F. Ali and A. Gupta, HEMTs and HBTs: Devices, Fabrication, and Circuits, Artech House, Boston, 1991.

[31] B.R. Ryum and I.M. Abdel-Motaleb, "Investigation of Current Transport and Charges in Graded Base HBTs," IEEE 1990 Bipolar Circuits and Technology Meeting, pp. 199-202.

[32] S-C Lee, *et al.*, "Origin of High Offset Voltage in an AlGaAs/GaAs Heterojunction Bipolar Transistor," Applied Physics Letters 45(10), 15 November 1984, pp. 1114-1116.

[33] A. Marty, *et al.*, "Electrical behavior of an NPN GaAlAs/GaAs Heterojunction Transistor," 1979 Solid-State Electronics, Vol. 22, pp. 549-557.

[34] K. Lee and M. Shur, "Electron Density of the Two-Dimensional Electron Gas in Modulation Doped Layers," Journal of Applied Physics, 54(4), April 1983, pp. 2093-2096.

[35] A.H. Marshak, "Transport Equations for Highly Doped Devices and Heterostructures," 1987 Solid-State Electronics, Vol. 30, No. 11, pp. 1089-1093.

[36] W. Liu, and J.S. Harris, Jr., "Diode Ideality Factor for Surface Recombination Current in AlGaAs/GaAs Heterojunction Bipolar Transistors," IEEE Transactions on Electron Devices, Vol. 39, No. 12, December 1992, pp. 2726-2731.

[37] C.J. Sandroff, *et al.*, "Dramatic Enhancement in the gain of a GaAs/AlGaAs Heterojunction Bipolar Transistor by Surface Chemical Passivation," Applied Physics Letters, 51(2), 6 July 1987, pp. 33-35.

[38] M. Kurata and J. Yoshida, "Modeling and Characterization for High-Speed GaAlAs-GaAs n-p-n Heterojunction Bipolar Transistors," IEEE Transactions on Electron Devices, Vol. 31, No. 4, April 1984, pp. 467-473.

[39] B. Willén and U. Westergren, "The Temperature Dependent Current Gain of Heterojunction Bipolar Transistors," Microelectronic Engineering 15, 1991, pp. 317-320.

[40] R.M. Warner, Jr. and B.L. Grung, Transistors, Fundamentals for the integrated-Circuit Engineer, John Wiley & Sons, New York, 1983.

[41] H.C. DeGraaff, J.W. Slotboom, and A. Schmitz, "The Emitter Efficiency of Bipolar Transistors," Solid-State Electronics Vol. 20, 1977, pp. 515-521.

[42] S.I. Long, "A Comparison of the GaAs MESFET and the AlGaAs/GaAs Heterojunction bipolar Transistor for Power Microwave Amplification," IEEE Transactions on Electron Devices ED36, no. 7, 1989, pp. 1274-1278.

[43] W.P. Dumke, "The Effect of Base Doping on the Performance of Si Bipolar Transistors at Low Temperatures," IEEE Transactions on Electron Devices ED28, No. 5, May 1981, pp. 494-500.

[44] W.W. Gartner, "Temperature Dependence of Junction Transistor Parameters," Proceedings of the IRE, May 1957, pp. 662-680.

[45] P.C. Grossman, A. Oki, " A Large Signal DC Model for GaAs/$Ga_{1-x}Al_xAs$ Heterojunction Bipolar Transistors," Proceedings of the 1989 Bipolar Circuits and Technology Conference, pp. 258-261.

[46] W.L. Kauffman and A.A. Bergh, "The Temperature Dependence of Ideal Gain in Double Diffused Silicon Transistors," IEEE Transactions on Electron Devices, October 1968, pp. 732-735.

[47] J.D. Cressler, *et al.*, "On the Low-Temperature Static and Dynamic Properties of High-Performance Silicon Bipolar Transistors," IEEE Transactions on Electron Devices ED36, No.8, august 1989, pp. 1489-1502.

[48] J.W. Slotboom and J.C. DeGraaff, "Measurements of Bandgap Narrowing in Si Bipolar Transistors," Solid-State Electronics Vol. 19, 1976, pp. 857-862.

[49] H.M. Rein, J.V. Rohr and P. Wennekers, "A Contribution to the Current Gain Temperature Dependence of Bipolar Transistors," Solid-State Electronics Vol. 21, 1978, pp. 439-442.

[50] H.J.J. DeMan, "The Influence of Heavy Doping on the Emitter Efficiency of a Bipolar Transistor," IEEE Transactions on Electron Devices ED18, No. 10, October 1971, pp. 833-834.

[51] PSPICE Simulation. MicroSym Corp., Irvine, CA.

[52] F. Bergmann and D. Gerstner, "Some New Aspects of Thermal Instability of the Current Distribution in Power Transistors," IEEE Transactions on Electron Devices ED13, No. 8 August 1966, pp. 630-634.

[53] G.C.M. Meijer, "Thermal Sensors Based on Transistors," Sensors and Actuators vol. 10, September-October 1986, pp. 103-125.

[54] M.P. Timko, "A Two-Terminal IC Temperature Transducer," IEEE Journal of Solid-State Circuits, Vol. 11, No. 6, December 1976, pp. 784-788.

[55] G.V. Mânduteanu, "A New Device-A Power Semiconductor Diode with an Integrated Thermal Sensor," IEEE Transactions on Electron Devices, Vol. 35, No. 5, May 1988, pp. 700-703.

[56] M.E. Hafizi, C.R. Crowell, M.E. Grupen, "The DC Characteristics of GaAs/AlGaAs Heterojunction Bipolar Transistors with Application to Device Modeling," IEEE Transactions on Electron Devices ED37, No. 10, October 1990, pp. 2121-2129.

[57] N. Chand, *et al.*, "Temperature Dependence of current Gain in AlGaAs/GaAs Heterojunction Bipolar Transistors," Applied Physics Letters 45(10), 15 November 1984, pp. 1086-1088.

[58] G.B. Gao, *et al.*, "Emitter Ballasting Resistor Design for, and Current Handling Capability of AlGaAs/GaAs Power Heterojunction Bipolar Transistors," IEEE Transactions on Electron Devices, Vol. 38, No. 2, February 1991, pp. 185-196.

[59] J.S. Kofol, *et al.*, "A Backside Via Process For Thermal Resistance Improvement Demonstrated Using GaAs HBTs," 1992 GaAs IC Symposium, pp. 267-270.

[60] F.M. Yamada, *et al.*, "Reliability analysis of microwave GaAs/AlGaAs HBTs with Beryllium and Carbon Doped Base," 1992 IEEE MTT-S Digest, pp. 739-742.

[61] D.H. Smith, "Estimating GaAs IC Operating Temperatures," Applied Microwave, Winter 1993, pp. 82-86.

[62] D.H. Smith, "Predicting Operating Temperatures for GaAs ICs," 1991 GaAs IC Symposium, pp. 187-190.

[63] B.S. Siegel, "Measuring Thermal resistances is the Key to a Cool Semiconductor," Electronics, July 6, 1978, pp. 121-126.

[64] D.B. Estreich, "A DC Technique for Determining GaAs MESFET Thermal Resistance," IEEE Transactions on Components, Hybrids, and Manufacturing Technology, Vol. 12, No. 4, December, 1989, pp. 675-679.

[65] W.J. Roesch, "Thermo-Reliability Relationships of GaAs ICs," 1988 GaAs IC Symposium, pp. 61-64.

[66] D.E. Dawson, *et al.*, "CW Measurement of HBT Thermal Resistance," IEEE Transactions on Electron Devices, Vol. 39, No. 10, October 1992, pp. 2235-2239.

[67] M.G. Adlerstein and M.P. Zaitlin, "Thermal Resistance Measurements for AlGaAs/GaAs Heterojunction Bipolar Transistors," IEEE Transactions on Electron Devices, Vol. 38, No. 6, June 1991, pp. 1553-1554.

[68] C. Canali, *et al.*, "Correlation Between Fabrication Processes and Thermal Distribution in Medium Power MESFETs," Microelectronic Reliability, Vol. 29, No. 4, 1989, pp. 499-504.

[69] X. Gui, *et al.*, "Simulation Study of Peak Junction Temperature and Power Limitation of AlGaAs/GaAs HBT's Under Pulsed and CW Operation," IEEE Transactions on Electron Devices, Vol. 13, No. 8, August 1992, pp. 411-413.

[70] R.D. Lindsted, and R.J. Surty, "Steady-State Junction Temperatures of Semiconductor Chips," IEEE Transactions on Electron Devices, Vol. 19, No. 1, January, 1972, pp. 41-44.

[71] G.B. Gao, *et al.*, "Thermal Design Studies of High-Power Heterojunction Bipolar Transistors," IEEE Transactions on Electron Devices, Vol. 36, No. 5, May 1989, pp. 854-862.

[72] D.S. Whitefield, C.J. Wei, and J.C.M. Hwang, "High Power Characterization of Heterojunction Bipolar Transistors," 1992 IEEE Princeton Section Sarnoff Symposium, Session II.

[73] EEsof Inc., Westlake Village, California.

[74] D.S. Whitefield, C.J. Wei, and J.C.M. Hwang, "Temperature-Dependent Large Signal Model of Heterojunction Bipolar Transistors," 1992 GaAs IC Symposium, pp. 221-224.

[75] J.J. Ebers, and J.L. Moll, "Large-Signal Behavior of Junction Transistors," Proceedings of the IRE, December 1954, pp. 1761-1772.

[76] F.F. Oettinger, *et al.*, "Thermal Characterization of Power Transistors," IEEE Transactions on Electron Devices, Vol. 23, No. 8, August 1976, pp. 831-838.

[77] R.T. Dennison and K.M Walter, "Local Thermal Effects in High Performance Bipolar Devices/Circuits," 1989 IEEE Bipolar Circuits and Technology Meeting, pp. 164-167.

[78] P. Antognetti, and G. Massobrio, Semiconductor Device Modeling with SPICE, McGraw-Hill Book Company, New York, 1988, pp. 62-64.

[79] Touchstone & Libra Utilities Manual, EEsof Inc., Westlake Village, California, pp. 3-1 - 3-17.

[80] R.J. Trew, *et al.*, "Microwave Performance of n-p-n and p-n-p AlGaAs/GaAs Heterojunction Bipolar Transistors," IEEE Transactions on Microwave Theory and Techniques, December 1988, pp. 1869-1873.

[81] D. Costa, *et al.*, "A New Direct Method for Determining the Heterojunction Bipolar Transistor Equivalent Circuit Model," IEEE 1990 Bipolar Circuits and Technology Meeting, pp. 118-121.

[82] D.R. Pehlke and D. Pavlidis, "Direct Calculation of the HBT Equivalent Circuit From Measured S-Parameters," 1992 IEEE MTT-S Digest, pp. 735-738.

[83] B. Meskoob, *et al.*, "Bias-Dependence of the Intrinsic Element Values of InGaAs/InAlAs/InP Inverted Heterojunction Bipolar Transistor," IEEE Transactions on Electron Devices vol. 40 no. 5, May 1992, pp. 1012-1014.

[84] R.J. Trew, *et al.*, "A Parameter Extraction Technique for Heterojunction Bipolar Transistors," 1989 IEEE MTT-S Digest, pp. 897-900.

[85] S. Lee and A. Gopinath, "Parameter Extraction Technique for HBT Equivalent Circuit Using Cutoff Mode Measurement," IEEE Transactions on Microwave Theory and Techniques, Vol. 40, No. 3, March 1992, pp. 574-577.

[86] M.Y. Frankel, *et al.*, "Large-Signal Modeling and Study of Power Saturation Mechanisms in Heterojunction Bipolar Transistors," 1991 IEEE MTT-S Digest, pp. 127-130.

[87] M.Y. Frankel and D. Pavlidis, "An Analysis of the Large-Signal Characteristics of AlGaAs/GaAs Heterojunction Bipolar Transistors," IEEE Transactions on Microwave Theory and Techniques, vol. 40 No. 3, March 1992, pp. 465-474.

[88] D.A. Teeter, *et al.*, "Large Signal Characterization and Numerical Modeling of the GaAs/AlGaAs HBT," 1991 IEEE MTT-S Digest, pp. 651-654.

[89] C.T. Matsuno, *et al.*, "A Large-Signal HSPICE Model for the Heterojunction Bipolar Transistor," IEEE Transactions on Microwave Theory and Techniques, vol. 37 No. 9, September 1989, pp. 1472-1474.

[90] N. Hayama, J.I. Shimizu, and K. Honjo, "Large-Signal Parameter Modeling for AlGaAs/GaAs HBT and its application to a monolithic 22 GHz-Band Oscillator," IEICE Trans. Electron., vol E75-C, No. 6, June 1992, pp. 683-688.

[91] A. Asensio and F. Pérez, "High-Power Microwave Bipolar Transistor Modeling," Microwave and Optical Technology Letters, Vol. 5, No. 1, January 1992, pp. 10-16.

[92] P.C. Grossman, "A Physically Based Large Signal HBT Model with Self Heating and Transit Time Effects," 1991 IEEE MTT-S Digest, pp. 233-236.

[93] P.C. Grossman, "Large Signal Modeling of HBT's Including Self-Heating and Transit Time Effects," IEEE Transactions on Microwave Theory and Techniques, vol. 40 No. 3, March 1992, pp. 449-464.

[94] P. Baureis, *et al.*, "Modeling of Self-Heating in GaAs/AlGaAs HBT's for Accurate Circuit and Device Analysis," 1991 GaAs IC Symposium, pp. 125-128.

[95] P. Baureis, *et al.*, "A New Large Signal Model for Heterojunction Bipolar Transistors Including Temperature Effects," 1991 IEEE Custom Integrated Circuits Conference, pp. 23.3.1-23.3.4.

[96] H. Wang, *et al.*, "Temperature Dependence of dc Currents in HBT," 1992 IEEE MTT-S Digest, pp. 731-734.

[97] J. Fitzpatrick, "Error Models for Systems Measurement," Microwave Journal, May 1978, pp. 63-66.

[98] P. Walters, *et al.*, "On-Wafer Measurement Uncertainty for 3-Terminal Active Millimetre-Wave Devices," 1992 GaAs IC Symposium, pp. 55-58.

[99] L.L. Liou, *et al.*, "Numerical Studies of Thermal Effects on Heterojunction Bipolar Transistor Current-Voltage Characteristics Using One-dimensional Simulation," Solid-State Electronics, vol. 35 No. 4, 1992, pp. 579-585.

[100] W.M. Webster, "On the Variation of Junction-Transistor Current-Amplification Factor With Emitter Current," Proceedings of the IRE, Vol. 42, June 1954, pp. 914-920.

[101] R. Katoh and M. Kurata, "Self-Consistent Particle Simulation for (AlGa)As/GaAs HBT's Under High Bias Conditions," IEEE Transactions on Electron Devices, Vol. 36, No. 10, October 1989, pp. 2122-2128.

[102] C.T. Kirk, Jr., "A Theory of Transistor Cutoff Frequency (f_T) Falloff at High Current Densities," IRE Transactions on Electron Devices, March 1962, pp. 164-174.

[103] H.C. Poon, *et al.*, "High Injection in Epitaxial Transistors," IEEE Transactions on Electron Devices, Vol. 16, No. 5, May 1969, pp. 455-457.

[104] P.D. Maycock, "Thermal Conductivity of Silicon, Germanium, III-V Compounds and II-V Alloys," Solid-State Electronics, Vol. 10, 1967, pp. 161-168.

[105] D.M. Pozar, Microwave Engineering, Addison-Wesley Publishing Co., New York, 1990.

[106] S.C.M. Ho and D.L Pulfrey, "The Effect of Base Grading on the Gain and High-Frequency Performance of AlGaAs/GaAs Heterojunction Bipolar Transistors," IEEE Transactions on Electron Devices, Vol. 36, No. 10, October 1989, pp. 2173-2182.

[107] W. Liu, *et al.*, "Derivation of the Emitter-Collector Transit Time of Heterojunction Bipolar Transistors," 1992 Solid-State Electronics, Vol. 35, No. 4, pp. 541-545.

[108] R. Katoh and M. Kurata, "Self-Consistent Particle Simulation of Heterojunction Bipolar Transistors Under High Temperature Operating Conditions," 1989 IEEE International Electron Devices Meeting, pp. 477-480.

[109] J. Chen, *et al.*, "Thermal Dependence of HBT High-Frequency Performance," Electronics Letters, Vol. 26, No. 21, 11 October 1990, pp. 1770-1772.

[110] J. Laskar, *et al.*, "Effect of Reduced Temperature on the f_T of AlGaAs/GaAs Heterojunction Bipolar Transistors," IEEE Electron Device Letters, Vol. 12, No. 6, June 1991, pp. 329-331.

APPENDIX
TEMPERATURE DEPENDENT HBT MODEL

A.1 User Defined Element Program Listing

Within the following program listing, the text in bold is the standard 'skeleton' structure for user defined models in LIBRA. All other program lines are specific to the HBT large signal model.

```
/*************************************************************************/
/*  Nonlinear User Defined Model for Large Signal Simulation of The HBT */
/*                      program name:    full2.c                       */
/*************************************************************************/
/*    D.S. Whitefield, C.J. Wei, 3/18/92    */
#include <math.h>
#include <stdio.h>
#define  LINEAR      0
#define  NONLINEAR   1        /* define user element type */

static void void_function()
{
}

struct user_def_element
    {
    char *name;           /* element name, EIGHT characters is MAXIMUM    */
    int  node;            /* number of nodes.  if user provides           */
                           /* s matrix rather than y matrix for this       */
                           /* element, 4 is the maximum                    */
    int  nkey;            /* number of parameter names                     */
    int  keyinde          /* beginning key index to userkey[] array        */
    void (*user_fnct)();/* user function pointer                          */
    int  type;            /* can be LINEAR or NONLINEAR, if both,          */
                           /* specify NONLINEAR                            */
    };

#ifdef LINT_ARGS
  void hbt(int);
#else
  void hbt();
#endif

#define NUM_USER_ELEMENTS  1
struct user_def_element user_element[ ] = {

 {"    ", 0, 0, 0, void_function, LINEAR},    /* dummy element */
 {"hbt", 8, 32, 1, hbt, NONLINEAR},
 };  /* end of the user element structure */
```

```
#undef  LINEAR
#undef  NONLINEAR

char   *userkey[] =
{ "    ", "rb","rc","re",
        "is","nf","ise","ne",
             "nr","isc","nc",
        "a1","a2","a3","a4","a5","br",
        "cje","vje","me","t0","t1","t2",
        "cjc","vjc","mc","tr","xbc","fc",
        "temp","rth","kb","kvbe",
 } ;
int num_user_elements = NUM_USER_ELEMENTS ;
#define pi 3.141592654
#define PI 3.141592654
static float fr;        /* current frequency in Hertz */
static float zo;        /* system characteristic impedance - 50 ohms */
                        /* or as respecified in the TERM block */
static float funit;     /* frequency scale factor */
static float runit;     /* resistance scale factor */
static float gunit;     /* conductance scale factor */
static float lunit;     /* inductance scale factor */
static float cunit;     /* capacitance scale factor */
static float lenunit;   /* length scale factor */
static float tunit;     /* time scale factor */
static float angunit;   /* angle scale factor */
static float curunit;   /* current scale factor */
static float volunit;   /* volt scale factor */
                        /* user data times scale factor equals MKS units */
static int sbeg;        /* location to begin storing s-parameters */
static int flag;
#ifdef LINT_ARGS
  extern void get_global_data(float *, float *, float *, float *, float *,
                              float *, float *, float *, float *, float
*);
  extern void userdata(int, float *, int *);
  extern void set_aritherror(void);
  extern void loadyij(int, int, int, double, double) ;
  extern void loadyij_nl(int, int, int, double, double) ;
  extern void loadiq(int, double, double) ;
  extern void nodevolt(int, double *) ;
  extern char linear_analysis(void);
  extern char nonlinear_analysis(void);
#else
  extern void get_global_data();
  extern void userdata();
  extern void set_aritherror();
  extern void loadyij();
  extern void loadyij_nl();
  extern void loadiq();
  extern void nodevolt();
  extern char linear_analysis();
  extern char nonlinear_analysis();
#endif
#define sqr(x) ((x)*(x))
#define abst(x) ( ((x)>0)? (x): -(x))
#define   BOLTZ   1.3806226e-23
#define   CHARGE  1.6021918e-19
#define   CTOK    273.15
#define   TEMP    (27.0+CTOK)
#define   GMIN    1.0e-12
#define   MAXTEMP 8
```

```
#define   MAXI8   1e-3

/*-------------------------------------------------------------------*/
/*-------------------------------------------------------------------*/
void hbt(exloc)
int exloc ;
{
  double vbe,vbc,vt1,vt2,evbe,evben,evbc,evbcn,vt,vth,v13,v23;
  double ge,gc,gb,gbe,gben,gbc,gbcn, gm,go,gth,gm_th,gbe_th,gmm;
  double ibe,iben,ibc,ibcn, ic,i1,i2,i3,i8,ip;
  double cbco,cbc,czof2,cbe,ctemp,cbe4,cbe5,cbe6,cbe_th;
  double qcbc,qcbe;
  double fcbc, xfc, f1c,f2c,f3c,arg,sarg,fcbe,f1e,f2e,f3e;
  double beta,e1,e2, tb,et2,dtb,b0,dt,dtb_th,deltaT,kvbe100;
  double dp1,dp2,dp3,dp4,dp5;
  double vnode[1+8] ; /* vnode[0] not used */
  struct modelparameter
  {
    float dummy;
    float rb;    float rc;    float re;
    float is;    float nf;    float ise;   float ne;
    float nr;    float isc;   float nc;
    float a1;    float a2;    float a3;    float a4;    float a5;    float br;
    float cje;   float vje;   float me;    float t0;    float t1;    float t2;
    float cjc;   float vjc;   float mc;    float tr;    float xbc;   float fc;
    float temp;  float rth;   float kb;    float kvbe;
  };
  struct modelparameter p ;
  FILE *fout;

  if ( linear_analysis() )  /* touchstone analysis */
     { /* no touchstone model for this element */;  }
  if ( nonlinear_analysis() )  /* bias, dc transfer and HB analysis */
  {

    userdata( exloc, &p, &sbeg ) ; /* get user data */
    nodevolt( exloc, vnode ) ;     /* get node voltages of this element */

/*p.kvbe=0.0014;*/
    vbe = vnode[4] - vnode[6];
    vbc = vnode[4] - vnode[5];
    vth = vnode[8] - vnode[7];
    v13 = vnode[1] - vnode[3];
    v23 = vnode[2] - vnode[3];
    vt  = BOLTZ*TEMP/CHARGE ;
    deltaT = (vth*100 - TEMP);

/*                                              vbe thermal effects     */


/******************************** first time ***************************/
    if (flag !=99) {
      fout = fopen ("user.out","w");
      fprintf(fout,"First\n");
      flag=99;
    }
    else { fout = fopen("user.out","a"); }
    fprintf (fout,"vbe=%3e ",vbe);

    vbe =(vbe<=3)? vbe + (p.kvbe*deltaT):1;        /* get new vbe for
modeling*/
```

```
/***************************************************************************/
/********************** Current Calculation  ***************************/
/***************************************************************************/
                    /***************** Base Emitter *****************/
   vt2 = p.nf * vt ;
   if ( vbe > -10*vt2 ){                          /* forward */
      vt1 = p.ne * vt ;
      evbe  = exp(vbe/vt2) ;                      /* diode   */
      gbe   = (evbe/vt2)*p.is + GMIN ;
      ibe   = (evbe-1)*p.is + vbe*GMIN ;
      evben = exp(vbe/vt1) ;                    /* low bias recombination */
      gben  = (evben/vt1)*p.ise ;
      iben  = (evben-1)*p.ise ;
    }
    else {                                        /* reverse */
      gbe   = GMIN;
      ibe   = vbe*GMIN - p.is ;
      gben  = 0.0 ;
      iben  = -p.ise;
    }
    kvbe100 = p.kvbe*100;
    gbe_th  = kvbe100*gbe;                       /* vbe thermal effects */
    ibe     = ibe+iben;
    gbe     = gbe+ gben;
                       /******************* Base collector *************/
   vt2 = p.nr*vt ;
   if ( vbc > -10*vt2 ){
      vt1 = p.nc * vt ;
      evbc  = exp(vbc/vt2) ;
      gbc   = (evbc/vt2)*p.is + GMIN ;
      ibc   = (evbc-1)*p.is + vbc*GMIN ;
      evbcn = exp(vbc/vt1);
      gbcn  = (evbcn/vt1)*p.isc ;
      ibcn  = (evbcn-1)*p.isc ;
   }
   else {
      gbc=GMIN;
      ibc=vbc*GMIN - p.is ;
      gbcn =0.0 ;
      ibcn = -p.isc ;
   }
   ibc = ibc+ ibcn;
   gbc = gbc+ gbcn;
                         /************** Collector Current ************/
   e1   = ibe * exp(-p.a3*ibe);
   e2   = ibe * ibe * exp(-p.a5*ibe);
   b0   = p.a1 - (p.kb*deltaT);
   beta = b0 + p.a2*e1 + p.a4*e2;
   ic   = (ibe * beta) - (ibc * p.br);
                /* derivative of ic: */
   gmm  = b0 + p.a2*e1*(2 - p.a3*ibe) + p.a4*e2*(3 - p.a5*ibe);
   gm   = gbe*gmm;
   go   = -p.br*gbc;
   gm_th= gmm*gbe_th-100*ibe*p.kb;
                        /************* Resistors *******************/
   ge = (p.re <=0.0)? GMIN : (1/p.re) ;
   gc = (p.rc <=0.0)? GMIN : (1/p.rc) ;
   gb = (p.rb <=0.0)? GMIN : (1/p.rb) ;

   i1 = gb*(vnode[1]-vnode[4]);
   i2 = gc*(vnode[2]-vnode[5]);
   i3 = ge*(vnode[3]-vnode[6]);
```

```
/*****************************************************************/
/******************** Charge Calculation ************************/
/*****************************************************************/
cbco = p.cjc*p.xbc  ;
xfc  = log(1.0 - p.fc) ;
fcbc = p.fc *p.vjc ;          /******** Base Collector *************/
if (vbc < fcbc) {
  arg  = 1.0 - vbc / p.vjc ;
  sarg = exp(-p.mc * log(arg)) ;
  cbc   = (gbc*p.br*p.tr) + (cbco * sarg) ;
  qcbc  = (ibc*p.br*p.tr) + p.vjc*cbco*(1.0-arg*sarg)/(1.0 - p.mc);
}
else {
  f1c  = p.vjc * (1.0-exp((1.0-p.mc)*xfc)) / (1.0 - p.mc) ;
  f2c  = exp((1.0+ p.mc)*xfc) ;
  f3c  = 1.0 - p.fc * (1.0 + p.mc) ;
  czof2 = cbco / f2c ;
  cbc   = (gbc*p.br*p.tr) + czof2 * (f3c + p.mc * vbc / p.vjc) ;
  qcbc  = (ibc*p.br*p.tr) + cbco *  f1c + czof2 * (f3c * (vbc - fcbc)+
        (p.mc / (p.vjc + p.vjc)) *  (vbc * vbc - fcbc * fcbc)) ;
}
                        /************ Base Emitter ***************/
fcbe = p.fc *p.vje ;
if (vbe < fcbe) {
   arg  = 1.0 - vbe / p.vje ;
   sarg = exp (-p.me * log(arg)); /* without transit time initially */
   cbe  = p.cje * sarg ;
   qcbe = p.vje * p.cje * (1.0 - arg * sarg) /(1.0 - p.me) ;
}
else  {
   f1e  = p.vje * (1.0-exp((1.0-p.me)*xfc)) / (1.0 - p.me) ;
   f2e  = exp((1.0+ p.me)*xfc) ;
   f3e  = 1.0 - p.fc * (1.0 + p.me) ;
   czof2 = p.cje / f2e ;
   cbe =  czof2 * (f3e + p.me * vbe / p.vje) ;
   qcbe =  p.cje * f1e + czof2 * (f3e * (vbe - fcbe) +
           (p.me / (p.vje + p.vje)) *
          (vbe * vbe - fcbe * fcbe)) ;
}
if (vbe < 0.0) {
   cbe4 = p.cje;
   cbe6 = -p.cje;
   qcbe = p.cje * vbe;
   tb   = 0;
   cbe5 = 0;
   cbe_th= cbe4*kvbe100;
}
else {
   et2 = exp(-p.t2*ibe);
   tb   = p.t0+ p.t1*et2;            /* add transit time */
   qcbe = qcbe + ic*tb;
   dt   = -p.t1*p.t2*et2;            /* derivative of tau b */
   dtb  = gbe*dt;
   dtb_th = gbe_th*dt;
   ctemp= cbe+(Ic*dtb);
   cbe4 = ctemp + (tb*(gm+go));        /* derivative of qcbe with
                                  respect to V4 */
   cbe5 = -tb*go;                    /*           V5 */
   cbe6 = -ctemp - (tb*gm);          /*           V6 */
   cbe_th= cbe*kvbe100 + tb*gm_th + ic*dtb_th;
}
```

```
/*********************************** Thermal ***********************/
gth = 1/p.rth;
ip  = (abst(i1*(vnode[1]-vnode[3])) +
       abst(i2*(vnode[2]-vnode[3])))/100;
                          /* ip = power "current" for thermal */
i8  = (vth*gth) - (p.temp*gth)/100 - ip;
dp5 = -v23*gc/100;
dp4 = -v13*gb/100;
dp3 = -(i1+i2)/100;
dp2 = (i2/100)-dp5;
dp1 = (i1/100)-dp4;

loadyij    ( exloc, 1, 1, gb,           0.0 );
loadyij    ( exloc, 2, 2, gc,           0.0);
loadyij    ( exloc, 3, 3, ge,           0.0);
loadyij_nl( exloc, 4, 4, gb+gbc+gbe,    cbc+cbe4);
loadyij_nl( exloc, 5, 5, gbc+gc-go,     cbc );      /*  + - go */
loadyij_nl( exloc, 6, 6, gm+gbe+ge,    -cbe6 );
loadyij    ( exloc, 7, 7, gth,          0.0 );
loadyij    ( exloc, 8, 8, gth,          0.0);

loadyij    ( exloc, 1, 4, -gb,         0.0);
loadyij    ( exloc, 2, 5, -gc,         0.0);
loadyij    ( exloc, 3, 6, -ge,         0.0);
loadyij    ( exloc, 4, 1, -gb,         0.0);
loadyij_nl( exloc, 4, 5, -gbc,        -cbc+cbe5);
loadyij_nl( exloc, 4, 6, -gbe,         cbe6);
loadyij_nl( exloc, 4, 7, -gbe_th,     -cbe_th);
loadyij_nl( exloc, 4, 8,  gbe_th,      cbe_th);
loadyij    ( exloc, 5, 2, -gc,         0.0);
loadyij_nl( exloc, 5, 4,  gm+go-gbc, -cbc);
loadyij_nl( exloc, 5, 6, -gm,          0.0 );
loadyij_nl( exloc, 5, 7, -gm_th,       0.0 );
loadyij_nl( exloc, 5, 8,  gm_th,       0.0 );
loadyij    ( exloc, 6, 3, -ge,         0.0);
loadyij_nl( exloc, 6, 4, -gm-gbe-go,    -cbe4);
loadyij_nl( exloc, 6, 5,  go        ,   -cbe5);
loadyij_nl( exloc, 6, 7,  gm_th+gbe_th, cbe_th );
loadyij_nl( exloc, 6, 8, -gm_th-gbe_th,-cbe_th );
loadyij_nl( exloc, 7, 1,  dp1,          0.0 );
loadyij_nl( exloc, 7, 2,  dp2,          0.0 );
loadyij_nl( exloc, 7, 3,  dp3,          0.0 );
loadyij_nl( exloc, 7, 4,  dp4,          0.0 );
loadyij_nl( exloc, 7, 5,  dp5,          0.0 );
loadyij    ( exloc, 7, 8, -gth,         0.0 );
loadyij_nl( exloc, 8, 1, -dp1,          0.0 );
loadyij_nl( exloc, 8, 2, -dp2,          0.0 );
loadyij_nl( exloc, 8, 3, -dp3,          0.0 );
loadyij_nl( exloc, 8, 4, -dp4,          0.0 );
loadyij_nl( exloc, 8, 5, -dp5,          0.0 );
loadyij    ( exloc, 8, 7, -gth,         0.0 );

loadiq( 1, i1,             0.0);
loadiq( 2, i2,             0.0) ;
loadiq( 3, i3,             0.0) ;
loadiq( 4, (ibe-i1+ibc),  qcbc+qcbe );
loadiq( 5, (ic -i2-ibc), -qcbc);
loadiq( 6, -(ibe+ic+i3), -qcbe );
loadiq( 7, -i8,            0.0);
loadiq( 8,  i8,            0.0) ;

}
```

```
  fprintf (fout, "deltaT=%3e kvbe=%3e kb=%3e vbe=%3e b0=%3e beta=%3e
              ibe=%3e ic=%3e\n", deltaT,p.kvbe,p.kb,vbe,b0,beta,ibe,ic);
  fclose (fout);
  return ;
}
#undef   BOLTZ
#undef   CHARGE
#undef   CTOK
#undef   TEMP
#undef   GMIN
#undef   GMAX
/*-------------  END USER HBT USER DEFINED ELEMENT ------------*/
```

A.2 Example Circuit file for HBT dc Simulation

```
! CIRCUIT FILENAME: dc_full2.ckt
! DESCRIPTION:      Simulates dc Collector Characteristics for an HBT
! DATE/AUTHOR:      3/27/92 DSW
DIM
    FREQ    GHZ
    RES     OH
    IND     NH
    CAP     PF
    LNG     MIL
    TIME    PS
    COND    /OH
VAR
EQN
CKT
  S1Pa_D1     2   5      [MODEL=DBC]

  HBT_Q1    2 3 0 4 5 6 0 8 rb=13.5  rc=12.3  re=6.2                        &
            is=1.62e-27     nf=1.03  ise=3.68e-20  ne=1.551                 &
                            nr=1.3   isc=2e-16     nc=1.472                 &
            a1=1.6     a2=12981 a3=816 a4=1.004e6   a5=392.2      br=0.01   &
            cje=2e-14  vje=1.7  me=0.5 t0=5.5e-12   t1=11.9e-12   t2=3000   &
            cjc=1e-14  vjc=1.42 mc=0.5 tr=1e-11     xbc=0.3       fc= 0.5   &
            temp=300   rth=2900 tmp0=296 kb=.0038 kvbe=0.0014
  cap_cce   5  6 c=.015
  res_ro    5  6 r=10000
  cap_cth   8  0 c=172

  res_rout 10 3 r=.01
  res_rin  11 2 r=.01
  cccs_ibb 20 0 0 11 M=1 A=0 R1=1000 R2=0 F=0 T=0
  DEF2P 2 3 model1
MODEL
  DBC    D    IS=3e-16 N=1.47 CJO=4e-14
SOURCE
  model1 vs_ib    20 0
  model1 vs_vce   10 0
DCTR                                                           ! dc
  dctr1  vs_ib                                                 ! dc
  sweep  1 5 1                                                 ! dc
  dctr2  vs_vce
  sweep  0   2 .1
  sweep  2.5 8 .5
OUT
  model1 i_iin  res_rin  gr1                                   ! dc
  model1 i_out  res_rout gr2
  model1 v_vth  8 0      gr3                                   ! dc
  model1 v_vth  8 0      SCN
  model1 i_out  res_rout SCN
GRID
 dctr2  0  8  8                                                ! dc
    GR2  -5 30 35                                              ! dc
    GR3  3 6 3                                                 ! dc
    SCN
HBCNTL
  sample=2
  reltolv = 1e-5
  reltol  = 1e-5
```

A.3 Example Circuit file for HBT Pulsed Simulation

```
! CIRCUIT FILENAME: pulse_full2.ckt
! DESCRIPTION:      Simulates dc Collector Characteristics for an HBT
! DATE/AUTHOR:      3/27/92 DSW
DIM
    FREQ    KHZ
    RES     OH
    IND     NH
    CAP     PF
    LNG     MIL
    TIME    US
    COND    /OH
VAR
EQN
CKT
  S1Pa_D1     2   5      [MODEL=DBC]

  HBT_Q1    2 3 0 4 5 6 0 8 rb=13.5  rc=12.3  re=6.2                    &
            is=1.62e-27  nf=1.03  ise=3.68e-20  ne=1.551                 &
                         nr=1.3   isc=2e-16     nc=1.472                 &
            a1=1.6   a2=12981  a3=816  a4=1.004e6   a5=392.2     br=0.01 &
            cje=2e-14  vje=1.7  me=0.5 t0=5.5e-12   t1=11.9e-12  t2=3000 &
            cjc=1e-14  vjc=1.42 mc=0.5 tr=1e-11     xbc=0.3      fc= 0.5 &
            temp=300   rth=2900 tmp0=296  kb=.0038 kvbe=0.0014
  cap_cce   5  6 c=.015
  res_ro    5  6 r=10000
  cap_cth   8  0 c=172

  res_rout 10 3 r=.01
  res_rin  11 2 r=.01
  DEF2P 2 3 model1
MODEL
  DBC    D    IS=3e-16 N=1.47 CJO=4e-14
SOURCE
  model1 pulse_ib 11 0 amp=1.8 f^f1  tw=5 nh=60 wght=1 tr=0 tf=0 td=1
  model1 vs_vce  10 0  dc=6
DCTR                                                              ! dc
FREQ
  step 100
  nh=60
OUT
  model1 i_Ib   res_rin  gr1
  model1 i_Ic   res_rout gr1
  model1 v_Temp 8 0      gr2
  model1 i_Ib   res_rin  SCN
  model1 i_Ic   res_rout SCN
  model1 v_Temp 8 0      SCN
GRID
  time 0 10 10
  gr1  0 40 40
  gr2  3 8 5
  time 0 10 .5
  SCN
HBCNTL
 sample = 2
  reltol=  1e-5
  reltolv= 1e-4
  abstolv= 1e-5
```

A.4 Example Circuit file for HBT Microwave Simulation

```
! CIRCUIT FILENAME:  power_full2.ckt
! DESCRIPTION:       Simulates dc Collector Characteristics for an HBT
! DATE/AUTHOR:       3/27/92 DSW
DIM
    FREQ     GHZ
    RES      OH
    IND      NH
    CAP      PF
    LNG      MIL
    TIME     PS
    COND     /OH
    CUR      MA
    PWR      DBM
VAR
EQN
CKT
  S1Pa_D1       2   5       [MODEL=DBC]

  HBT_Q1    2 3 0 4 5 6 0 8 rb=13.5  rc=12.3  re=6.2                     &
           is=1.62e-27  nf=1.03  ise=3.68e-20  ne=1.551                  &
                         nr=1.3   isc=2e-16     nc=1.472                  &
            a1=1.6   a2=12981  a3=816  a4=1.004e6   a5=392.2     br=0.01 &
            cje=2e-14  vje=1.7  me=0.5 t0=5.5e-12   t1=11.9e-12  t2=3000 &
            cjc=1e-14  vjc=1.42 mc=0.5 tr=1e-11     xbc=0.3      fc= 0.5 &
            temp=300   rth=2900 tmp0=296  kb=.0038 kvbe=0.0014
  cap_cce   5   6 c=.015
  res_ro    5   6 r=10000
  cap_cth   8   0 c=172

  res_rout 10 3 r=.01
  res_rin  11 2 r=.01
  DEF2P 2 3 model1
MODEL
  DBC    D    IS=3e-16 N=1.47 CJO=4e-14
SOURCE
  model1 p_Pin    14 0   r=res_rin p^pwr f^f1
  model1 res_Rs   13 14  r=50
  model1 cap_Cs   15 13  c=1000
  model1 vs_vbe   12 0   dc=1.5
  model1 ind_Is   15 12  l=1000
  model1 ind_Ib   15 11  l=.0456
  model1 cap_cb   13 0   c=.00114

  model1 vs_vce   18  0 dc=3
  model1 ind_lce 10 18 l=1000
  model1 res_rl   17  0 r=50
  model1 cap_cc   16 17 c=1000
  model1 ind_lc   10 16 l=.0365
DCTR
  dctr1 vs_vbe
  step  1.52 1.61 1.68 1.73 1.77
  dctr2 vs_vce
  sweep 0 2 .1
  sweep 2.5 8 .5
POWER
  step 10 20 25 30 32 34
```

```
FREQ
  step 5.5
  nh=20

OUT
! modell i_Ib   res_rin  gr1
  modell i_Ic   res_rout gr1
  modell v_Vce  3  0     gr1
! modell v_Vbe  2  0     gr1

  modell v_Temp 8 0      gr2

  modell PF_Pfund 17 0  r=res_rl h1=1 gr3
  modell PF_Ph2   17 0  r=res_rl h1=2 gr3
  modell PF_Ph3   17 0  r=res_rl h1=3 gr3
  modell PF_Ph4   17 0  r=res_rl h1=4 gr3

  modell i_Ic 3 0 res_rout  gr4

  modell v_Vbe  2  0     SCN
  modell i_Ib   res_rin  SCN
  modell v_Vce  3  0     SCN
  modell i_Ic   res_rout SCN
  modell v_Temp 8 0      SCN
!  modell PF_Pfund 17 0  r=res_rl h1=1 SCN
!  modell PF_Ph2   17 0  r=res_rl h1=2 SCN
!  modell PF_Ph3   17 0  r=res_rl h1=3 SCN
!  modell PF_Ph4   17 0  r=res_rl h1=4 SCN
GRID
  time 0 400 400
    gr1   0 27 27
    gr2   3 5 2
! time 0 400 10
!   SCN
  power 10 35 25
    gr3 -50 40 90
  dctr2  0 8 8
    gr4 0 30 30
HBCNTL
 sample = 2
  reltol=  1e-5
  reltolv= 1e-4
  abstolv= 1e-5
```

Vita

David S. Whitefield was born in Philadelphia Pennsylvania on December 27, 1967 to Janet and Thomas Whitefield. He graduated with high honors from Lehigh University in 1989 with a BS in Electrical Engineering and in 1991 with an MSEE. He is a member of Tau Beta Pi and Eta Kappa Nu.

He is the co-author of two papers:

D.S. Whitefield, C.J. Wei, and J.C.M. Hwang, "High Power Characterization of Heterojunction Bipolar Transistors," 1992 IEEE Princeton Section Sarnoff Symposium, Session II.

D.S. Whitefield, C.J. Wei, and J.C.M. Hwang, "Temperature-Dependent Large Signal Model of Heterojunction Bipolar Transistors," 1992 GaAs IC Symposium, pp. 221-224